Characterization of a turbulence bifurcation underlying L-mode confinement transitions on Alcator C-Mod

by

Norman Ming-Chen Cao

B.S., Massachusetts Institute of Technology (2015)

Submitted to the Department of Nuclear Science and Engineering
in partial fulfillment of the requirements for the degree of

Doctor of Philosophy in Applied Plasma Physics

at the

MASSACHUSETTS INSTITUTE OF TECHNOLOGY

June 2020

Author . . . .
Department of Nuclear Science and Engineering
May 19, 2020

Certified by . . . .
John E. Rice, Sc.D.
Senior Research Scientist, Plasma Science and Fusion Center
Thesis Supervisor

Certified by . . . .
Anne E. White, Ph.D.
Professor and Head, Nuclear Science and Engineering
Thesis Reader

Accepted by . . . .
Ju Li, Ph.D.
Battelle Energy Alliance Professor of Nuclear Science and Engineering
and Professor of Materials Science and Engineering
Chair, Department Committee on Graduate Theses

Characterization of a turbulence bifurcation underlying L-mode confinement transitions on Alcator C-Mod

by

Norman Ming-Chen Cao

Submitted to the Department of Nuclear Science and Engineering
on May 19, 2020, in partial fulfillment of the
requirements for the degree of
Doctor of Philosophy in Applied Plasma Physics

Abstract

Empirical energy confinement scalings play a crucial role in the design of tokamak fusion reactors, measuring how quickly energy is transported by turbulence from the fusion-producing core to conduction loss at the edge. Unfortunately, experiments often exhibit discontinuous changes in scaling behavior as the plasma parameters are varied, termed confinement transitions. Navigating these transitions requires an understanding of the physical origin and limits of confinement scalings, and is crucial for retiring the physics risk of extrapolating empirical results to future reactors.

This thesis explores the connection between two universally observed transitions in tokamak transport: the Linear to Saturated Ohmic Confinement (LOC/SOC) transition and the concomitant intrinsic rotation reversal. Analysis and modeling of rotation reversal hysteresis experiments show that a single turbulent bifurcation underlies both transitions on Alcator C-Mod. Plasmas on either side of the reversal exhibit different toroidal rotation profiles and therefore different turbulence characteristics despite profiles of density and temperature which are indistinguishable within measurement uncertainty. Elements of this bifurcation are also shown to persist for auxiliary heated L-modes. Within a reduced quasilinear transport model, the deactivation of subdominant (in linear growth rate and contribution to heat transport) ion temperature gradient (ITG) and trapped electron mode (TEM) instabilities is identified as the only possible change in turbulence across the reversal which is consistent with the measured profiles and inferred heat and particle fluxes. Experimental constraints on a possible change from strong to weak turbulence, outside the description of the quasilinear model, are also discussed.

These results indicate an explanation for the LOC/SOC transition that provides a mechanism for the hysteresis through the dynamics of subdominant modes and changes in their relative populations, and does not involve a change in the most linearly unstable ion-scale drift-wave instability. This work highlights the importance of considering the dynamics of the entire mode spectrum, and not just the dominant modes, in making predictions about transport and confinement regimes.

Thesis Supervisor: John E. Rice, Sc.D.
Title: Senior Research Scientist, Plasma Science and Fusion Center

Thesis Reader: Anne E. White, Ph.D.
Title: Professor and Head, Nuclear Science and Engineering

Acknowledgments

I would not be where I am today if it were not for the many amazing people I have met, who have supported me and helped me grow through all the challenges that life and research throw at you.

First, I would like to thank my thesis supervision committee. My supervisor, Dr. John Rice, has been a constant source of good advice, wisdom, and grammatical corrections. His nose for interesting experimental work is unparalleled, as it was originally at his suggestion that I take a look at the rotation reversal hysteresis which lies at the heart of this thesis. My faculty advisor, Prof. Anne White, helped orient me as a fledgling graduate student and set an example of achievement and positive impact to aspire towards. Her input has helped me sharpen my research considerably. Lastly, I'd like to give special thanks to Prof. Patrick Diamond. He has gone above and beyond as a mentor to me, and has been an endless fount of knowledge for me to pick at with my questions. He has provided me with so many opportunities to grow as a scientist and researcher, and has always pushed me to improve and to keep learning new things. Without his guidance and supervision my research would be a mere shadow of what it is now.

I'd also like to thank the many collaborators who helped make this work possible. On the experimental side, I would like to offer thanks to many members of the Alcator C-Mod team, including the technicians, engineers, and diagnosticians who helped make the experiments a reality. I'd like to thank Dr. Matthew Reinke, whose work on x-ray imaging crystal spectroscopy on Alcator C-Mod formed the foundation of this work, and I am extremely grateful for his efforts teaching me how to use the tools he created. Other contributors to the experiments in this thesis include Dr. Seung-Gyou Baek, Dr. Alexander Creely, Dr. Paul Ennever, Dr. Amanda Hubbard, Dr. Jerry Hughes, and Dr. Jim Irby.

On the modeling side, I was reliant on many of the Python tools developed by Dr. Mark Chilenski, including those for performing Gaussian Process Regression. The work on uncertainty quantification in this thesis owes everything to Francesco

Sciortino's expertise in computational Bayesian techniques, who also helped me with Gaussian Process Regression in this thesis. Dr. Pablo Rodriguez-Fernandez, who I began my research journey with as a fellow first-year, ran TRANSP for all the experiments in this thesis. I'd like to thank Dr. Nathan Howard, who taught me how to use GYRO. On the theoretical components, I'd like to thank the organizers of the Festival de Théorie and the Chengdu Theory Festival, where I met with and learned from many people both inside and outside of plasma physics. I'd also like to acknowledge the financial support this work received from the U.S. Department of Energy, Office of Science, Office of Fusion Energy Sciences under Award Numbers DE-FG02-04ER54738, DE-SC0014264, DE-FC02-99ER54512. Lastly, I'd also like to acknowledge the administrative staff Jessica Coco and Valerie Censabella, who made my life as a graduate student easy.

I would not made it through these past five years without my friends. Staly Chin and Victor Hung, without your inspiration I don't think I would have had the courage to pursue research. To the residents of safetythird, safetyfourth, and other company, I'd like to thank you for the sense of community you've fostered over the years. The same extends to my colleagues at the Plasma Science and Fusion Center and others I've met as a graduate student, who have helped make a very welcoming research environment. Special mention to Adam Kuang, who has been a source of interesting discussion, advice, and friendship. Francesco Sciortino also gets a second mention here for being a good person to bounce ideas off of, and for helping set up the turbulence and transport reading group with me. I'd also like to thank Ann Choi, who has been my solid rock and warm ray of sunshine.

Finally, I would like to thank my parents, who throughout my life have encouraged me to develop my passions and instilled in me the value of perseverance. I am eternally grateful for their trust and support.

Contents

List of Figures

List of Tables

Chapter 1

Introduction

Development of magnetic confinement fusion reactor concepts provides the most promising pathway for the production of fusion energy. A major challenge in the design of these reactors, such as tokamaks and stellarators, is the need for effective models of fusion plasma behavior used in the design phase to ensure reactor performance requirements are met and to optimize rector size and cost. Unfortunately, magnetically confined fusion plasmas are typically turbulent, demonstrating a complex dependency between external actuation and the plasma response. This makes it difficult to create and understand predictive models of fusion plasma behavior.

This thesis primarily explores how transitions between different macroscopic regimes of turbulence can be linked to changes in the underlying microscopic flow patterns. Characterizing this link helps shed light on the origins of empirically observed trends in plasma behavior, and provides a physical basis for the construction of improved models of plasma turbulence. This chapter will discuss the motivation for this work, and will introduce the key results of this thesis.

1.1 Why Study Confinement in Fusion Plasmas?

Many of the key challenges to harnessing fusion energy on Earth come from the fact that fusion plasmas must be maintained at extreme temperatures in order to reach significant fusion reaction rates. For magnetic confinement fusion power plants, the target temperatures are around 20 keV, or over 200 million degrees Celsius, which correspond to the peak of the thermally averaged deuterium-tritium (D-T) fusion reaction cross section. Cross-sections for Coulomb collisions are many orders of magnitude higher than cross-sections for fusion reactions between fusing nuclei, so the bulk of ions in the fusion plasma will always be thermal. In addition, these temperatures must be maintained for a large enough density of plasma for economically useful amounts of energy to be produced, typically resulting in plasma densities on the order of 10^{20} particles per cubic meter, and confined plasma pressure on the order of 10^5 pascals or 1 atmosphere.

Since the walls of the fusion reactor constituting the boundary of the plasma must be kept in a non-plasma state at temperatures well below 200 million degrees Celsius, large gradients of plasma temperature and density necessarily exist in fusion plasmas. These gradients act as sources of free energy, which drive significant transport of heat, particles, and momentum across the plasma. Such transport has been experimentally observed to be many orders of magnitude larger than what would be predicted from collisionally-driven transport alone. This additional transport, often called anomalous transport, is thought to be due to plasma microturbulence. The consequence of this turbulent transport on reactor performance can be summarized by the energy confinement time τ_E, defined as the ratio of the plasma stored energy (the plasma response) to input heating power (the external actuation). Stronger turbulent transport corresponds to a shorter energy confinement time, which corresponds to energy being exhausted more quickly out of the plasma.

The importance of the energy confinement time comes from the fact that fusion reactions produce power at a rate fixed by the density and temperature of the ions. If the energy confinement time is too low, then the power required to keep the plasma in fusion-producing conditions exceeds the amount of power generated by the fusion reactions. The fusion reactor would on average consume more energy than it produces, which is not desirable for an electrical generation system. The criterion for fusion self-sufficiency is captured by the triple product of the plasma density n, plasma temperature T, and confinement time τ_E

$$nT\tau_E > 3 \times 10^{21}\mathrm{m}^{-3}\mathrm{keV\ s} \tag{1.1}$$

Thus, we see that the energy confinement time is a key metric of fusion plasma performance. The confinement time demonstrates a dependency on plasma parameters that cannot be described with a single scaling law [63, 34], and importantly can show discontinuous changes in scaling behavior, called confinement transitions. Moreover, not all transport is deleterious, as turbulence can lead to significant thermally-driven up-gradient particle and momentum fluxes. Thus, to understand the behavior of transport in fusion plasmas, it is necessary to understand the dynamics which govern the plasma response, many of which are internal to the plasma, and how they could lead to different regimes of plasma behavior.

Two major questions will be at the focus of this thesis. The first is centered around energy confinement: how does turbulence influence the transport of injected power in the tokamak? The second is in momentum transport: when do large-scale coherent flows form from turbulence in tokamaks, and in the fusion energy context, how do these flows interrelate with energy confinement?

Even with improving computation models of plasma turbulence, confinement scalings will always play a role in building intuition about the performance of fusion devices, and are needed for rapid 0-D iteration to provide high-level guidance for parameter spaces where detailed fusion reactor design work can focus. Better understanding of the physical origin of confinement scalings can also help with the creation of reduced models which serve as a bridge between computationally expensive full physics simulations, and empirical scaling laws. Finally, understanding how the small scale microturbulence leads to changes in macroscopic observables is an interesting physical question in its own right. Thus, it is crucial to understand the physical origins and limits of confinement scalings in order to retire physics risk and identify interesting operational regimes for future fusion reactors.

1.2 Roadmap to Wave Turbulence

Before diving into the specifics of the physics underpinning tokamak turbulence, this section first sketches out where tokamak turbulence sits in relation with other paradigmatic examples of fluid and plasma turbulence, and motivates the physics needed to model it. What lessons learned from other turbulence models can help us with modeling tokamak turbulence, and vice versa? We will find that turbulence necessarily has a broad range of interacting length scales and time scales which typically interact in a chaotic manner, making both analytic and computational study of turbulence difficult.

Tokamak turbulence in the core is hypothesized to be wave turbulence, where the plasma flows and other fluctuations are primarily organized into a spectrum of weakly nonlinear waves [89]. This sets it apart from the study of traditional incompressible fluid turbulence, where fluid elements and vortexes are thought to be more fundamental. This wave character forms the basis of validity for certain perturbative approaches, typically referred to as quasilinear theory or a variant thereof, in the description of turbulence in tokamaks [108, 74, 31]. While the usage of quasilinear theory represents a major gain in our power to model and understand tokamak transport, theoretical understanding and experimental validation of the wave character is important for determining the applicability of the predictions to real-world situations.

1.2.1 The Need for a Statistical Theory of Turbulence

Tokamak plasmas are generally collisionless, or very weakly collisional, with a high enough density of particles that particle discreteness effects are weak, which suggests that we begin with a kinetic description of the plasma. This description begins with the Boltzmann equation, which will serve as the basic model of plasma particle dynamics we will consider:

$$\frac{\partial f_s}{\partial t} + \mathbf{v} \cdot \frac{\partial f_s}{\partial \mathbf{x}} + \frac{\mathbf{F}_s}{m_s} \cdot \frac{\partial f_s}{\partial \mathbf{v}} = C[f_{s_1}, f_{s_2}, ...] \tag{1.2}$$

Here $f_s = f_s(\mathbf{x}, \mathbf{v}, t)$ is the probability distribution function which describes how likely it is to find a particle of species s at position $\mathbf{x}$ with velocity $\mathbf{v}$. m_s is the particle mass, and $\mathbf{F}_s = \mathbf{F}(\mathbf{x}, \mathbf{v}, t)$ is the net force experienced by a particle at each point in phase space $(\mathbf{x}, \mathbf{v})$. Two-particle interaction effects are taken into account in the collision operator $C[f_{s_1}, f_{s_2}, ...]$, which is a nonlinear functional which also couples different particle species together, and in plasmas typically takes the form of a velocity space diffusion combined with a drag, as in the Landau collision operator [55]. Note that if we were to drop the collisional term, then the equation takes the form of a advection equation in phase space for the f_s. This collisionless version is also known as the Vlasov equation.

In plasmas, the force of interest is the Lorentz force:

$$\mathbf{F}_s = q_s(\mathbf{E} + \mathbf{v} \times \mathbf{B}) \tag{1.3}$$

where q_s is the species charge, and $\mathbf{E} = \mathbf{E}(\mathbf{x}, t)$ and $\mathbf{B} = \mathbf{B}(\mathbf{x}, t)$ are the electric and magnetic fields respectively. In this thesis SI unit conventions are used. In order to close the equations, we need equations to solve for the electric and magnetic fields. In this case we use Maxwell's equations without displacement current, since we look at phenomena which do not involve the propagation of light:

$$\nabla \cdot \mathbf{E} = \frac{\rho}{\varepsilon_0} \tag{1.4}$$

$$\nabla \cdot \mathbf{B} = 0 \tag{1.5}$$

$$\nabla \times \mathbf{E} = -\frac{\partial \mathbf{B}}{\partial t} \tag{1.6}$$

$$\nabla \times \mathbf{B} = \mu_0 \mathbf{J} \tag{1.7}$$

Here ρ and $\mathbf{J}$ are the charge and current density respectively, which is calculated in terms of moments of the particle distribution functions as

$$\rho = \sum_s \int \mathrm{d}^3\mathbf{v}\, q_s f_s \tag{1.8}$$

$$\mathbf{J} = \sum_s \int \mathrm{d}^3\mathbf{v}\, q_s \mathbf{v}_s f_s \tag{1.9}$$

Since the electromagnetic fields depend on moments of the distribution function, the Vlasov equation plus Maxwell's equations together form a nonlinear advection equation for the distribution function. We also note that this set of equations without collisions is time-reversible, and conserves the total entropy $\sum_s \int \mathrm{d}^3\mathbf{x}\, \mathrm{d}^3\mathbf{v}\, f_s \log f_s$ for sufficiently smooth initial conditions.

We can compare the situation of plasmas to that of incompressible fluid flow, described by the Navier-Stokes equations, here written in dimensionless form

$$\frac{\partial \mathbf{u}}{\partial t} + \mathbf{u} \cdot \nabla \mathbf{u} = -\nabla p + \frac{1}{Re} \nabla^2 \mathbf{u} \tag{1.10}$$

$$\nabla \cdot \mathbf{u} = 0 \tag{1.11}$$

Here $\mathbf{u} = \mathbf{u}(\mathbf{x}, t)$ is a fluid velocity and Re is the Reynolds number, the ratio between inertial forces and viscous forces. We note that the Navier-Stokes equations also take the form of a non-linear advection equation for the fluid velocity, and when ignoring dissipation (by setting $Re = \infty$) has a time-reversible counterpart, the Euler equations, which conserves the total fluid kinetic energy for sufficiently smooth initial conditions.

The equations that support turbulence look innocuous enough, so what leads to the difficulty of describing turbulence? For incompressible fluid flow, turbulence leads to the irreversible dissipation of fluid kinetic energy via viscous heating. Paradoxically, this dissipation must occur in the inviscid limit $Re \to \infty$. This paradox is reconciled by noting that the viscosity has the highest-order spatial derivative in the Navier-Stokes equations, and hence the inviscid limit is a singular limit. Finite dissipation, called anomalous dissipation, can still occur if $\nabla^2 \mathbf{u}$ diverges as $Re \to \infty$, which corresponds to flow energy active at finer and finer spatial scales [42, 62]. Similar arguments apply to the plasma turbulence, where entropy is still generated at a finite rate even in the limit of vanishing collisionality by generation of fine-scale velocity-space structure, through possible mechanisms such as Landau damping or nonlinear phase mixing [109]. Since turbulence is typically sustained by drive or mixing at large scales compared to the dissipation scales, in the absence of direct coupling of large to small scales, the requirement of anomalous dissipation necessitates a broad cascade of energy through intermediate scales to fully realize the turbulent state.

The broad range of active scales in turbulence implies a huge number of degrees of freedom. In 3-D Navier-Stokes turbulence, a simple estimate [44] suggests that the number of mesh points needed to simulate turbulence grows as $\sim Re^{9/4}$, while the number of time steps grows as $\sim Re^{3/4}$. Even modest Reynolds numbers of $Re \approx 2000$, which is around the minimum Reynolds number required to observe sustained turbulence in pipe flows, are extremely expensive to compute. One might hope that the precise details of all of these degrees of freedom will not matter, and instead only their long-time collective statistical properties would determine the long-time average behavior of the system. Thus we will try to construct a statistical theory of turbulence using the apparatus of Reynolds averaging.

A Reynolds average $\langle \cdot \rangle$ is defined as any abstract operation which satisfies linearity and the averaging property. That is, for random variables or fields ϕ, ψ and a an arbitrary constant, the following hold:

$$\langle \phi + \psi \rangle = \langle \phi \rangle + \langle \psi \rangle \tag{1.12}$$

$$\langle a\phi \rangle = a \langle \phi \rangle \tag{1.13}$$

$$\langle \langle \phi \rangle \psi \rangle = \langle \phi \rangle \langle \psi \rangle \tag{1.14}$$

Note the final property implies $\langle \langle \psi \rangle \rangle = \langle \psi \rangle$. Typically, the averaging operator will also commute with space, time, and velocity differentiation and integration. There are many ways to construct such an operator, including averaging along directions of symmetry (including zonal averaging or averaging over all of space), taking a flux-surface average for tokamaks, or using an ensemble average. In some cases it is useful to define the averaging with respect to a specific length scale, denoted $\langle \cdot \rangle_\ell$, where the operator will correspond to convolution with a spatial and/or temporal filter. In this thesis unless otherwise specified, the averaging operator will correspond to a flux-surface average. We define the fluctuating component of a field as

$$\tilde{\psi} = \psi - \langle \psi \rangle \tag{1.15}$$

The hope is that only a subset of the degrees of freedom, preferably ones corresponding to averaged quantities which evolve on large spatial scales and slow time scales, will determine the statistics of the small-scale fluctuations.

1.2.2 Role of Waves in Turbulence

So, with this in mind, how could we go about constructing the statistical theory? Perhaps if the deviations from the mean state are weak enough, a linearization perturbation approach around the mean state may work. For fluid and plasma systems, this typically will result in a spectrum of waves which can be excited in the medium. This is where the pictures of Navier-Stokes turbulence and tokamak turbulence will begin to diverge. In 3-D Navier-Stokes turbulence, energy is generally considered to proceed from large injection scales to small dissipation scales via a chain of nonlinear eddy-eddy interactions, which is poetically captured by Richardson (taking after the older works by Augustus De Morgan and Jonathan Swift):

> *Big whorls have little whorls*
> *Which feed on their velocity,*
> *And little whorls have lesser whorls*
> *And so on to viscosity.*

For high Reynolds number isotropic turbulence, this is captured quantitatively by the paradigmatic self-similar cascade of energy through scale posited by Kolmogorov's famous K41 theory [44]. In K41, the timescale at which energy is thought to proceed to dissipation scales is dictated by the eddy turnover time, which would not appear in the linearization around a Navier-Stokes mean flow state which lacked these eddies.

Two properties of drift wave turbulence in tokamaks conspire to make the usage of the *linear response* plausibly adequate for the study of transport in tokamaks. The first property is that in a linear approximation, plasmas act as a dispersive medium for a variety of waves, particularly drift waves which will be covered next in Section 2.2. Additionally, particles traveling through the broad spectrum of active waves typically have chaotic trajectories, so an ensemble of particle orbits initially nearby each other soon disperses stochastically. Wave dispersion and particle orbit stochasticity act together to limit the interaction time between traveling wavepackets and particles experiencing forces from the waves. The net effect is that particles can be thought of as experiencing forces from the waves which are small-amplitude enough that the linear response applies, and weakly correlated enough that the central limit theorem applies, predicting diffusive behavior from wave-particle interaction. This forms the basis of quasilinear theory, which Section 2.3 and Appendix A will discuss in more depth. Additionally, the dispersion means that wavepackets have a short interaction time with other wavepackets, which makes nonlinear effects related to the formation of beat modes also weak.

This weak wave nonlinearity can be contrasted with the example of strong $Pr = 1$ classical Rayleigh-Bénard turbulence, where the Rayleigh number is large enough that a broad range of modes are excited, and the Bénard cells do not survive. Tokamak turbulence and Rayleigh-Bénard turbulence are both examples of thermally-driven convection in which the mean state supports a broad range of linearly unstable modes. While mean states with sufficiently weak perturbations may have fluctuations which initially resemble the linear stage of the Rayleigh–Bénard instability, these modes soon grow in amplitude and nonlinearly interact with each other, causing them to lose their linear character. This could also be the case near the tokamak edge, where the fluctuations are large enough that there is significant nonlinear interaction between modes, which may lead to the breakdown of quasilinear estimates. Note that the breakdown of weak wave nonlinearlity could be scale-dependent, leading to a coexistence of weak wave turbulence with other forms of turbulence even at the same spatial location.

The second property which allows for the usage of the linear response as a plausible basis of a transport theory in tokamaks is that the time-reversal symmetry of the linear response is broken without needing to invoke nonlinear effects, even in the limit of zero dissipation. For linearly unstable systems, the existence of unstable modes in a time-reversible system can be thought of as a form of spontaneous time-reversal symmetry breaking[1]. Even in the case for plasma systems without a linear instability, Landau damping provides another form of time-reversal symmetry breaking via the process of phase mixing. This time-reversal symmetry breaking continues to be important in the limit of vanishing growth/damping rate γ due to the resonant denominator in the linear response, as is typically seen in derivations of Landau damping:

$$\frac{1}{\omega - \mathbf{k}\cdot\mathbf{v} + i\epsilon} \xrightarrow[\epsilon\to 0^+]{} \frac{\mathcal{P}}{\omega - \mathbf{k}\cdot\mathbf{v}} - i\pi\delta(\omega - \mathbf{k}\cdot\mathbf{v}) \tag{1.16}$$

where the symbol $\mathcal{P}$ refers to the principal value, and the limit is taken for $\epsilon > 0$ in order to enforce causality. This is an example of a singular limit, where the $\epsilon \to 0^+$ case differs from the $\epsilon = 0$ case by the presence of the delta function for particles satisfying the resonance condition $\omega - \mathbf{k}\cdot\mathbf{v} = 0$, which introduces an imaginary component to a value that would otherwise be real for ω and $\mathbf{k}\cdot\mathbf{v}$ both real[2]. If the conditions for quasilinear theory are met, this time-reversal symmetry breaking leads to net irreversible transport.

The importance of time-reversal symmetry breaking can be illustrated with the example of adiabatic quasigeostrophic Rossby wave turbulence in a steady mean flow, modeled by the Charney-Hasegawa-Mima (CHM) equation [25]. Rossby waves are strongly dispersive and can be regularly observed in the atmospheres and oceans, suggesting the appropriateness of using the linear response to describe the interaction of

---

[1] That is, even though the evolution operator commutes with the time-reversal operator, unstable eigenmodes of the evolution operator and are not also eigenmodes of the time-reversal operator, i.e. are not invariant under time-reversal. This is possible because the evolution operators are non-Hermitian, see [5, 96].

[2] For information about how this analytic continuation comes about as a time-asymptotic result of the initial value problem, see Van Kampen [68]. Recent work by Mouhot and Villani [87, 118] have also rigorously established the relevance of Landau damping beyond the linear approximation, for weak enough nonlinearity. See [117, 109] for explicit examples of Landau damping being arrested by nonlinearity, reinforcing the importance of the criterion of weak nonlinearity.

the mean flows with the waves. If the mean flow satisfies the Rayleigh-Kuo criterion so there are no linear instabilities [76], and varies on large enough length scales that the waves propagate adiabatically, conservation of wave action applies and a wave kinetic equation can be derived [89]. While this setup is successful at describing the *reversible* transport of momentum by waves via radiation, the Charney-Drazin theorem [20], commonly known as a non-acceleration theorem, implies that irreversible transport of momentum can only occur when waves are generated or dissipated. This requires the breaking of the time-reversal symmetry by some mechanism. In the CHM equations this could occur in the linear response at critical layers where the adiabatic assumption breaks down, which involve a resonance between the wave phase velocity and the mean shear flow velocity [113]. Alternatively this could occur via explicit inclusion of nonlinear mechanisms, such as Rossby wave breaking [35], shearing by nonlinearly generated zonal flows leading to ray stochasticity [110], or consideration of the wave cascade of some conserved quantity to small scales in Kolmogorov-Zakharov wave spectra [89].

Thus, the picture we find of turbulence in the tokamak core is that weakly nonlinear waves could plausibly be responsible for most of the irreversible transport of heat, particles, and momentum. The key assertions made in this section to support this claim, and how other paradigmatic examples of turbulence relate to these assertions, are summarized in Table 1.2.2. This represents a major gain in the modeling of tokamak turbulence, as it suggests an approximate 'factorization' of transport calculations into calculation of the linear response or eigenmodes of the system, and then a separate calculation of what the ultimate fates of those linear perturbations are. It is much easier to calculate the eigenmodes of a system than it is to solve a fully nonlinear evolution equation, and the framing of the nonlinear interaction of fluctuations as the weak nonlinear interaction of wavepackets simplifies the modeling of nonlinear theories.

While this section paints a rosy picture of drift wave turbulence in tokamaks, it is important to critically assess whether or not such a picture actually holds in reality. One of the major results of this thesis is the demonstration of two mean plasma

Paradigmatic Turbulence Example	Weak nonlinearity permits usage of linear response?	Linear response breaks time-reversal symmetry?
High Reynolds Number Isotropic Navier-Stokes (K41)	No	No
Strong Rayleigh-Bénard	No	Yes
Steady Adiabatic Charney-Hasegawa-Mima (Quasigeostrophic Rossby) Wave	Yes	No
Tokamak Core Drift Wave	Yes	Yes

Table 1.1: Types of turbulence in comparison to tokamak core turbulence, and the proposed relationship with the linear response in each case for fluctuations of interest. Note these assertions are only approximate, and will not hold uniformly across all scales active in the turbulence.

profiles which have the same linear spectrum (in terms of real frequency, growth rate, and quasilinear weights, to be defined in Chapter 2), but which manifest different states of turbulence and lie on different branches of a confinement scaling law. This provides an ideal testbed for interrogating the assumptions of quasilinear theory, as it provides a controlled experiment where the linear modes remain the same, but the nonlinear interactions involving these modes necessarily change.

1.3 Turbulence Transitions Observed in Ohmic Plasmas

This work focuses primarily on two transitions observed universally in tokamak plasmas: the Linear to Saturated Ohmic Confinement (LOC/SOC) transition and the intrinsic rotation reversal. The LOC/SOC transition refers to a break in the slope of the scaling of energy confinement with respect to density in L-mode plasmas where the only power input is from Ohmic heating. The intrinsic rotation reversal refers to a spontaneous reorganization of a large-scale toroidally-directed mean shear flow observed to be driven in tokamaks in the absence of external momentum input. These transitions are illustrated in Figure 1-1. In response to scans of plasma density, these two transitions are found to occur at the same critical density, the reason for which is unknown. There is also a wealth of other phenomenology associated with the transitions, including density profile peaking, non-diffusive cold pulse propagation, fluctuation spectrum changes, and impurity density asymmetries. The concurrence of these two transitions suggests a link between the heat, particle, and momentum transport channels in tokamak core plasmas, reminiscent of how heat-flux driven turbulent Reynolds stresses are thought to trigger the L-H transition, and lead to shear layer formation.

While there has been some success in reproducing features of the LOC/SOC transition *in silico*, a self-contained physical picture of how changes in turbulence lead to the concurrence of these transitions and explain its observed properties remains elusive. Since drift wave turbulence is responsible for most of the heat, particle, and momentum transport in tokamaks, it has been conjectured that a transition from trapped electron mode (TEM) to ion temperature gradient (ITG) mode dominated turbulence could unify the confinement transition and rotation reversal. Experiments find changes in turbulent fluctuations across the LOC/SOC transition, and modeling suggests transport gradually changes from TEM-driven to ITG-driven across density ramps which transition from LOC to SOC. However, studies find no clear change in the dominant ion-scale linear instability from TEM to ITG (either in linear growth rate or driven quasilinear heat flux) at the transition itself. Additional insight is needed to elucidate if and how a TEM/ITG transition is involved in the rotation reversal.

1.4 Primary Results in the Thesis

The thesis presents three main results:

- A novel uncertainty quantification method for the fitting of line-integrated spectra, which is used to measure impurity ion temperature and velocity, summarized in Section 1.4.1.

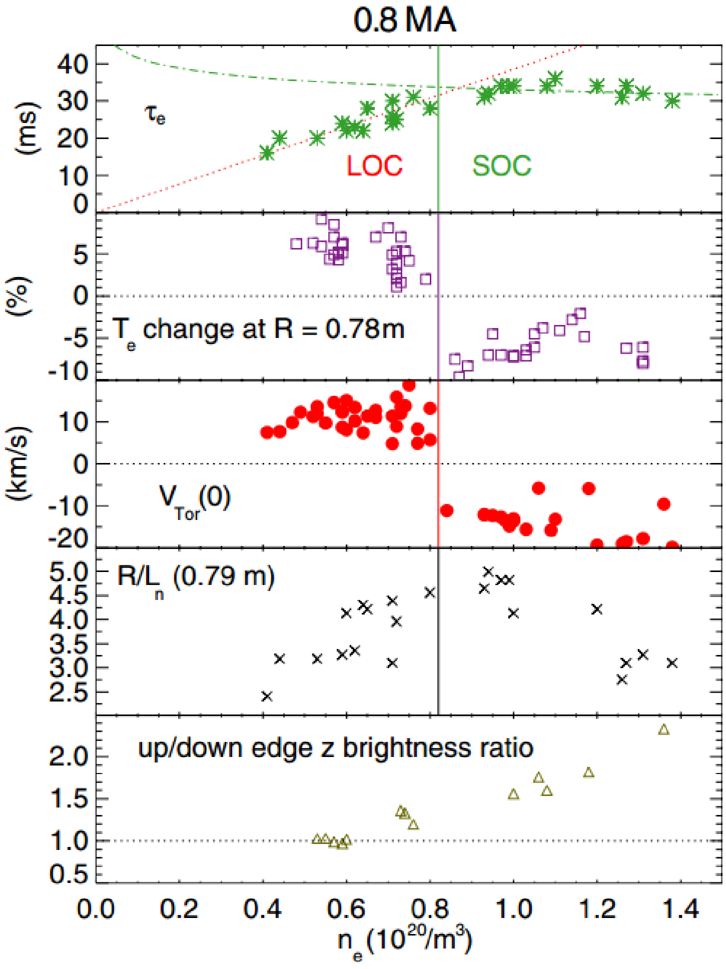

Figure 1-1: Plots of the energy confinement time (top), core heating in response to cold pulse injection (second frame), toroidal rotation (middle), density peaking as measured by inverse gradient scale length (fourth frame), and edge impurity up/down asymmetry brightness ratio (bottom) as a function of line-average electron density for 0.8 MA, 5.4 T discharges. Figure from [103]

- Analysis of rotation reversal hysteresis experiments which unambiguously demonstrates the existence of a nonlinear turbulence bifurcation separating the LOC and SOC states on Alcator C-Mod, summarized in Section 1.4.2.
- Quasilinear modeling which identifies a partial turbulence population collapse, which involves the deactivation of a subdominant instability, as a candidate theory for the reversal, summarized in Section 1.4.3. Consideration is also given to transitions outside the description of the quasilinear model.

1.4.1 Uncertainty Quantification via Bayesian Methods

This thesis presents a Bayesian spectral fitting method developed for spectroscopic data analysis, particularly (but not solely) in the context of fusion energy research. This work was published in [19]. The presented techniques are particularly valuable to estimate moments and corresponding uncertainties whenever the spectra result from line-integrated measurements in non-uniform plasmas, for which the approximation of atomic line shapes being ideal Gaussians gives poor estimates. The method decomposes multiple, potentially overlapping spectral lines into a sum of Gauss-Hermite polynomials, whose properties allow an efficient truncation and uncertainty quantification, often with only 3 free parameters per atomic emission line. Tests with both synthetic and experimental data demonstrate effectiveness and robustness where more standard non-linear fitting routines may experience difficulties.

1.4.2 Confirmation of Turbulence Bifurcation in L-mode

The experiments presented here were run on Alcator C-Mod, a compact ($R = 0.67$m, $a = 21$cm), high-field (B_t up to 8.1 T) diverted tokamak with a molybdenum wall [48]. Results were published in [17, 18]. Here, we provide evidence that the LOC/SOC transition and intrinsic rotation reversal are linked to a single nonlinear bifurcation of the plasma state in Alcator C-Mod, advancing the notion that LOC and SOC are representative of different states of nonlinearly saturated turbulence. The existence of a bifurcation is established through a set of experiments which use hysteresis as a probe of the LOC/SOC transition and intrinsic rotation reversal. Hysteresis is the dependence of a system's state on its history, and could result from memory or the evolution of hidden variables not tracked in the state space. This hysteresis is manifested as a bistability in the plasma response, corresponding to a range of experimental control parameters which exhibit either LOC-like or SOC-like rotation depending on whether the plasma entered this range from an LOC-like state or a SOC-like state. Hysteresis in L-mode intrinsic rotation has been reported previously in multiple experiments [9, 99, 102].

The experiments demonstrate nearly exact matches of mean plasma density and temperature which manifest different rotation and turbulent states in the same discharge. Elements of the bifurcation are also shown persist in auxiliary heated plasmas, suggesting its importance for understanding L-mode scaling in more generality. The results show that changes in the mean drive profiles of density and temperature alone cannot be responsible for the LOC/SOC transition and rotation reversal. In particular, a change in dominant linear instability from TEM and ITG alone is not sufficient to explain the transitions, and a full explanation will necessarily involve some change in turbulence saturation mechanism or other nonlinear behavior.

1.4.3 Proposal of Candidate Subdominant Mode Transition

To interpret the experimental results, a quasilinear estimate of the turbulent fluxes is used to explore possible changes in turbulence consistent with the observed transport. Related modes are grouped into families, which enables the use of experimentally inferred fluxes to provide meaningful constraints on the turbulence saturation levels. From this modeling we propose to identify the bifurcation as a partial turbulence population collapse, which involves the deactivation of a subdominant instability. This provides a candidate theory for the reversal and draws analogy with predator-prey models for the L-H transition, except in this case, not all ion-scale turbulent instabilities are quenched. Identifying the deactivated subdominant instabilities with intermediate scale (between electron and ion scales) TEM provides a hypothesis for reconciling the lack of a clear transition in the linear behavior of TEM/ITG with the observed sharpness of the LOC/SOC and rotation reversal transitions. While the precise physical mechanism underlying the proposed transition is not identified in this work, experimental constraints on the possibilities for such mechanisms are discussed. The possibility of a subdominant mode transition driven by a change from strong to weak TEM turbulence, which lies outside the description of the quasilinear model, is also discussed.

1.5 Thesis Outline

Chapter 2 begins the body of the thesis with an introduction and discussion of the physics underpinning this work. Chapter 3 follows with a brief introduction to X-ray Imaging Crystal Spectroscopy (XICS). This provides the requisite background material for Chapter 4, which presents better uncertainty quantification of ion temperature and velocity measurements by the Bayesian Spectral Fitting Code (BSFC). This better uncertainty quantification helps underpin Chapter 5, which presents experimental confirmation that a single nonlinear bifurcation underlies the LOC/SOC transition and intrinsic rotation reversal. These experiments are then analyzed in Chapter 6 using linear gyrokinetic simulations and a simplified quasilinear model. Chapter 7 discusses some of the physical mechanisms which could underlie the identified candidate subdominant mode transition, including physical mechanisms not captured by the quasilinear model. Finally, Chapter 8 summarizes the material presented in the thesis, discusses the larger implications of the physics results, and suggests several avenues for future research motivated by this work.

Chapter 2

Physics of Turbulent Transport in Tokamaks

This chapter will give a physical picture of turbulence in tokamaks. Physical intuition is emphasized instead of detailed derivations, which are left to the appendices when included. The exposition begins in Section 2.1 with an introduction to single-particle motion in a tokamak, which underpins all of the physical effects mentioned in this chapter. This is followed by Section 2.2, which describes how collective motion leads to instabilities in plasmas. Theoretical motivation is given for the specific choice of instabilities which are focused on in the rest of the thesis. Section 2.3 then covers how these instabilities are thought to lead to turbulent transport, providing a bridge between microscopic and macroscopic behavior. Finally, Section 2.4 covers topics of specific interest to describing the turbulence transitions that are at the focus of this thesis.

2.1 Single Particle Motion and Gyrokinetics

Since the magnetic force on a particle is perpendicular to both the magnetic field and the particle velocity, particles in uniform magnetic fields will execute a circular trajectory known as gyromotion in the plane perpendicular to the magnetic field with frequency defined as the gyrofrequency $\Omega_{ca} \equiv \frac{|q_a|B}{m_a}$ and radius defined as the

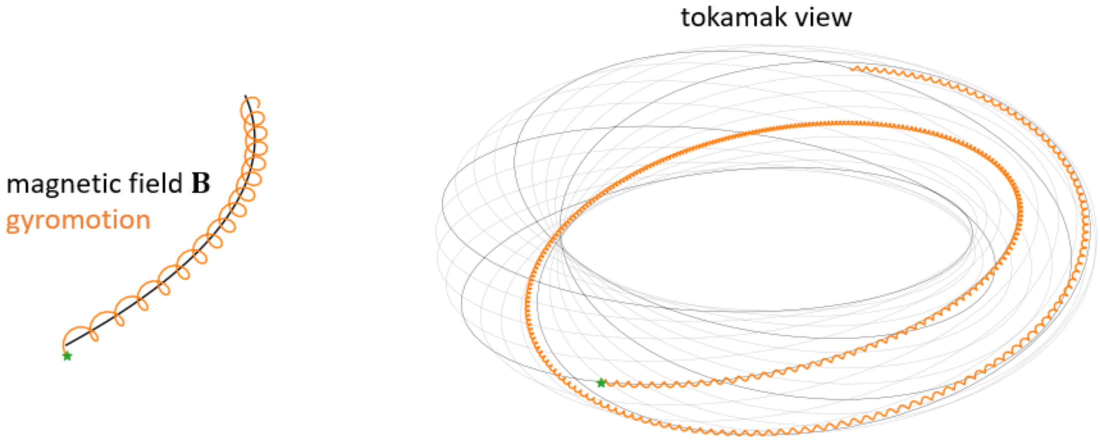

Figure 2-1: Graphics showing the trajectory of a particle, in orange, subject to a strong magnetic field, with field lines marked in black and gray. The initial position is marked in green. (Left) shows motion following a single field line. (Right) shows how the magnetic field lines in a toroidal configuration keeps the particle confined to toroidally shaped magnetic flux surfaces. The gyromotion is slowed down and exaggerated for emphasis. Additionally, note that the particle does not follow the field line exactly, and executes a drift relative to the field line.

gyroradius $\rho_a \equiv \frac{v_\perp}{\Omega_{ca}}$. This is illustrated in Figure 2-1. This circular motion constitutes a current, and hence the net motion is associated with an effective magnetic dipole moment of $\mu = \frac{mv_\perp^2}{2B}$, which is known as the first adiabatic invariant. The impact of this gyromotion is that in strong magnetic fields, where the confining magnetic field changes on spatial scales much larger than the gyroradius, particles will stream quickly along field lines at the thermal velocity $\sim v_{ta} \equiv \sqrt{T_a/m_a}$, but will tend to be confined near the magnetic field line. This motivates the toroidally nested magnetic topology of tokamaks and stellarators.

However, this confinement is not perfect, and particles will execute slow *drifts* across field lines due to the impact of other forces. Some drifts result from spatial inhomogeneity in the magnetic fields, which include the curvature drift due to the centrifugal force on particles following curved field lines, and the grad-B drift due to the magnetic mirror force acting on the effective magnetic dipole moment of the gyromotion.

$$\mathbf{v}_\kappa = \frac{mv_\parallel^2}{qB}\frac{\boldsymbol{\kappa} \times \mathbf{B}}{B^2} \tag{2.1}$$

$$\mathbf{v}_{\nabla B} = -\frac{1}{q}\frac{(\mu \nabla B) \times \mathbf{B}}{B^2} \tag{2.2}$$

These two drifts are important because they are intrinsic to the geometry of any toroidal confinement system, and in so-called ‘bad-curvature’ regions play the role of an effective gravity destabilizing gradients of temperature and density in the plasma, allowing for the conversion of thermal energy into kinetic energy to drive plasma turbulence. Other drifts result from interaction with other fields, of which the $E \times B$ drift due to interaction with electric fields is the most important.

$$\mathbf{v}_E = \frac{\mathbf{E} \times \mathbf{B}}{B^2} \tag{2.3}$$

The $E \times B$ drift is the motion responsible for most of the turbulent transport in plasmas. One final drift of relevance, the diamagnetic drift, is actually not a drift of individual particles but is instead a net fluid drift caused by pressure gradients.

$$\mathbf{v}_{*p} = -\frac{1}{nq}\frac{\nabla p \times \mathbf{B}}{B^2} \tag{2.4}$$

Its relevance comes from the fact that drift waves are associated with diamagnetic drifts, which will be expanded upon on in the next section.

Typically, the gyrofrequency is much faster than the time-scales of interest for turbulent transport, so instead of solving explicitly for the gyromotion in the particle equations of motion, instead this motion could be averaged over. This averaging procedure results in gyrokinetics [12], which evolves rings of charge as they follow along magnetic field lines. μ serves as the adiabatic invariant associated with the gyromotion, and the resulting gyroaveraged equations do not depend on the gyrophase, so we move from solving the Boltzmann equation in the full 6-D phase space to a reduced 5-D phase space, where only 4 of the phase space coordinates will need to be evolved. These 4 coordinates are typically $(\mathbf{X}_{gy}, p_\parallel)$, which correspond to the gyrocenter position and the particle parallel momentum. Different types of gyrokinetics also sometimes include different orderings on the electromagnetic fields. In this thesis we focus primarily on electrostatic fluctuations $(\delta\phi)$, although we also keep shear-Alfvénic fluctuations $(\delta A_\parallel)$ in simulations.

Considering the typical velocities, length scales, and timescales will give us insight into which fluctuations we will expect to be the most important. The fast streaming of particles along magnetic field lines compared to motion across field lines suggests that fluctuations will primarily be field-aligned, so $k_\parallel \ll k_\perp$. We consider transport away from low-order rational surfaces, and assume macroscopic plasma stability (captured by MHD stability), so $k_\perp a \gg 1$. We distinguish two length scales, $\rho_i \equiv v_{ti}/\Omega_{ci}$ and $\rho_e \equiv v_{te}/\Omega_{ce}$, which correspond to the typical gyroradius of an ion and electron, respectively. Fluctuations with smaller length scale than these gyroradii will tend to be averaged out by the gyromotion, so we identify $k_\perp \rho_i \lesssim 1$ with ion-scale turbulence and $k_\perp \rho_e \lesssim 1$ with electron-scale turbulence. Finally, we note that the Alfvén velocity typically satisfies $v_A \equiv \frac{B}{\sqrt{\mu_0 n m_i}} \gg v_{ti} \sim c_s$, where $c_s \equiv \sqrt{T_e/m_i}$ is the ion sound velocity. Thus Alfvén waves do not strongly couple to ion acoustic waves, so for ion-scale turbulence we primarily consider electrostatic modes. While it is possible for electron-scale modes have a stronger electromagnetic character, the distinction will not play a large role.

One final note about single particle motion specific to tokamak geometry is the distinction between trapped and passing particle trajectories. Due to the magnetic mirror force, which arises from an effective potential μB of a dipole aligned to the magnetic field, particles with low enough parallel kinetic energy can be trapped in regions of low magnetic field. For a tokamak, the low-field side is at larger major radius, and separates particles into topologically distinct passing and trapped orbits. The trapped particle trajectories form a banana shape in the poloidal plane, and hence are usually referred to as banana orbits. See Figure 2-2 for an illustration of these orbits.

Since the low-field side typically also corresponds to the region of bad curvature,

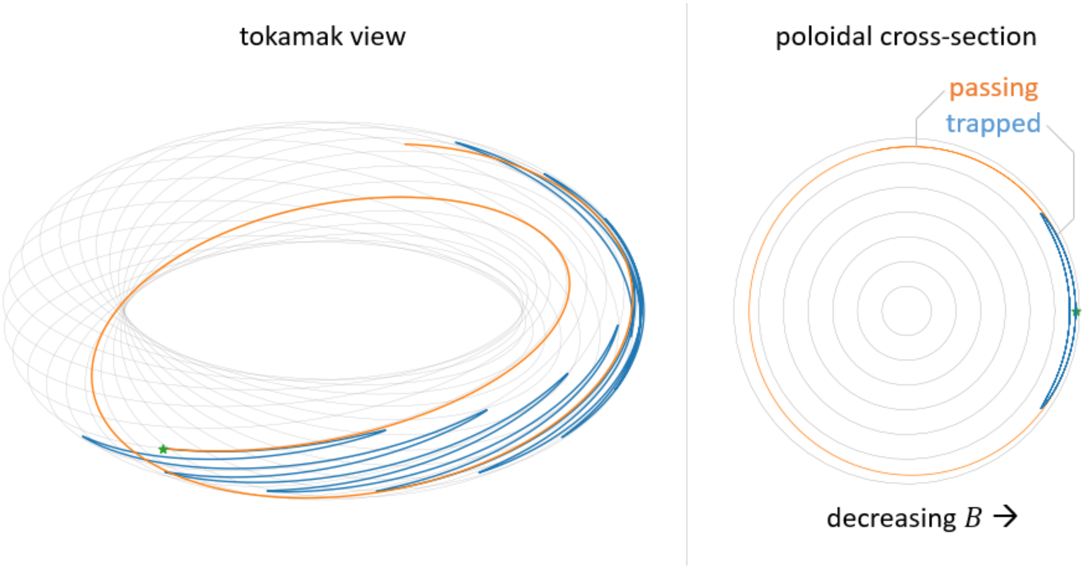

Figure 2-2: Figure showing the trajectory of two particles starting from the same position, marked in green, but with different initial parallel kinetic energy, leading to topologically distinct orbits. (Left) shows motion in the tokamak. (Right) shows the trace of the orbit in the poloidal plane, with the blue trapped particle orbit forming a banana shape.

new types of drift-wave instabilities can arise from the dynamics of these trapped particles. Since the dominant effect of collisions tends to be pitch-angle scattering, these trapped orbits are particularly sensitive to collisions. In this thesis we will focus on trapped electrons, which introduce a new length scale, the typical banana orbit width:

$$\Delta r_b = \epsilon^{1/2} \rho_e \frac{B}{B_p} \tag{2.5}$$

where $\epsilon = r/R$ is the inverse aspect ratio, and B_p is the poloidal magnetic field magnitude. It also introduces a new time scale, the bounce frequency

$$\omega_{be} = \frac{v_{te}}{qR} \epsilon^{1/2} \tag{2.6}$$

where q is the magnetic safety factor, which captures the ratio of the toroidal winding number to poloidal winding number for magnetic field lines on a flux surface. We define the collisionality to be a normalized measure of the collision frequency [55],

$$\nu_* \equiv \frac{\nu_{ee}/\epsilon}{\omega_{be}} \tag{2.7}$$

where the numerator $\nu_{eff} \equiv \nu_{ee}/\epsilon$ is the time it takes for collisions to scatter the electron pitch angle by $\sim \epsilon$, and hence scatter out of the trapped particle orbit. If $\nu_* \ll 1$ then most trapped electrons will complete their orbits. However, if $\nu_* \gtrsim 1$, then electrons will be scattered out of trapped orbits before they can complete them, removing the topological distinction between trapped and passing electrons. For $T_e \sim T_i$ usually $\rho_i \gg \Delta r_b \gg \rho_e$.

2.2 Collective Plasma Flows: Drift Wave Instabilities and Zonal Flows

This subsection will review the three main drift wave instabilities which will be considered in this thesis: the ion temperature gradient (ITG), trapped electron mode (TEM), and electron temperature gradient (ETG) instabilities. This subsection will also briefly introduce zonal flows (ZFs), which are important because they provide a mechanism by which drift wave fluctuations can be sheared to smaller scales, while being benign to transport in the sense that they do not directly drive turbulent fluxes.

To understand plasma drift wave instabilities and zonal flows, we introduce the paradigmatic example of drift-Rossby waves in the Charney-Hasegawa-Mima equation [25]. This situation models a slab geometry with fixed density gradient scale length in the x direction, no temperature gradients, electrostatic perturbations, cold ions, and adiabatic electrons. Written in dimensionless form,

$$\frac{\partial q}{\partial t} + \mathbf{v}_E \cdot \nabla q = 0 \tag{2.8}$$

$$q = \nabla^2 \psi - \frac{1}{\rho_s^2}\tilde{\psi} + \beta x \tag{2.9}$$

$$\mathbf{v}_E = \left(-\frac{\partial \psi}{\partial y}, \frac{\partial \psi}{\partial x} \right) \tag{2.10}$$

here ψ is a normalized electrostatic potential, and the equations are written in the form of an advection equation for q, the potential vorticity. In geophysical dynamics, the β comes from the "beta plane approximation" which is a linear approximation to the change in the vertical component of the planetary vorticity a fluid parcel experiences as it moves from one latitude to another, here corresponding to movement in the variable x. To conserve angular momentum, motion of a fluid parcel from one latitude to another must be compensated by a change in either the relative vortex motion of the parcel (corresponding to the $\nabla^2\psi$ term), or by a change in vorticity through internal vertical vortex stretching (corresponding to the $-\psi/\rho_s^2$ term). For reference, ρ_s would refer to the Rossby deformation radius in geophysics. In tokamaks similar arguments can be made with the 'ion plasma absolute vorticity' [52]. In this case $\beta = \mathrm{v}_*/\rho_s^2$, where v_* is the diamagnetic drift (2.4) due to the density gradients only, and ρ_s is the ion sound gyroradius. The connection with geophysical fluid dynamics has been a source of cross-fertilization between fields.

Note additionally the presence of $\tilde{\psi} = \psi - \langle\psi\rangle$ in the equation for the potential vorticity. Here $\langle\cdot\rangle$ is the zonal average, corresponding to an average in y, which would be the poloidal direction in a tokamak. This is necessary because the electron adiabatic response is a result of fast parallel streaming of electrons along magnetic field lines. Electrostatic potential fluctuations which are constant along field lines, which in tokamaks would be poloidally constant, do not exert a parallel force on the electrons and hence will not lead to an electron adiabatic response. This is important for zonal flows, which have constant ψ perturbations on flux surfaces, and hence only enter the potential vorticity through $\nabla^2\psi$ and not $-\frac{1}{\rho_s^2}\tilde{\psi}$.

By linearizing this equation around a flow-free base state $\psi = 0$ and solving for the eigenmodes, we find the existence of drift waves, which satisfy a dispersion relation

$$\omega_k = \frac{k_y \mathrm{v}_*}{1 + k_\perp^2 \rho_s^2} \tag{2.11}$$

The basic mechanism is illustrated in Figure 2-3. Perturbations to the plasma density lead to perturbations in the electrostatic potential, which then lead to $E \times B$

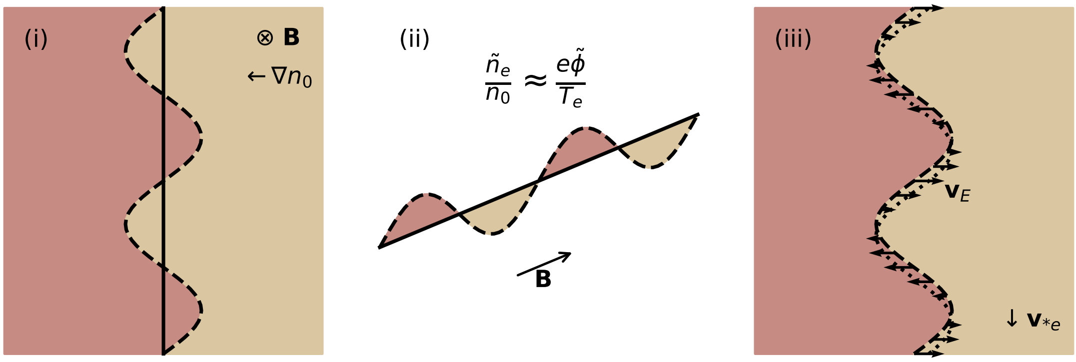

Figure 2-3: Demonstration of the basic plasma drift wave mechanism in the Charney-Hasegawa-Mima equation. (i) A density perturbation (dashed line) is imposed on a background density gradient, leading to a periodic excess/deficiency of ion density compared to the original iso-density surface (solid line). (ii) With a small but finite $k_{\|}$, an electrostatic potential $\tilde{\phi}$ forms along magnetic field lines to maintain quasineutrality between the cold ions and fast parallel streaming electrons via the electron adiabatic response. (iii) The resulting $E \times B$ drifts flow cause the density perturbation to drift downward (dotted line), in the electron diamagnetic drift direction $\mathbf{v}_{*e}$.

drifts causing the perturbations to drift in the diamagnetic drift direction. Since the electrostatic potential acts as the streamfunction for the flow (2.10), the presence of a density gradient can be thought of as setting up a gradient of potential $E \times B$ flow vorticity. Note that despite the existence of a density gradient, these waves do not lead to transport, because the density perturbations and radial velocity perturbations are 90 deg out of phase.

In order for particles to transfer net energy to the waves, in tokamaks typically a wave-particle resonance is invoked. The most basic wave-particle resonance comes in the form of Landau damping, which intuitively involves particles 'surfing' an electrostatic wave, as illustrated in Figure 2-4. The wave will either be damped or unstable depending on whether particles on average pick up energy from, or lose energy to the wave. The different instabilities present in tokamaks reflect the variety of waves that are supported by the plasma, and the variety of mechanisms by which particles can transfer energy to the waves. The instabilities covered in this thesis are categorized by whether they are supported by either ion diamagnetic direction drift waves, or electron diamagnetic direction drift waves, and whether or not trapped particle dynamics are important to destabilizing the wave.

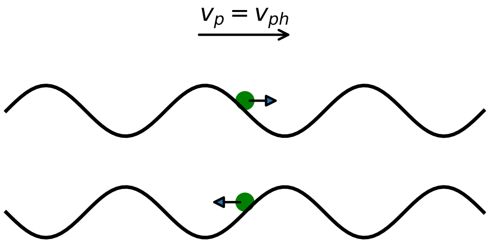

Figure 2-4: Figure showing mechanism of Landau damping and inverse Landau damping. For particles with velocity v_p approximately equal to the phase velocity v_{ph} of an electrostatic wave, the waveform of electrostatic potential is approximately constant in the frame moving with the particle. The top particle receives energy from the wave, while the bottom particle transfers energy to the wave.

Ion Temperature Gradient (ITG) Instabilities

ITG instabilities [90] are modes primarily driven by free energy available in the ion temperature gradient, ∇T_i, and typically have phase velocity in the ion diamagnetic drift direction. In a fluid picture, the free energy is converted into flow energy either via expansion in the bad curvature region of tokamaks (where $\nabla p \cdot \nabla B > 0$, typically the low-field outboard side), corresponding to toroidal ITG instabilities, or via coupling to ion acoustic waves as negative compressibility modes [129], corresponding to slab ITG instabilities. Toroidal ITG modes are typically ballooning modes, with greater amplitude on the low-field side. Kinetic effects may become near important near marginality from the curvature and ∇B drift resonance with the perpendicular mode propagation, and parallel streaming resonance with the ion acoustic wave.

ITG instabilities occur primarily at long wavelengths, typically $k_\perp \rho_i \lesssim 1$. In order to excite these modes, there is usually a critical ion temperature gradient scale length $\frac{1}{L_{Ti}} = \frac{\nabla T_i}{T_i}$, which depends on the density gradient scale length $\frac{1}{L_n} = \frac{\nabla n}{n}$ through the ratio $\eta_i = L_n/L_{Ti}$, hence these modes are sometimes also known as η_i instabilities.

Note this implies that density gradients are stabilizing to ITGs. Other major dependencies of the growth rate are the electron to ion temperature ratio T_e/T_i, and main ion dilution ratio n_i/n_e. The growth rate can also be enhanced in the presence of trapped electrons, which contribute a significant non-adiabatic electron response. While ITGs primarily exhaust ion heat fluxes, they can also exhaust significant particle, momentum, and electron heat fluxes.

Trapped Electron Mode (TEM) Instabilities

TEM instabilities [67] are modes primarily driven by free energy available in either the electron density gradient ∇n_e, or electron temperature gradient ∇T_e, and typically have phase velocity in the electron diamagnetic drift direction. TEMs can be destabilized either through collisionless processes (CTEMs) or through dissipative processes (DTEMs). Similar to ITG instabilities, TEMs are also usually ballooning modes. In a fluid picture, for CTEMs the free energy is also converted into flow energy in the bad curvature region of the tokamak, although since trapped electrons bounce-average over a region of a plasma, the criterion is usually expressed in terms of the second adiabatic invariant $J = \oint v_\parallel \, \mathrm{d}l$ (where the integral is taken along the magnetic field line the particle is bouncing on), with instability requiring $\nabla p \cdot \nabla J > 0$. In a kinetic picture, the instability involves wave resonance with the toroidal precession drift resonance of the electron bounce centers (a bounce-averaged remnant of the curvature and ∇B drifts). DTEMs do not require either bad curvature or kinetic resonances to be destabilized, as collisions lead to instability by introducing a phase lag to the electron adiabatic response, similar to resistive drift waves, although here the dissipation is due to the exchange of trapped electrons and passing electrons.

TEMs can be active across a broad range of scales, from the banana width scale $k_\perp \Delta r_b \lesssim 1$, all the way to ion scales including $k_\perp \rho_i \lesssim 1$. Modes with $k_\perp \rho_i \gtrsim 1$ typically have a mostly adiabatic ion response, so they exhaust mostly electron heat flux, although some amount of ion heat and particle fluxes remain up until $k_\perp \rho_i \gg 1$. At ion scales, TEMs can actually have greater growth rates than ITGs for low collisionality ν_* and large T_e/T_i. As the collisionality increases, a larger fraction of trapped electrons will be scattered into passing orbits before they complete an entire banana orbit. CTEMs are stabilized by collisionality. While DTEMs are initially destabilized by small values of the collisionality, as ν_* approaches unity the distinction between trapped and passing electron orbits becomes less important, extinguishing the mechanism of instability. It should also be noted that outside of limiting cases, TEM and ITG do not lie on distinct branches of the dispersion relation, and are smoothly connected as ubiquitous modes, which have nearly zero phase velocity.

Electron Temperature Gradient (ETG) Instabilities

ETG instabilities [56] are modes primarily driven by free energy available in the electron temperature gradient, ∇T_e, and typically have phase velocity in the electron diamagnetic drift direction. ETGs have similar destabilization mechanisms as ITGs, in the sense that they can be destabilized via bad curvature for toroidal ETG, or via coupling to parallel modes for slab ETG. Similarly, they have a critical $\eta_e = L_n/L_{Te}$ threshold. However, ETGs typically occur at $k_\perp \rho_e \lesssim 1$ and $k_\perp \rho_i \gg 1$. Hence, ions are adiabatic, and so ETGs cannot exhaust ion heat fluxes or particle fluxes. This situation is not modified by the presence of trapped ions, as the ion adiabatic response is supported by ion polarization associated to the gyromotion, rather than to perpendicular free streaming. Note that the ETG branch of the dispersion relation smoothly connects to the TEM branch.

Zonal Flows

The final class of collective plasma flow covered in this section is that of zonal flows (ZFs) [28]. Zonal flows are toroidally and poloidally symmetric $n = 0, m = 0$ perturbations of the electrostatic potential, which result in $E \times B$ flows which lie entirely in magnetic flux surfaces. Thus, these flows cannot lead to transport, as there is no radial component to the flow. Zonal flows are a natural consequence of turbulence in tokamaks, as the mixing of potential vorticity necessarily leads to the acceleration of a zonal flow via the Taylor identity [52].

The importance of zonal flows comes from the fact that they regulate drift wave turbulence by shearing apart $E \times B$ eddies. This process is usually described via the process of shear-enhanced decorrelation, in which eddies increase in radial wavenumber until the turbulent diffusivity is strong enough to break apart the eddy. This shearing process leads to eddy tilting, which acts to accelerate the zonal flow, transferring flow energy from the drift wave to the zonal flow. Zonal flows then slowly damp via collisional viscosity. Zonal flows may also be subject to nonlinear flow damping, such as damping via a turbulent viscosity from tertiary instabilities driven by the zonal flows themselves. The drive of tertiary instabilities, such as Kelvin-Helmholtz-like instabilities, represent a return transfer of flow energy from the zonal flows to the drift waves, and would limit the amplitude of the zonal flows. Note that other nonlinear flow damping mechanisms are possible as well, and the relevance of these different mechanisms remains an open question.

2.3 Transport and Saturation in Wave Turbulence

Now that we've discussed how instabilities arise in plasmas, we now need to discuss how these instabilities feed back on the plasma state, that is, what level of transport do these waves cause, and how do the linear instabilities saturate? More subtly, how do the properties of the linear instabilities imprint on the nonlinear state of the plasma, if at all?

As hinted by the focus on linear instabilities in the previous section, turbulence in tokamaks is generally thought to be wave turbulence. Waves in plasmas tend to be dispersive limiting the lifetime of wavepackets, and overall fluctuation levels tend to be weak (e.g. $\tilde{T}_e / \langle T_e \rangle \sim 0.01$ in the core), which suggests the relevance of linear processes in turbulence. Quasilinear theory, to be introduced below, has formed the basis of widely-used reduced transport models in tokamaks such as TGLF and QuaLiKiz. The reasonable accuracy of these codes in situations they are tuned for suggests (although does not prove) the relevance of linear modes to the nonlinear state. Thus, this thesis takes quasilinear fluxes as an assumption. However, since plasmas are driven above the linearly unstable state, the plasma is unable to quasilinearly relax into a linearly stable state. Thus, some prescription is required to determine the saturation amplitude of the linear instabilities.

2.3.1 Quasilinear Theory

Quasilinear theory is the workhorse of plasma turbulence [31]. Its name comes from the usage of the linear response, either directly or as part of a more complex approximation, to describe the dynamics of the fluctuations. While the discussion below is primarily conceptual, Appendix A provides a brief derivation of the turbulent flux calculation in quasilinear theory for a generic system.

The main concept from quasilinear theory employed in this thesis consists of the quasilinear weights. To define the quasilinear weights, consider for example the turbulent electron heat flux in a Reynolds-averaged fluid model,

$$Q_e(x,t) = \left\langle \tilde{T}_e(x,t)\tilde{v}_r(x,t) \right\rangle \tag{2.12}$$

This is a second-order moment involving two independent fields (temperature and radial velocity), which both vary as a function of space and time. The core of quasilinear theory is to assume the appropriateness of the linear response to describe the dynamics of the fluctuations. For example we might be able to express both the temperature as linear functionals of the electrostatic potential:

$$\tilde{T}_e(x,t) = \int \mathrm{d}x' \, \mathrm{d}t' \, \mathcal{R}_{T_e}(x,t;x',t')\tilde{\phi}(x',t') \tag{2.13}$$

Typically, the linear response functional is diagonalized in an eigenmode basis. In some situations it is useful to also allow non-eigenmodes as is the case for Landau modes, which are not true eigenmodes of the system, but diagonalize the linear response in the time-asymptotic limit of phase mixing as shown by Van Kampen [68]. In this case we can express any fluctuation as a sum over eigenmodes,

$$\tilde{T}_e(x,t) = \sum_{\mathbf{k}} \tilde{T}_{e,\mathbf{k}} g_{\mathbf{k}}(x) e^{-i\omega_{\mathbf{k}} t} \tag{2.14}$$

where $\mathbf{k}$ is an abstract eigenmode index, and $g_{\mathbf{k}}(x)$ is a function describing the eigenmode shape. In translation-invariant systems, these functions correspond to the Fourier basis $g_{\vec{k}}(x) = e^{i\vec{k}\cdot\vec{x}}$, but the sum may involve multiple eigenmodes for each wavenumber $\vec{k}$. For tokamaks, this sum is typically over n, the toroidal wave number, usually expressed in terms of the poloidal wavenumber $k_\theta = qn/r$.

Plugging equation (2.14) into (2.13) implies

$$\tilde{T}_{e,\mathbf{k}} = \mathcal{R}_{T_e,\mathbf{k}} \tilde{\phi}_{\mathbf{k}} \tag{2.15}$$

where the $\mathcal{R}_{T_e,\mathbf{k}}$ are complex numbers. A similar result for the radial velocity field will hold, which allows us to write turbulent fluxes as

$$Q_e = \sum_{\mathbf{k}} W_{Q_e,\mathbf{k}} \left\langle \bar{\phi}_{\mathbf{k}}^2 \right\rangle \tag{2.16}$$

Here, $W_{Q_e,\mathbf{k}}$ is called the quasilinear weight, and determines how much the eigenmode will contribute to transport purely due to the linear response, while $\left\langle \bar{\phi}_{\mathbf{k}}^2 \right\rangle$ is called the spectral weight, and represents the amplitude of the eigenmode. The quasilinear weight is determined entirely by the linear response, and hence can be calculated purely through linear theory. However, the spectral weight depends on the wave amplitudes, or equivalently the wave spectrum.

As a sidenote, another way to break down the turbulent fluxes is by using the inequality $\mathrm{Cov}(X,Y)^2 \leq \mathrm{Var}(X)\,\mathrm{Var}(Y)$ between covariances and variances. This implies $\left\langle \tilde{T}_e \tilde{v}_r \right\rangle^2 \leq \left\langle \tilde{T}_e^2 \right\rangle \left\langle \tilde{v}_r^2 \right\rangle$ so we can define a 'cross-phase' which relates the fluctuation strengths to the actual amount of transport,

$$\left\langle \tilde{T}_e \tilde{v}_r \right\rangle = \sqrt{\left\langle \tilde{T}_e^2 \right\rangle \left\langle \tilde{v}_r^2 \right\rangle} \cos \alpha_{T_e,v_r} \tag{2.17}$$

Cross-phases are possibly experimentally accessible, so they can serve as an important check on the quasilinear weights. For example, for fluctuations of a single wavelength, the cross-phase reduces to

$$\cos \alpha_{T_e,v_r} = \mathrm{Re}\left[\frac{\left\langle \tilde{T}_{e,\mathbf{k}} \tilde{v}^*_{r,\mathbf{k}} \right\rangle}{\sqrt{\left\langle \tilde{T}_{e,\mathbf{k}} \right\rangle \left\langle \tilde{v}_{r,\mathbf{k}} \right\rangle}}\right] = \frac{\mathrm{Re}\left[\mathcal{R}_{T_e,\mathbf{k}} \mathcal{R}^*_{v_r,\mathbf{k}}\right]}{|\mathcal{R}_{T_e,\mathbf{k}}||\mathcal{R}_{v_r,\mathbf{k}}|} \tag{2.18}$$

The second important concept from quasilinear theory employed in this thesis regards the bounds of validity for quasilinear theory. While for the most part this thesis takes the validity of quasilinear theory as an assumption, some parts will touch on whether or not this assumption is founded. While the minimally sufficient conditions for the validity of quasilinear theory to hold are not known, one known necessary condition is that the autocorrelation time of the fields seen by resonant particles τ_{ac}, is shorter than the time it takes for the particle to traverse an eddy or complete a 'bounce' in the field pattern τ_S. The symbol τ_S is used here instead of the more usual 'bounce time' τ_b to prevent confusion with the bounce time of particles in banana orbits, and emphasizes that this is an effect relating to the synchronization of a particle with an eikonal phase S. This condition is typically captured via the Kubo number $\mathcal{K} \equiv \tau_{ac}/\tau_S$, with quasilinear theory requiring $\mathcal{K} \ll 1$. The physical content of this condition is that the diffusive processes result from the accumulation of many small independent kicks. If $\mathcal{K} \gtrsim 1$, the kicks cannot be justified to be either independent or small. Appendix A explains this in more quantitative detail, and discusses how quasilinear theory breaks down if this necessary condition is not met. Chapter 7 will address this point in more detail for drift waves.

2.3.2 Saturation

In a sense, quasilinear theory provides a way to relate any second-order moment (e.g. the turbulent heat flux $\left\langle \tilde{T}_e \tilde{v}_r \right\rangle$) to the wave spectrum, which can be represented by the second-order moment of a fluctuating field (e.g. $\left\langle \tilde{\phi}^2_k \right\rangle$), or more generally to any quadratic quantity associated to the waves such as the wave action. In 'pure' quasilinear theory, to calculate the evolution of the wave spectrum, we ignore nonlinearities in the time evolution of the wave spectrum, thus assuming growth and damping is purely due to the linear growth rate, i.e.

$$\frac{\partial}{\partial t}\left\langle \tilde{\phi}_k^2 \right\rangle = 2\gamma_k \left\langle \tilde{\phi}_k^2 \right\rangle \tag{2.19}$$

The ultimate outcome of this is a quasilinearly relaxed state – one in which there are no linear instabilities present. However, fusion plasmas in tokamaks are typically driven such that the mean plasma profiles are above marginal stability. Linear instabilities remain present with finite positive growth rates, so the plasma is not in a quasilinearly relaxed state. Thus, nonlinearities in the time evolution of the wave spectrum are required to balance out the pumping of energy into fluctuations by the linear growth rate, seen in equation (2.19), and saturate the instabilities at finite amplitude.

If we wish to include nonlinearities into the evolution of the wave spectrum, we enter the moment hierarchy problem: the evolution of lower-order moments is coupled by the nonlinearity to higher-order moments. For example, for a quadratic nonlinearity, the evolution of the second moments depends on the third moments, which depend on the fourth moments, etc... In order to form a closed system of equations, the moment hierarchy must be either truncated or otherwise approximated at some order. The prescription on how to close the system of equations is known as a closure relation. This is a common theme in many parts of statistical physics. In addition to showing up in such Reynolds-averaged turbulence problems, it also occurs in closure needed when deriving fluid models from kinetic equations since various velocity moments are coupled to each other, or in truncation of BBGKY hierarchy to derive the Boltzmann equation in which the time evolution of the s-particle distribution function depends on the $(s+1)$-particle distribution function.

Needless to say, as an attempt to solve for the statistics of a nonlinear system with an infinite number of degrees of freedom, finding such closure relations is difficult. Progress can be made in certain cases - for example, outside of wave turbulence, the assumption of universality, isotropy, and complete self-similarity in the inertial range results in the famous Kolmogorov 5/3 spectrum $E(k) = C\varepsilon^{2/3}k^{-5/3}$ for 3-D

Navier-Stokes turbulence [71]. Here $E(k)\,\mathrm{d}k$ is the contribution to the kinetic energy from Fourier modes $k < \left|\vec{k}\right| < k + \mathrm{d}k$, ε is the rate of turbulent energy dissipation rate, and C is a universal constant. The physical insight from the form of this spectrum underlies two-equation closure models of Navier-Stokes, such as K-ε or K-ω models [127], which refer to closure models which model the Reynolds stress via an effective eddy viscosity, and evolve two fields corresponding to 'free parameters' of the Kolmogorov spectrum, the mean turbulent kinetic energy K and either the turbulent energy dissipation rate ε or the specific dissipation rate $\omega \propto K/\varepsilon$. For these models, the second-order statistics of the small-scale fluctuations are fully prescribed by the large-scale dynamics of the Reynolds-averaged fields.

For wave turbulence, similar results can be achieved in certain cases. For wave systems which are isotropic and scale-invariant (e.g. the dispersion relation and non-linear interaction coefficients are invariant with respect to rotation, and homogeneous functions of wavenumber), and sufficiently dispersive to allow for a weak turbulence treatment to be used, dimensional arguments can be applied to derive Kolmogorov-Zakharov wave spectra [89]. For strongly anisotropic wave systems such as reduced MHD or strongly rotating turbulence, where a certain direction is special due to the presence of a strong magnetic field or strong rotation, progress can be made in the form of critical balance arguments where linear and non-linear timescales are balanced scale-by-scale to derive anisotropic wave spectra. However, as intimated by the wealth of physics over multiple scales introduced in earlier sections as relevant to tokamak turbulence, analytic progress is significantly more difficult in trying to describe tokamak turbulence. There are other methods to describe the evolution or saturation of wave spectra used in tokamaks. Examples include wave kinetic approaches, which are successful in describing the saturation of drift waves via shearing from zonal flows in the adiabatic limit of large scale separation between zonal flows and drift waves [28], or propagator renormalization theories [36]. However, these approaches will not be covered in this thesis.

Returning to quasilinear theory, in lieu of a satisfactory analytic approach to solve the closure problem, approximate saturation rules are a major component to modern quasilinear transport codes. For example, a heuristic estimate of the saturation level can be constructed the linear growth time by an eddy turnover time using the root mean square fluctuating $E \times B$ velocity $\tilde{v}_{E,rms} = \sqrt{\langle \tilde{v}_E^2 \rangle}$,

$$\gamma_{max} \sim \tau_{eddy}^{-1} \sim \bar{k}_r \tilde{v}_{E,rms} \sim \frac{\bar{k}_r \bar{k}_\theta \tilde{\phi}_{rms}}{B} \tag{2.20}$$

which when taking $\bar{k}_r \sim \bar{k}_\theta \sim \bar{k}_\perp$ reproduces the familiar mixing length estimate $\tilde{\phi}_{rms} \sim \gamma_{max}/\bar{k}_\perp^2$ [45]. Codes such as TGLF [111] and QuaLiKiz [10] calculate turbulent fluxes by finding or approximating eigenmodes of the gyrofluid and gyrokinetic equations, respectively, to get quasilinear weights, then applying a saturation rule to get the wave spectra for the spectral weights. Current saturation rules tend to be empirical, with free parameters which are fit to reproduce observed spectra and transport from nonlinear gyrokinetic simulations.

Part of this thesis is motivated by an ‘inverse problem’ of quasilinear transport. The quasilinear weights, as the output of a linear eigenmode calculation, are well-characterized. Instead of using spectral weights calculated from a saturation rule to calculate the transport, instead we can use the total transport inferred from experiments as a constraint on the possible spectral weights. If the assumption that the quasilinear weights provide an adequate description of the transport holds, then this constraint method provides a way to probe the saturation physics of the eigenmodes if we can construct an experimental situation where we expect the linear spectrum to be the same, but the nonlinearly saturated amplitudes to be different. The hysteresis experiments presented in this thesis provide such an experimental situation.

2.4 Topics of Specific Interest to Addressing Turbulence Transitions

As discussed in the introduction, this thesis focuses on two specific transitions in tokamak L-mode plasmas, the Linear to Saturated Ohmic Confinement (LOC/SOC) transition and concomitant intrinsic rotation reversal. A natural question would be how these empirically observed transitions can be described in terms of the wave turbulence concepts introduced earlier in this chapter. This section discusses how the physical concepts make contact with the experimental phenomenology.

2.4.1 General Picture of Momentum Transport in Tokamaks

This thesis will not cover the details of momentum transport or generation. However, some concepts from momentum transport specific to tokamaks are used in the arguments made in the research. This section covers the basic material on momentum transport relevant to these arguments.

In general, the flux of toroidal kinetic momentum in the radial direction, or equivalently the $r\phi$-component of the stress tensor, can be written in the following form:

$$\Pi_{r\phi} \equiv \langle \tilde{v}_r \tilde{p}_\phi \rangle = m_i \left[\langle n \rangle \langle \tilde{v}_r \tilde{v}_\phi \rangle + \langle \tilde{n} \tilde{v}_r \rangle \langle v_\phi \rangle + \langle \tilde{n} \tilde{v}_r \tilde{v}_\phi \rangle \right] \tag{2.21}$$

where $\tilde{p}_\phi$ is the fluctuating component of the toroidal kinetic momentum, and $\langle v_r \rangle = 0$ is used. The first term is familiar from incompressible fluid physics, and is called the Reynolds stress. The second term is the convection term since it relates to the transport of momentum due to the net transport of plasma density via $\langle \tilde{n} \tilde{v}_r \rangle$. We will not discuss it here, since it necessarily leads to a flux in the form of a momentum pinch since it is proportional to $\langle v_\phi \rangle$. Finally, the third term corresponds to a triplet correlator. Very little is understood of it, and it might be expected to be smaller than the other other two terms outside of strong turbulence regimes since it is the product of three, rather than two, fluctuating terms.

The Reynolds stress (properly a stress density since it is divided through by the average density, but the distinction is not important here) can be further broken into several components as

$$\langle \tilde{v}_r \tilde{v}_\phi \rangle = -\chi_\phi \frac{\partial \langle v_\phi \rangle}{\partial r} + V \langle v_\phi \rangle + \pi^R_{r\phi} \tag{2.22}$$

The first and second terms correspond to diffusive and pinch terms. The third term is called the residual stress, and contains the parts of the Reynolds stress which is not proportional to either the gradient of the toroidal velocity (Fick's law diffusion), or the toroidal velocity (momentum pinch) itself. The importance of this term comes from the fact that intrinsically driven rotation profiles are observed to cross through zero velocity with a non-zero gradient in velocity, and hence cannot be held in steady-state through the balance of momentum pinch and diffusion terms alone. Since there are no external momentum sources in the core, the profiles require drive in the form of residual stress. The divergence of the residual stress acts as a torque which can accelerate the plasma to a non-zero rotation. Since this residual stress can involve the transport of momentum against a rotation gradient, the requirement for net positive entropy generation by the system requires up-gradient a residual stress to be linked to some down-gradient transport of heat or particles [72]. This corresponds to off-diagonal transport of momentum, since these fluxes result from gradients of other thermodynamic variables, such as temperature or density.

In addition to momentum transport due to Reynolds stress, net plasma flows can also form due to turbulent acceleration [122, 123]. The turbulent acceleration is a source or sink of parallel flow which cannot be written as the divergence of a parallel Reynolds stress. The existence of such a source or sink does not contradict momentum conservation: while the kinetic momentum of the plasma is mainly carried by ions, the momentum conservation law in tokamaks applies to the total canonical momentum, which is the sum over the momenta of all species and the field momentum. Thus, a net turbulent acceleration would correspond to the net transfer of momentum from particles to the waves.

The form of both the residual stress and the turbulent acceleration are constrained by symmetries obeyed by the plasma dynamics. Most models of gyrokinetics have a certain parity symmetry which has important consequences on momentum transport. The basic idea is that for axisymmetric confined plasmas in the absence of background flows (and flow shears), and in mirror-symmetric geometries, there exists a certain parity transformation obeyed by the equations of motion which reverses the sign of the leading order momentum fluxes in the gyrokinetic ordering. Thus for saturated states of turbulence which statistically obey this symmetry, the leading order momentum fluxes cancel out. As a consequence, driving a net non-zero residual stress requires a combination of both radial inhomogeneity and broken symmetry. As a sidenote, since symmetry breaking mechanisms tend to be weak, this parity symmetry also causes difficulties in calculating the time evolution of the long-wavelength radial electric field, which necessitates workarounds when trying to calculate the toroidal rotation from gyrokinetic simulations [92].

While this thesis will not address the question of the symmetry breaking mechanism responsible for momentum transport in L-mode, it will provide a candidate theory for how a momentum transport bifurcation could relate to changes in the underlying microturbulence. The combination of radial inhomogeneity with broken symmetry leading to large-scale self-generated structure is not unique to L-mode intrinsic rotation, and is reminiscent of solar differential rotation and the dynamo. In addition, turbulent Reynolds stresses are thought to trigger the L-H transition, and lead to shear layer and pedestal formation. In all these cases, the process of structure formation modifies the turbulence population. The thesis will draw analogy between these transitions to provide insight on the problem of the LOC/SOC transition and concomitant intrinsic rotation reversal.

2.4.2 Role of TEM/ITG in LOC/SOC and Rotation Reversal

The conventional argument for why LOC/SOC is observed as the density increases is as follows: Ohmic heating primarily deposits power into the electrons. At low collisionality, the ions and electrons are only weakly thermally coupled, and TEMs are particularly virulent, leading to poor confinement. As the density increases, the collisionality serves both to improve the coupling of ions and electrons, and to decrease the growth rate of TEMs through collisional detrapping of electrons. Main ion dilution $1-(n_D/n_e)$ also tends to decrease and T_e/T_i approaches 1 with increasing plasma density, leading to increased ITG growth rates. The critical density is seen to increase with increasing plasma current I_p. Thus it has been suggested the critical density corresponds to a critical collisionality $\nu_* = (\nu_{ei}/\epsilon)/\omega_{be}$, where ω_{be} is the bounce time of electron banana orbits caused by trapping in the magnetic well, and ν_{ei}/ϵ corresponds to the rate of electron detrapping due to collisions. The TEM/ITG transition picture supposes that once the LOC/SOC transition density is reached, ITGs overtake TEMs as the key contributor to the confinement scaling, as increasing collisionality does not have as large of an effect on the ITG drive. It is argued that since ITG will tend to pin ion temperature gradients near marginal stability, changes in nonlinear mode couplings or saturation of ITG, such as the increasing damping of zonal flows expected at higher collisionality, will not produce a large effect on the gradients leading to confinement scaling saturation. This argument appears to agree with reduced modeling of LOC/SOC both using analytic estimates of transport [107] and using TGLF [41, 50]. The roles of TEM and ITG instabilities are also implicated in producing the observed change in core temperature response to edge cold pulses in perturbative laser blow off injection experiments in Ohmic plasmas, where a gradual transition from TEM to ITG dominance correlates with the experimentally observed trend of transition from core non-diffusive temperature inversion response to core cooling response [105, 106].

The connection between drift wave mode and the rotation reversal is less clear. It is known that the profiles of intrinsic rotation observed in L-mode plasmas cannot be explained through purely diffusive and convective models, and require some form of residual stress or turbulent acceleration to explain. Net generation of either requires the breaking of a parity symmetry obeyed by lowest order local gyrokinetics [93, 30, 122]. This is a broad and subtle topic, and the reader is directed to several recent reviews for an understanding of this topic [94, 32, 13]. Generally, it is expected that TEM and ITG should have different signs of residual stress due to the opposite sign of their group velocities. Additionally, ITG is predicted to produce a non-zero turbulent acceleration [122], while CTEM does not produce any turbulent acceleration [123]. While simulations show a flip in rotation from TEM dominated plasmas to ITG dominated plasmas [124, 78], it is unclear how this connects to the experimentally observed rotation reversal. Recent simulations with global gyrokinetic codes have been able to reproduce the shape and magnitude of observed rotation profiles from experimental input profiles [51, 57], and show both flat and hollow rotation profiles in plasmas which are linearly ITG dominant. Additional insight is needed to explain how or if the TEM/ITG transition picture for energy confinement underlies the rotation reversal, and provide a basis for predicting the critical transition densities.

The connection between linear stability and drift wave mode change is also subtle. It is generally difficult to precisely characterize the linear stability state of the plasma due to experimental uncertainty in the measured plasma profiles and gradients. Typically when the rotation reversal occurs, it is found that ITG is the dominant linear instability at nominal gradient values in the radial locations where the toroidal rotation gradient changes. However, typically variations of the driving gradients of 10 to 20% can lead to TEMs being the dominant linear instability, which are within 1 to 2σ of uncertainty around the inferred mean gradients. Experimentally, some changes in turbulent fluctuations have been observed when crossing the LOC/SOC boundary and the rotation reversal. On JET and Tore Supra, changes in reflectometry measurements, through synthetic diagnostics and nonlinear simulation, have been identified to correspond to the presence of a quasi-coherent TEM (QC-TEM) feature in LOC, which disappears upon transition into SOC [2, 24]. It was noted in these studies that the QC-TEM feature depended not just on the presence of TEM, but also on the saturated state of the turbulence. Changes in fluctuations have also been seen on Alcator C-Mod. This thesis will demonstrate how changes in turbulent fluctuation are seen at experimentally indistinguishable density and temperature profiles, and that circumstantial evidence supports an interpretation of these changes reflecting changes in the underlying turbulence.

Chapter 3

X-ray Imaging Crystal Spectroscopy on Alcator C-Mod

This thesis relies on ion temperature and velocity measurements from an X-ray imaging crystal spectroscopy (XICS) system installed on Alcator C-Mod, HIgh REsolution X-ray spectrometer with Spatial Resolution (HIREXSR) [60]. These measurements are provided by capturing and analyzing the atomic line spectra of impurities introduced into the plasma, typically argon. The developments of Chapter 4 on uncertainty quantification of overlapping chord-integrated spectral lines were made to better characterize data from this diagnostic. This chapter will cover parts of the diagnostic relevant to this thesis.

3.1 Spectrometer Hardware and Viewing Geometry

X-ray imaging crystal spectroscopy (XICS) refers to the usage of x-ray imaging detectors, capable of capturing 2-D arrays of x-ray photon counts, to measure spatially-resolved x-ray spectra emitted by the plasma. The spectra are wavelength resolved via Bragg reflection off a crystal. One axis of the detector is responsible for spatial resolution, and the other axis responsible for wavelength resolution. As will be explained in Section 3.2, this allows for the reconstruction of 1-D profile data, such as impurity ion temperature and rotation, that are accessible to spectroscopic measure-

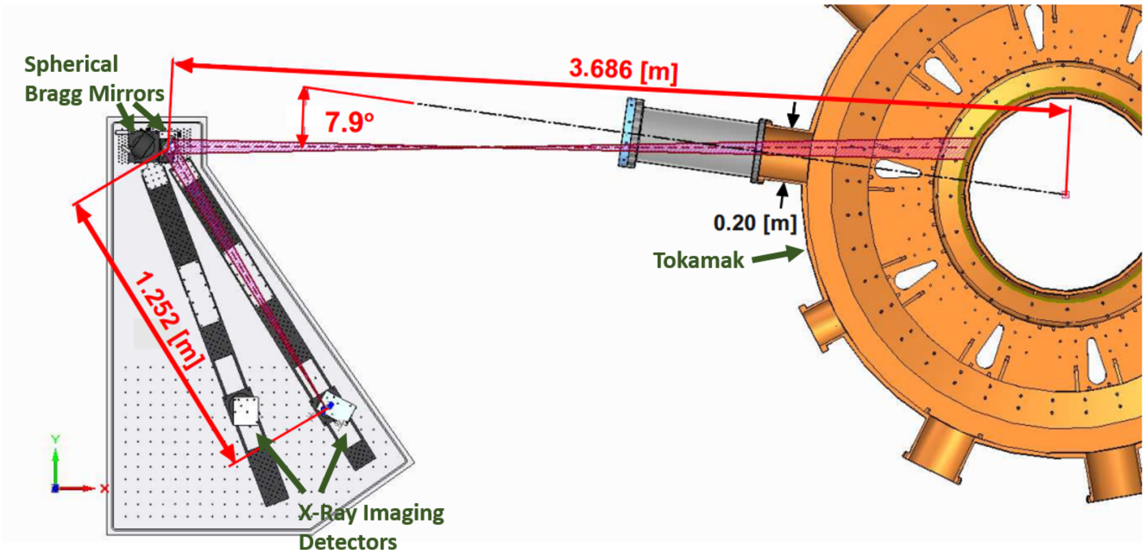

Figure 3-1: A top-down rendering of the spectrometer in place next to the tokamak, with major components labeled. Two arrays of detectors and two spherical Bragg mirrors are used. An example viewing cone from a detector pixel is shown in magenta. Figure from [60]

ments. This section briefly describes the physical characteristics of the spectrometer that makes these measurements possible.

3.1.1 Hardware Layout

A top-down view of the spectrometer is shown in Figure 3-1, showing the general layout of the diagnostic.

The Bragg mirrors, typically made of quartz, only allow reflection of photons of a certain wavelength at angles that satisfy the Bragg reflection rule, $n\lambda = 2d\sin(\theta)$, illustrated in Figure 3-2. Radiation that meets this selection rule will constructively interfere upon reflection and hence be visible, while radiation that does not will destructively interfere and not be visible. Hence, the wavelength of radiation captured by each detector pixel will depend on the angle of incidence of the sightline connecting the pixel to the mirror surface.

The detectors themselves are PILATUS x-ray imaging detectors [37]. The detectors are an array of 487×187 pixels, each of area 172 μm^2, which act as individual photon counters for photons with an energy above a user-configured threshold. Since

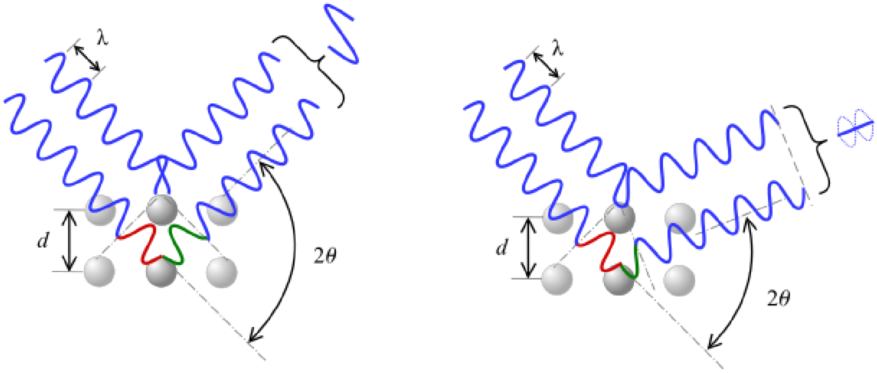

Figure 3-2: Illustration of the Bragg reflection selection rule. In the left figure, the bottom wave travels an integer number of additional wavelengths compared to the top wave, leading to constructive interference. In the right figure, the bottom wave travels an extra half wavelength, leading to destructive interference. Figure from Wikimedia Commons, `https://commons.wikimedia.org/wiki/File:Braggs_Law.svg`

the crystal provides wavelength resolution, only the count rate is needed. The detector is capable of reaching frame rates of 200 Hz, providing sufficient time resolution for many phenomena of interest.

3.1.2 Viewing Geometry

HIREXSR is a Johann spectrometer [66], in which the Bragg mirror is spherically bent in order to focus radiation from the plasma on the detector with minimal aberration. This situation is shown in Figure 3-3.

Consider a plane formed by a pixel on the detector, the center of the mirror, the reflection off the mirror of the sightline connecting the pixel to the center of the mirror. Call this the meridional plane. For a small spherically bent mirror with radius of curvature R_m, in the sense of solid angle visible from the detector, there exists a set of points in the meridional plane called the Rowland circle, which is a circle of radius $R_m/2$ which is tangent to the center of the mirror. Sightlines emanating from points on this circle will have approximately the same angle of incidence on the Bragg mirror, and hence will only see approximately one wavelength of radiation reflected by the mirror, minimizing chromatic aberration. Sightlines passing through different

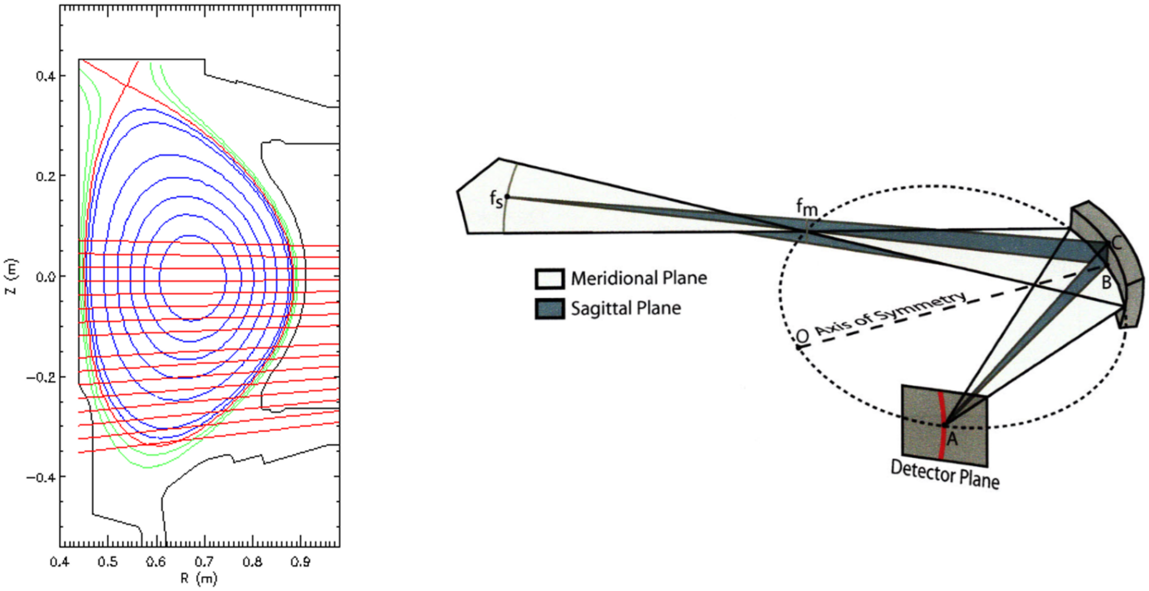

Figure 3-3: (Left) Different chords into the plasma cross-section corresponding to the same wavelength, for the configuration used in the experiments in this thesis. (Right) Geometry of a Johann spectrometer, with the Rowland circle shown using a dotted line. Points highlighted in red on the detector will see approximately the same wavelength of photons, but will collect from different chords as seen in the left figure. Figure from [60]

points on the circle will correspond to different wavelengths. By rotating a sightline about an axis that connects the center of the mirror to the center of curvature of the mirror, we see that it traces out a cone. Where this cone intersects the detector plane will correspond to pixels that measure the same wavelength, but from different spatial chords in the plasma.

As a result of the viewing geometry, the measured photon spectra are chord-integrated across different flux surfaces in the plasma. Thus, tomographic inversion is needed to produce local measurements of ion profiles.

3.2 Analysis of HIREXSR Data

Example HIREXSR data from an array of three PILATUS detectors is shown in Figure 3-4, corresponding to one branch of the spectrometer. HIREXSR has two branches which allow simultaneous viewing of different charge states of an impurity or different impurities entirely. In this thesis, measurements primarily derive from the He-like spectrum of argon. While the local line emission is approximately Gaussian, the chord-integration makes the resulting spectral lines non-Gaussian. The spectra therefore have to be fitted. This section first covers what the spectra look like and how they are fit. This section then covers the inversion technique.

3.2.1 Fitting of Spectra

A typical spectrum from a single viewing chord is shown in Figure 3-4. Spectral lines corresponding to line radiation emitted by He-like argon are clearly visible. The brightest of these are typically the resonance (w, $1s^2\ {}^1S_0$–$1s2p\ {}^1P_1$, 3949.12 mÅ) and forbidden (z, $1s^2\ {}^1S_0$–$1s2p\ {}^3P_2$, 3994.17 mÅ) lines. Thus, these lines are usually used as the basis for ion temperature and velocity measurements.

The most important broadening mechanisms for these x-ray lines are Doppler broadening, instrumental aberration, and natural line broadening. For medium-Z ions such as calcium and argon, typically the Doppler broadening dominates. It occurs as the result of the Doppler shift, $\Delta\lambda/\lambda = (\mathbf{v} \cdot \hat{\boldsymbol{\ell}})/c$ for emitters $v \ll c$

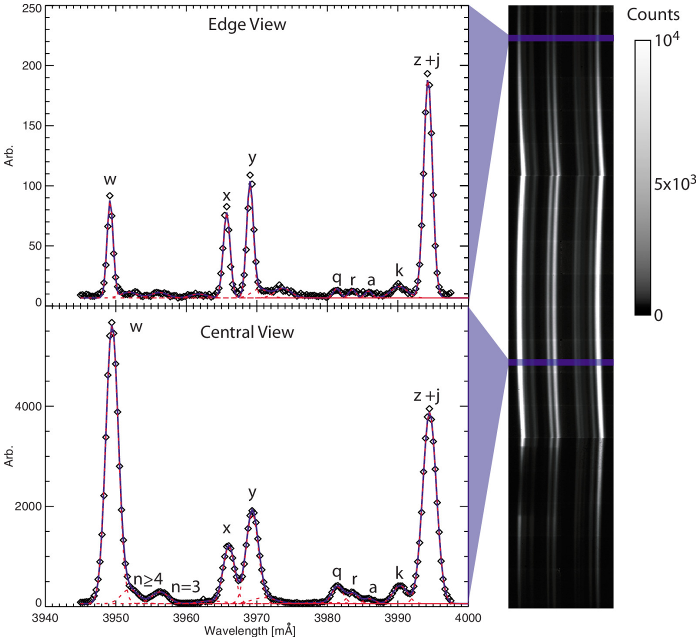

Figure 3-4: Set of three PILATUS detectors showing measured He-like argon spectra from a plasma discharge (right), as well as spectra from two viewing chords through the plasma (left). Figure from [60]

seen from a sightline direction $\hat{\boldsymbol{\ell}}$, averaged over a thermal distribution of emitting ions. Note that since the broadening is a linear function of the velocity, the average broadening is proportional to the average velocity, and the second moment of the broadening is also proportional to the second moment of the velocity (corresponding to the temperature).

The instrumental broadening is also typically non-negligible. It results from the combination of imperfect Bragg reflection from the crystal, displacement of the detector from the Rowland circle, and finite-size mirror effects known as the Johann error. These effects are typically captured via an instrumental function, which is convolved with the 'ideal' measured spectrum to get the spectrum which is actually measured. The instrumental function is typically near-Gaussian, and for lines which are properly in focus contributes an effective broadening of ~ 120 eV.

Finally, the natural line broadening is a result of the uncertainty principle, and the finite transition rate which causes the emission. It takes the form of a Lorentzian broadening, and is typically negligible for the atomic lines of interest here.

For transport analyses, we are usually interested in local measurements of the ion velocity and temperature. As will be discussed in the next section, these can be inferred via a tomographic inversion of the moments of the chord-integrated spectral line shapes. The zeroth moment corresponds roughly to a chord-integrated emissivity, the first moment to chord-integrated velocity, and the second moment to chord-integrated temperature. For a single isolated spectral line, these moments can be calculated directly by integrating over the spectrum after removing the x-ray background noise, assumed to have approximately constant emissivity over the wavelength range of interest. However, in the case of overlapping spectral lines, this direct integration approach no longer works, as the contributions from the two lines need to be separated. This is typically done by a nonlinear fitting routine to find a best-fit Gaussian to the unwanted spectral lines, then subtracting it out. However, this approach is not ideal as the line shapes typically deviate from being purely Gaussian, and furthermore the usage of nonlinear fitting makes uncertainty quantification difficult. The next chapter introduces a new technique developed to deal with these issues.

3.2.2 Profile Inversion

Note that tomographic inversion of HIREXSR is a well-studied problem, and is done through a code known as The Hirexsr Analysis COde (THACO) [97]. This section will sketch out the steps for profile inversion.

The tomographic inversion technique relies on two parts. The first part is the fact that the ion and electron temperature T_i, T_e, and electron density n_e are flux functions, and furthermore that the lowest-order neoclassical flows can be expressed in terms of flux functions, $\omega(\psi)$ the toroidal rotation and $u(\psi)$ the parallel flow. For atomic transitions excited by electron impact or recombination, the emissivity will be a function of n_e, T_e, and n_z, the emitting ion density. If the emissivity ε were also a flux function, since flux functions are 1-D, the effective 1-D spatial resolution of the spectrometer would be sufficient to determine the local emissivity, flow, and temperature functions. The flux function assumption can be relaxed somewhat by adding $\sin(\theta)$ and $\cos(\theta)$ variation, where θ is the poloidal angle. This may be important near the edge, see [104], but is typically better satisfied in the core.

The second part is a set of statistical results for mixture distributions. A mixture distribution is a probability distribution of a random variable which is randomly drawn from a distribution which itself is randomly drawn from a collection of distributions. In this case the random variable is the wavelength X of a photon hitting the detector, and the collection of distributions is the collection of Maxwellian distributions of different shifts and widths along a chord of the detector. The different shifts and widths result from different Doppler shift and broadening from spatially varying line-of-sight velocities and temperatures. The relative likelihood of choosing from a particular Maxwellian is weighted by the local emissivity. If the i-th distribution has probability w_i of being chosen, and has mean μ_i and variance σ_i^2, then

$$\mathbb{E}[X] = \mu = \sum_i w_i \mu_i \tag{3.1}$$

$$\mathrm{Var}(X) = \mathbb{E}[(X-\mu)^2] = \sum_i w_i(\sigma_i^2 + \mu_i^2 - \mu^2) \tag{3.2}$$

Note that the mean of the mixture is linear in the mixture means, and that the variance of the mixture is linear in the mixture variances, plus a term given by the variance of the mixture means. By discretizing the geometry along the sightlines, we can express the moments of the chord-integrated spectra in the form of a matrix equation involving the local moments. These equations can then be inverted in a least-squares sense using standard matrix inversion techniques to get radially local profiles of emissivity, ion rotation, and temperature.

Chapter 4

Uncertainty Quantification of Overlapping Chord-Integrated Spectral Lines

It is important to have a careful understanding of statistical uncertainty in order to draw firm conclusions from data. As described earlier in the chapter introducing HIREXSR, due to the non-Gaussian shape of the spectral lines measured by HIREXSR, the spectra need to be fitted in order to extract ion temperature and velocity measurements. This section covers the Bayesian Spectral Fitting Code (BSFC), which was developed as part of this thesis to better quantify the effect of overlapping spectral lines on the uncertainty of these fits. This work was done in collaboration with another student, Francesco Sciortino.

4.1 Bayesian Spectral Fitting Code Method Description

High resolution observations of atomic spectra play a fundamental role in the study of plasma dynamics, particularly in high-temperature fusion plasmas. In this context, the identification and measurement of specific atomic lines can inform analysis of particle, heat and momentum transport through a variety of diagnostics [59]. In particular, Doppler spectroscopy is a common technique to remotely infer density, temperature and velocity along the line of sight of the emitting body. In many cases the object of interest is emitting over its entire volume, and the measured spectra will be line-integrated over the sight-line of the spectrometer. In media where the plasma properties may be spatially varying, such as fusion devices or astrophysical plasmas, this complicates the interpretation of the measured spectra, thus motivating the use of Doppler tomography techniques to provide local measurements.

While several techniques for Doppler tomography exist [97, 91], they typically require the inference of spectral moments from well-isolated spectral lines. The tomography is typically carried out as an inversion technique using the moments (0^{th} moment corresponding to the brightness, 1^{st} moment corresponding to the Doppler shift, and 2^{nd} corresponding to the Doppler width) of the line-integrated spectra. When isolated spectral lines are not available, nonlinear fits can be used to attempt to resolve overlapping lines. However, this approach suffers from the issue that all possible line shapes must be known *a priori*, and must be parameterized with few enough parameters that a nonlinear fit would be successful. Another tomography method is to attempt full forward-modeling of spectra [81]. However, this typically requires precise determination of geometry and involves the simultaneous inference of many parameters. A parameterization for the local plasma profiles must also be made *a priori*. Uncertainty quantification is particularly complex with many of these methods, and poor results can significantly weaken any effort on interpretation of measurements or validation of transport models in fusion devices [69, 49]. These issues motivate a new method for moment estimation of line-integrated spectra.

In this work, we use a Gauss-Hermite polynomial decomposition to extract moments from line spectra without needing an exact parameterization for the line shape. This is combined with Markov Chain Monte Carlo (MCMC) and other sampling techniques to perform Bayesian uncertainty analysis on the estimated moments. The method is then demonstrated in an example application to spectral data from an X-ray Imaging Crystal Spectrometer (XICS) on the Alcator C-Mod tokamak [61].

It is shown that moment estimation methods using nonlinear fitting of Gaussians is insufficient in cases of practical interest, even when one spectral line is dominant, and that the presented method provides both higher-quality moment estimations and better uncertainty quantification.

This section describes the mathematical formulation of our method, implemented in the open-source Bayesian Spectral Fitting Code (BSFC). A Python implementation of our method is publicly available on GitHub[1]. The code is suitable for running on both personal workstations and computing clusters.

Gauss-Hermite Functions

First, we review the basis functions used in BSFC. Typical line-integrated spectra will be the superposition of Voigt line shapes from different atomic transitions and different spatial locations. Voigt line shapes are the convolution of a Lorentzian line shape from natural line broadening with a Gaussian line shape from Doppler broadening. If the Doppler broadening dominates the natural line broadening, then the line shapes are expected to be near-Gaussian. This motivates the use of (Probabilist's) Hermite polynomials, which are an orthogonal set of polynomials under a Gaussian weight function, satisfying

$$\begin{aligned} \langle He_m, He_n \rangle &\equiv \int_{-\infty}^{\infty} e^{-\frac{x^2}{2}} He_m(x) He_n(x)\ dx \\ &= \sqrt{2\pi} n! \delta_{nm} \end{aligned} \tag{4.1}$$

The first three Hermite polynomials are

$$\begin{aligned} He_0(x) &= 1 \\ He_1(x) &= x \\ He_2(x) &= x^2 - 1 \end{aligned} \tag{4.2}$$

The Gauss-Hermite functions (sometimes called Hermite functions when defined

---

[1] `https://github.com/Maplenormandy/bsfc`

with the Physicist's Hermite polynomials) are defined as

$$\phi_n(x) = He_n(x)e^{-x^2/2} \tag{4.3}$$

The usefulness of these basis functions for uncertainty quantification has long been recognized (see, for example, [38, 8]). In the context of spectral fitting, they provide the means to simplify the calculation of spectral moments and reduce the computational cost of a truncated polynomial decomposition of line shapes. Since the Hermite polynomials form a complete orthogonal basis, a function $f(x)$ can be formally expanded in terms of Gauss-Hermite functions in the following way:

$$\begin{aligned} f(x) &= h(x)e^{-x^2/2} \\ &= \left(\sum_{j=0}^{\infty} a_j He_j(x)\right) e^{-x^2/2} \\ &= \sum_{j=0}^{\infty} a_j \phi_j(x) \end{aligned} \tag{4.4}$$

Then, the first few unnormalized moments for each line shape are easily calculated using the inner product (4.1),

$$\begin{aligned} m_0 &= \langle 1, h \rangle = \sqrt{2\pi} a_0 \\ m_1 &= \langle x, h \rangle = \sqrt{2\pi} a_1 \\ m_2 &= \left\langle x^2, h \right\rangle = \sqrt{2\pi} a_0 + 2\sqrt{2\pi} a_2 \end{aligned} \tag{4.5}$$

These moments are computed against a Gaussian of unit variance. To appropriately rescale and shift line shapes, a scale factor s and centering λ_c is applied to the physical variables (in this case the wavelength λ) before calculating the moments

$$x = \frac{\lambda - \lambda_c}{s} \tag{4.6}$$

From this we can calculate the physical (unnormalized, centered) moments

$$\begin{aligned} M_0 &= m_0 s \\ M_1 &= m_1 s^2 + M_0 \lambda_c \\ M_2 &= m_2 s^3 \end{aligned} \tag{4.7}$$

Note that one factor of s is due to the rescaling $\lambda \to x$, which changes the area under the curve $\int d\lambda f(\lambda) = s \int dx f(sx + \lambda_c)$, and the other factors of s are due to the change of units adopted.

If absolute diagnostic calibration is available, the value of M_0 can then be processed to infer emitting particle density. In the absence of such calibration, as in the case of XICS at Alcator C-Mod, this step is not possible. However, this does not prevent the inference of physical values of line-of-sight velocity, v_i, and temperature for the measured ion, T_i, using:

$$v_i = \frac{M_1/M_0}{\lambda_0} c \tag{4.8}$$

$$T_i = \frac{M_2/M_0}{\lambda_0^2} m c^2 \tag{4.9}$$

Note that the higher order Hermite coefficients are not involved in the moment calculations at all. One may therefore expect that fitting only low-order Gauss-Hermite functions should be sufficient. We approximate the infinite expansion (4.4) with N terms for each line shape:

$$\begin{aligned} f(x) &\approx \sum_{j=0}^{N} a_j \phi_j(x) \quad (\textit{truncation}) \\ &\approx \sum_{j=0}^{N} \hat{a}_j \phi_j(x) \quad (\textit{aliasing}) \end{aligned} \tag{4.10}$$

where in the first line we showed the truncation, and in the second line we approximated the true coefficients a_j with our estimates $\hat{a}_j$ (the resulting error being referred as *aliasing*).

As described in Section 4.1.2, one significant advantage of a Hermite polynomial decomposition for high-resolution spectral fitting is that the truncation error is exactly orthogonal to the parameter space spanned by the Hermite polynomials included in the fit; the aliased $\hat{a}_j$ are expected to approximately retain this property. As a result, we expect the estimation of $\hat{a}_j$ to be robust to the truncation error for each individual line shape due to approximate independence from it (in the following, we will drop the hat notation and simply let $\hat{a}_j \equiv a_j$). Note, however, that the simultaneous analysis of multiple overlapping line shapes is affected by the inter-dependence of Hermite coefficients of different lines. Such dependence cannot be easily treated by an analytical expansion and therefore we make use of a numerical sampling scheme, described in following sections.

4.1.1 Bayesian Analysis

Let us define θ to be the set of parameters we wish to infer from the data, $\mathcal{D}$ the set of experimental data, and $\mathcal{M}_i$ a model that we wish to evaluate. An example of model is a collection of Hermite functions used to describe the line shapes of a fixed number of atomic lines. Bayes' formula then reads

$$p(\theta|\mathcal{D}, \mathcal{M}_i) = \frac{p(\mathcal{D}|\theta, \mathcal{M}_i)p(\theta|\mathcal{M}_i)}{\mathcal{Z}(\mathcal{D}|\mathcal{M}_i)}, \tag{4.11}$$

where

$$\mathcal{Z}(\mathcal{D}|\mathcal{M}_i) = \int p(\theta|\mathcal{M}_i)p(\mathcal{D}|\theta, \mathcal{M}_i)d\theta \tag{4.12}$$

is the *evidence* (or *marginal likelihood*) of model $\mathcal{M}_i$.

The term $p(\mathcal{D}|\theta, \mathcal{M}_i) \equiv \mathcal{L}(\mathcal{D}|\theta)$ is the likelihood distribution of observing the data given the model and parameters, which will be derived in this section. $p(\theta|\mathcal{M}_i) \equiv p(\theta)$ is the prior distribution, which incorporates prior knowledge and physical constraints to the model parameters. BSFC uses a uniform prior on Hermite coefficients subject to the constraint that the predicted line shapes are *unimodal.*

The term $p(\theta|\mathcal{D}, \mathcal{M}_i) \equiv p(\theta|\mathcal{D})$ is the posterior distribution, which can be used to either calculate maximum-a-posteriori (MAP) or average estimators for the model parameters. In the analysis described below, we report the mean and standard deviation of samples (accounting for their respective statistical weights, whenever these are computed by the adopted algorithm). This choice is a useful simplification since further analysis using spectral moments often assumes that uncertainties on experimental measurements are Gaussian. However, adoption of more robust statistics, such as median and inter-quantile ranges, may be easily accomplished in BSFC from samples.

The evidence $\mathcal{Z}$ acts as a normalization constant for equation (4.11), but it also plays the role of allowing the selection of the most appropriate model for a set of data [7], thus its name. $\mathcal{Z}$ is typically ignored, as it is not directly needed for parameter estimation. Moreover, the integration required to compute $\mathcal{Z}$ tends to be a computationally expensive task. However, computing the Bayesian evidence allows one to compare how much the data support one mathematical model versus another. For this reason, inference methods that can provide an accurate estimate of the evidence are advantageous.

Applying the Bayesian formulation to the moment estimation problem requires the calculation of the probability $P(\{\mathbf{M}_\ell\}|n)$ of observing the vector of moments $\mathbf{M}_\ell = (M_{\ell,0}, M_{\ell,1}, M_{\ell,2})$, one for each spectral line ℓ, given the observed spectral profile $n(\lambda)$.

For an observed spectral profile $n(\lambda)$ and a predicted spectral profile $f(\lambda;\theta)$ (where the prediction's dependency on the parameters θ is made explicit), we use the fact that photon rates are Poisson distributed and, for large counts, we can approximate their distribution as Gaussian. The distribution is thus taken to scale as $e^{-\frac{\chi^2}{2}}$, where

$$\chi^2 = \int_{-\infty}^{\infty} \frac{\left(f(\lambda;\theta) - n(\lambda)\right)^2}{f(\lambda;\theta)}\, d\lambda \tag{4.13}$$

Discretizing this integral into M bins allows us to calculate the log-likelihood function of observing the spectral profile as the log-likelihood of a multi-variate Gaussian,

$$\ln(P(n|\theta)) = -\sum_{j=1}^{M} \frac{\Delta\lambda_j}{2} \left[\ln(2\pi f(\lambda_j;\theta)) + \frac{(f(\lambda_j;\theta) - n(\lambda_j))^2}{f(\lambda_j;\theta)} \right] \tag{4.14}$$

Note that in practice the more accurate Simpson's rule is used to compute the integrals in BSFC.

Now to define the functions $f(\lambda;\theta)$, we choose the parameter set to be the set of center and scale parameters and the set of all Gauss-Hermite expansion coefficients for each line, as defined in the previous section.

$$\theta = \{\lambda_{c,\ell}, s_\ell, \{a_{\ell,i}\}\} \tag{4.15}$$

The predicted spectral profile can be written

$$f(\lambda;\theta) = \sum_{\ell} \sum_{i=0}^{\infty} a_{\ell,i} \phi_i \left(\frac{\lambda - \lambda_{c,\ell}}{s_\ell} \right) \tag{4.16}$$

Since the first three moments of each line depend only on the first three Hermite coefficients of that line, one has $P(\{\mathbf{M}_\ell\}|n) = P(\{\mathbf{a}_\ell\}|n)$, where $\mathbf{a}_\ell = (a_{\ell,0}, a_{\ell,1}, a_{\ell,2})$ is the vector of the first three Hermite coefficients corresponding to the three moments.

As derived in Section 4.1.2, the Hermite coefficients are weakly correlated for near-Gaussian lines. Thus, the high-order Hermite coefficients have a small influence on the statistical distribution of low-order Hermite coefficients. Therefore, each term of the series is independent of the truncation error, resulting in an efficient and robust truncation to only a few terms in the expansion. This truncation is expressed as:

$$f(\lambda;\theta) = \sum_{\ell} \sum_{i=1}^{N} a_{\ell,i} \phi_i \left(\frac{\lambda - \lambda_{c,\ell}}{s_\ell} \right). \tag{4.17}$$

We will show later that typically $N = 3$ is sufficient, but higher-order Hermite coefficients can be easily added when necessary.

Additional constraints can be put onto the parameters. One assumption that we adopt (but may be avoided, if desired) is that all the ion lines are emitted from species with approximately the same temperature and velocity. This constraint is enforced by having only one scale (s) and one center parameter λ_c. For each line, $s_\ell = s\sqrt{m_\ell/m_0}$ and $\lambda_{c,\ell} = \lambda_c + \delta\lambda_{0,\ell}$, where $\delta\lambda_{0,\ell}$ is the separation between line rest wavelengths and m_l/m_0 is the ratio of masses between the emitting ion and a reference value.

Therefore, for a spectrum including 3 spectral line-shapes, one may estimate a scalar noise (+1 parameter), a scale and central wavelength (+2) and three Hermite polynomials for each line ($3 \times 3 = 9$), for a total of 12 free parameters. Varying the number of Hermite polynomials used or the number of fitted lines may raise the dimensionality further, increasing the computational cost of parameter estimation.

Each spectrum corresponding to a time window in a spatial channel of the spectrometer was fitted independently of the rest. It is possible to introduce covariances between the likelihood calculations of different spatial channels and time bins to represent the effect of correlated errors in the instrument or spatial correlation between the different channels, but this was not pursued further in this work.

Prior Distributions

In order to ensure that the line shapes modelled by the Hermite coefficients represent physically realizable spectral line shapes, constraints need to be placed on their values. In a Bayesian context, physical constraints are often placed via the choice of a prior distribution on parameters. For example, the emissivity cannot be negative, so the prior distribution on a_0 can only be nonzero for $a_0 \geq 0$. On grounds of "complete ignorance" about the parameters to be inferred, one may assign uniform priors over the entire physically-realizable range for each parameter; however, often one has more information available and this should be used to avoid results that are not believed to be acceptable. This can be done by choosing more complicated prior distributions and by restricting the available range of allowed values for each parameter.

A central role in BSFC is played by the estimation of the 0th order Hermite polynomial coefficient, $\hat{a}_0$, which closely corresponds to the intensity of an individual line shape. For the primary line shape of interest, most fitting attempts will easily identify the approximate magnitude of $\hat{a}_0$. However, in cases where a line shape is barely visible (often for nearby satellite lines) it may not be simple to determine whether the satellite line intensity is small or there is simply no evidence for the line being observed. In other words, we do not know *a priori* what is the order of magnitude of $\hat{a}_0$. This statement is equivalent to agnosticism regarding the *scale* of this parameter. In such cases, the use of a logarithmic prior (commonly referred to as log-uniform or Jeffreys prior; see [65] for an extensive discussion) offers an effective non-informative choice that does not discriminate between different scales. Use of this prior on $\hat{a}_0$ has been tested in BSFC and found to be preferable to a uniform prior over the positive real axis for cases where line shapes are barely visible in the spectrum. However, in practice this choice of prior does not significantly affect BSFC's estimates for physical parameters over the more basic uniform prior over positive real numbers.

In BSFC, we also find it convenient to impose a constraint of *unimodality* on the line shape. This is expected to hold in tokamak plasmas, where emissivity, velocity, and temperature profiles generally vary smoothly and do not have multiple peaks. The unimodal constraint also forces the lines to be non-negative. This is because the line shapes decay as $\lambda \to \pm\infty$, so any zero crossing must necessarily result in at least two local extrema. The constraint of unimodality can be imposed by considering the zeros of the *first derivative* of the line shape function, given for an index ℓ by

$$f_\ell(\lambda) \approx f_\ell(\lambda;\theta) = \sum_{i=1}^{N} \hat{a}_{\ell,i}\phi_i\left(\frac{\lambda-\lambda_{c,\ell}}{s_\ell}\right) \tag{4.18}$$

Note the recurrence relation

$$\frac{d}{dx}\left[He_n(x)e^{-x^2/2}\right] = -He_{n+1}(x)e^{-x^2/2}. \tag{4.19}$$

Since $e^{-x^2/2} > 0$, finding the zeroes of the first derivative of (4.18) only requires consideration of the roots of Hermite polynomials with indices shifted up by one. Moreover, we note that one can scale all of the coefficients simultaneously by a constant factor and not change the resulting roots, so it suffices to consider the case of

$a_{\ell,0} = 1$, then scale the obtained constraint accordingly. To impose a constraint of unimodality of the total line shape, we therefore require that the derivative of Eq. 4.18 must have only one real root near the origin, and all other roots must either be complex or far from the origin.

The values chosen for BSFC require that the real root be within the interval $x \in (-0.2, 0.2)$ (which corresponds to the spectral peak occurring within 0.2 times the thermal velocity of the average shift of all of the lines). All other roots must be either complex or outside the interval $(-\sqrt{1.25N} - 1, \sqrt{1.25N} + 1)$, where N is the number of Hermite coefficients. This ensures that the line does not have multiple peaks, except far away from the origin, where the brightness is negligible and the peak cannot be observed. This scaling with N was chosen since the higher-order Hermite functions make contributions further from the origin at increasingly large n, scaling approximately with $\sqrt{n}$.

It is convenient for the constraint to be expressed as a series of linear inequalities. This makes it more tractable for non-linear fitting routines, and also makes it possible to embed it into the unit hypercube required for the `MultiNest` algorithm. This is done by using MCMC to sample the admissible values for the Hermite coefficients, then fitting the resulting region with linear constraints. This is done once for the case $a_{\ell,0} = 1$, then scaled accordingly. For simplicity only two linear constraints are used per Hermite coefficient. The constraints are placed in such a way that they form a collection of simplices sharing the origin as a vertex. Standard methods for sampling a simplex from a uniform hypercube are then used to express the constraints in a way amenable for use with the `MultiNest` algorithm [27].

4.1.2 Weak Correlation of Hermite Coefficients

In this section, we motivate the application of the chosen Hermite polynomial decomposition for line spectra and provide multiple lines of reasoning to explain the observed weak correlation between Hermite coefficients.

To provide a geometrical intuition for why the truncation to few polynomial terms is so effective in BSFC. Consider the decomposition of a single line shape

$$f(\lambda) = \sum_{j=1}^{\infty} a_j He_j(\lambda) \approx \hat{f}(\lambda) \equiv \sum_{j=1}^{N} \hat{a}_j He_j(\lambda) \tag{4.20}$$

and for simplicity let us ignore the effect of aliasing (see equation (4.10)). Since Hermite polynomials constitute a complete basis, an infinite series of polynomial terms would perfectly capture the functional form of $f(\lambda)$. In a truncation to N terms, $\hat{f}(\lambda)$, we define the vector $\vec{a} = \{a_1, a_2, \dots, a_N, 0, 0, \dots\}$, where elements beyond the truncation limit have been set to 0. The error incurred in the truncation can be defined as $\vec{\epsilon} \equiv \vec{a} - \vec{\hat{a}}$. By the orthogonality of Hermite polynomials, $\vec{\epsilon}$ must be orthogonal to $\vec{\hat{a}}$, and more generally to $span(\{He_j\}_{j=0}^{N})$. Consequently, we have

$$\langle f(\lambda) - \sum_{j=1}^{N} a_j He_j(\lambda), He_j \rangle = 0, \quad j = 0, \dots, N \tag{4.21}$$

which is a direct result of the coefficients being given exactly by the projection

$$a_j = \frac{\langle f, He_j \rangle}{\langle He_j, He_j \rangle} = \frac{\langle f, He_j \rangle}{j!}. \tag{4.22}$$

This shows that a decomposition using a complete orthogonal polynomial basis offers the advantage that the polynomial coefficients retained within the truncation are independent of the truncation error. In other words, higher-order coefficients, even accounting for aliasing, are expected to have small influence on lower-order ones. The choice of Hermite polynomials over other orthogonal polynomial families (see, e.g. Ref. [8]) for BSFC is motivated by the near-Gaussian shape of the spectral lines.

Further intuition into the process of estimating Hermite coefficients can be obtained through the following argument. Consider the case of one isolated spectral line with negligible background noise. Suppressing the line index ℓ, and writing

$f = h(x;\theta)e^{-x^2/2}$ and $n = g(x)e^{-x^2/2}$,

$$\begin{aligned} \chi^2 &= \int_{-\infty}^{\infty} dx \ \frac{(h(x;\theta) - g(x))^2 e^{-x^2}}{h(x;\theta)e^{-x^2/2}} \\ &= \int_{-\infty}^{\infty} dx \ e^{-x^2/2} \frac{(h(x;\theta) - g(x))^2}{h(x;\theta)} \end{aligned} \tag{4.23}$$

Now, we use the *near-Gaussian line approximation* $h(x;\theta) \approx a_0$ in the denominator of the expression to write χ^2 as a quadratic form using the inner product defined earlier

$$\begin{aligned} \chi^2 &\approx \frac{1}{a_0} \int_{-\infty}^{\infty} dx \ e^{-x^2/2} (h(x;\theta) - g(x))^2 \\ &= \frac{1}{a_0} \langle h - g, h - g \rangle \end{aligned} \tag{4.24}$$

The inner product here suggests the use of Probabilist's Hermite polynomials, rather than Physicist's Hermite polynomials. To demonstrate how this orthogonality helps in the statistical estimation of the coefficients a_j, let us re-write Bayes' Theorem here for convenience:

$$P(h|g) \propto P(g|h)P(h) \tag{4.25}$$

Representing h by its Hermite coefficients $\{a_j\}$ and using an improper uniform prior $P(\{a_j\}) = 1$ on the Hermite coefficients gives, for the log-likelihood

$$\ln P(\{a_j\}|g) = \ln P(g|\{a_j\}) - C \tag{4.26}$$

where C is a normalization constant that does not depend on $\{a_j\}$. Under the assumption of Gaussian statistics for the observed photon counts, the likelihood is proportional to the exponential of the negative χ^2, so one can write

$$\ln P(\{a_j\}|g) = -\chi^2/2 - C' \tag{4.27}$$

Given that the log-likelihood function is of the quadratic form in equation (4.24), this means that $P(\{a_j\}|g)$ behaves as a multivariate Gaussian in variables $\{a_j\}$, with mean given by the Hermite coefficients $\{g_j\}$ of the function g, and covariance given by the matrix elements of the quadratic form. Since the Hermite polynomials are orthogonal on this inner product, the quadratic form and hence the covariance matrix is diagonal. Thus, given an uninformative prior, the Hermite coefficients behave approximately as *uncorrelated Gaussian random variables.* This means that the distribution of higher-order Hermite coefficients should have a small statistical effect on the lower-order Hermite coefficients, as also seen by the geometric argument presented above. This explains the demonstrated accuracy of the Hermite function expansion to a finite, small number of Hermite functions.

Note that the argument of near-independence of Hermite polynomial coefficients described above only applies for a single, isolated line shape. However, for the case of overlapping line shapes with background noise one should expect some form of dependence between coefficients describing one line shape and coefficients describing other overlapping ones. For example, the value of a_0, corresponding to the intensity of a certain line shape, will inevitably affect the estimation of coefficients for overlapping lines. In BSFC, the use of nested sampling via `MultiNest` with the full (rather than approximate) log-likelihood function enables us to appreciate the correlations existing between parameters within high-dimensional parameter space. Therefore, while the discussion above explains why a Hermite polynomial decomposition offers a convenient form for rapid truncation and weak dependence between coefficients, we rely on a full numerical reconstruction of the posterior parameter space to deal with correlations that may arise in the presence of overlapping line shapes. This makes the BSFC approach fast (thanks to rapid truncation), accurate (thanks to near-independence of coefficients for each individual line shape) and effective in recognizing difficult spectral superpositions from different atomic lines.

4.2 Application to Spectral Data

4.2.1 General Fit Properties

This section will demonstrate some of the properties of the BSFC fitting routines on examples for experimentally observed He-like spectra of calcium and argon, centered on the $n = 2$ w resonance line; the reader is referred to [101] for details on these spectra. A typical calcium He-like spectrum with non-negligible satellite lines, and an inferred fit, is shown in Figure 4-1. The brightest line visible is the He-like w resonance line, and the other two visible lines are unresolved dielectronic $n = 4$ and $n = 3$ satellite groups. The fit shown was computed with 3 Hermite coefficients.

For argon He-like spectra, Figure 4-2 shows that inferred measurements from BSFC are relatively insensitive to the number of Hermite coefficients used in the fit (on the axis of abscissae). Additionally, the log-evidence (labelled as $ln\mathcal{Z}$, on the bottom panel) predicts that a simpler fit provides the best estimate of the inferred measurements: this conclusion follows from the observed reduction of $\mathcal{Z}$ with number of Hermite coefficients, which may be interpreted as indicating overfitting when the model is excessively complex for the provided data [7]. This observation will be described in more detail in the next section, with demonstrations based on synthetic data.

MCMC methods also allow for the results of the fit to be visualized through 'corner' plots. These are helpful in understanding the impact of specific parameters on the result, providing qualitative and quantitative insight that may be difficult to attain with nonlinear optimizers. For example, a corner plot for the 3 hermite function fit from Figure 4-2 is shown in Figure 4-3. This illustrates the effect of an unresolved satellite line on the measurements inferred from the primary w line in a combined fit due to correlations in the hermite coefficients introduced by the line overlap. In the illustrated example, the joint distribution plot of satellite line brightness versus velocity shows that increasing the inferred satellite line brightness tends to decrease the inferred velocity. However, within the inferred range of satellite line brightnesses, the overall decrease in velocity is less than 0.5 km/s. Thus this parameter is clearly

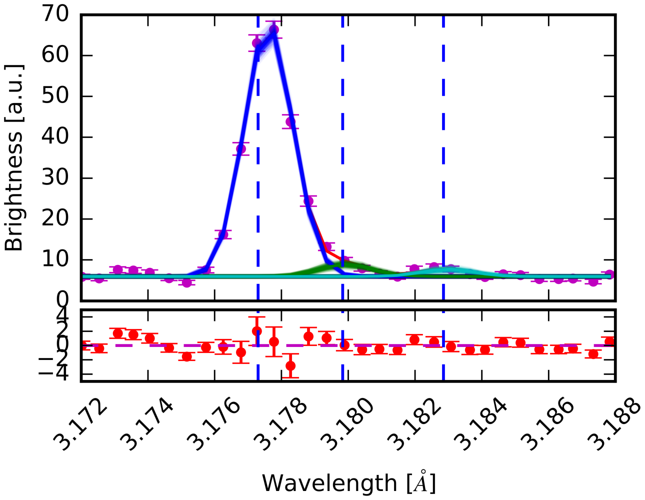

Figure 4-1: An example of a Ca^{18+} spectral fit from BSFC with 3 Hermite coefficients. Observed data are shown by the scatter points in magenta. There are three tracked spectral lines at the locations marked with vertical dashed lines. The maximum likelihood estimate fit is shown as a single curve in red. The residuals from this fit are shown on the bottom panel. The uncertainty in the fit is shown by overlapping multiple attempted fits with continuous lines, so the blurring of the lines is indicative of the error bars. The inferred contributions from individual lines are displayed in different colors.

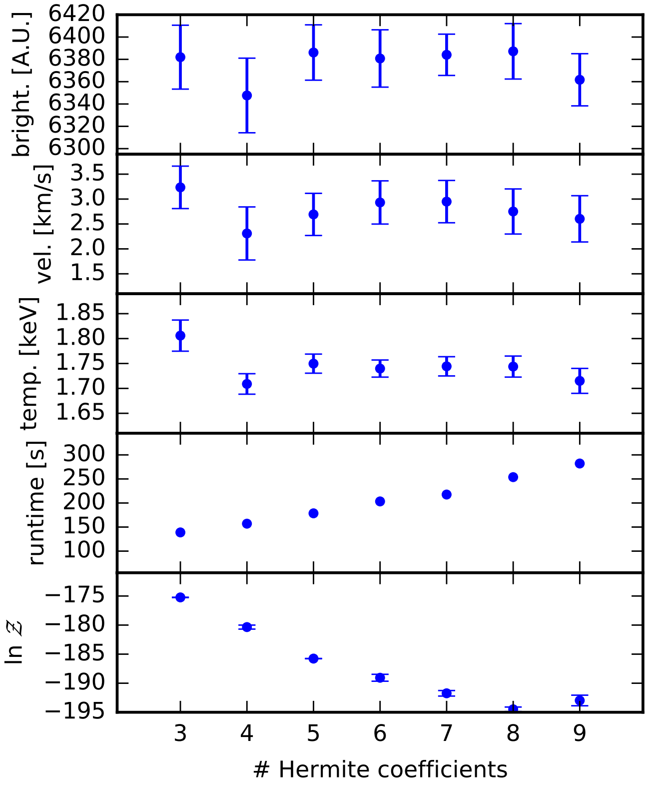

Figure 4-2: Results of a scan of number of Hermite coefficients used to fit the primary line for the argon He-like w resonance line. The inferred line-integrated measurements are shown in the top three panels, the computation time to perform the inference using Nested Sampling on a single Intel Core(TM) i7-7700 CPU (3.60 GHz) is in the second to last plot, and the log-evidence is in the bottom panel. The inferred measurements remain very close within error bars despite increasing the number of Hermite coefficients. The log-evidence decreases as the number of Hermite coefficients increases, demonstrating that the 3 Hermite coefficient model is the most robust and will provide the most valuable inference.

not the dominant source of uncertainty in the velocity measurement. We remark that these correlations are difficult to quantify in traditional nonlinear fitting techniques, but are a direct output of the numerical sampling technique in BSFC.

4.2.2 Synthetic Data Analysis

To validate the results of the fitting code, synthetic tests were performed. To generate experimentally-relevant spectral line shapes, synthetic emission was line-integrated using impurity emissivity, velocity, and temperature profiles inferred using standard tomographic methods. The true moments were calculated exactly using line-integration of the synthetic data. Two cases are presented here: one from an L-mode tokamak plasma in Figure 4-4, and one from an I-mode with a hollow emissivity profile in Figure 4-5.

These fits were done on the He-like argon $n = 2$ resonance w line with 3 Hermite coefficients. In both cases, the unresolved dielectronic $n = 4$ satellite lines in our atomic database were removed from the fit, since the Bayesian evidence obtained for a fit without it was found to be higher than with it. This assessment provides a rigorous way of determining whether the data justify a certain level of complexity in a fitting model. As seen from these plots, the method infers the true moments very well. Moreover, the uncertainty in the inference clearly matches the spread of the data. The non-Gaussian shape of the line resulting from higher-order Hermite coefficients typically accounted for a correction of approximately 10% to the temperature, and 20% to the velocity.

4.2.3 Application to Alcator C-Mod XICS

Results from BSFC were also compared to results inferred from THACO [97], the standard code used to analyze XICS data in Alcator C-Mod. THACO estimates line moments by using a nonlinear χ^2 minimization to remove satellite lines, followed by a direct calculation of line moments by integration. We remark that this method is typically only applied on non-overlapping spectral lines to avoid complications that

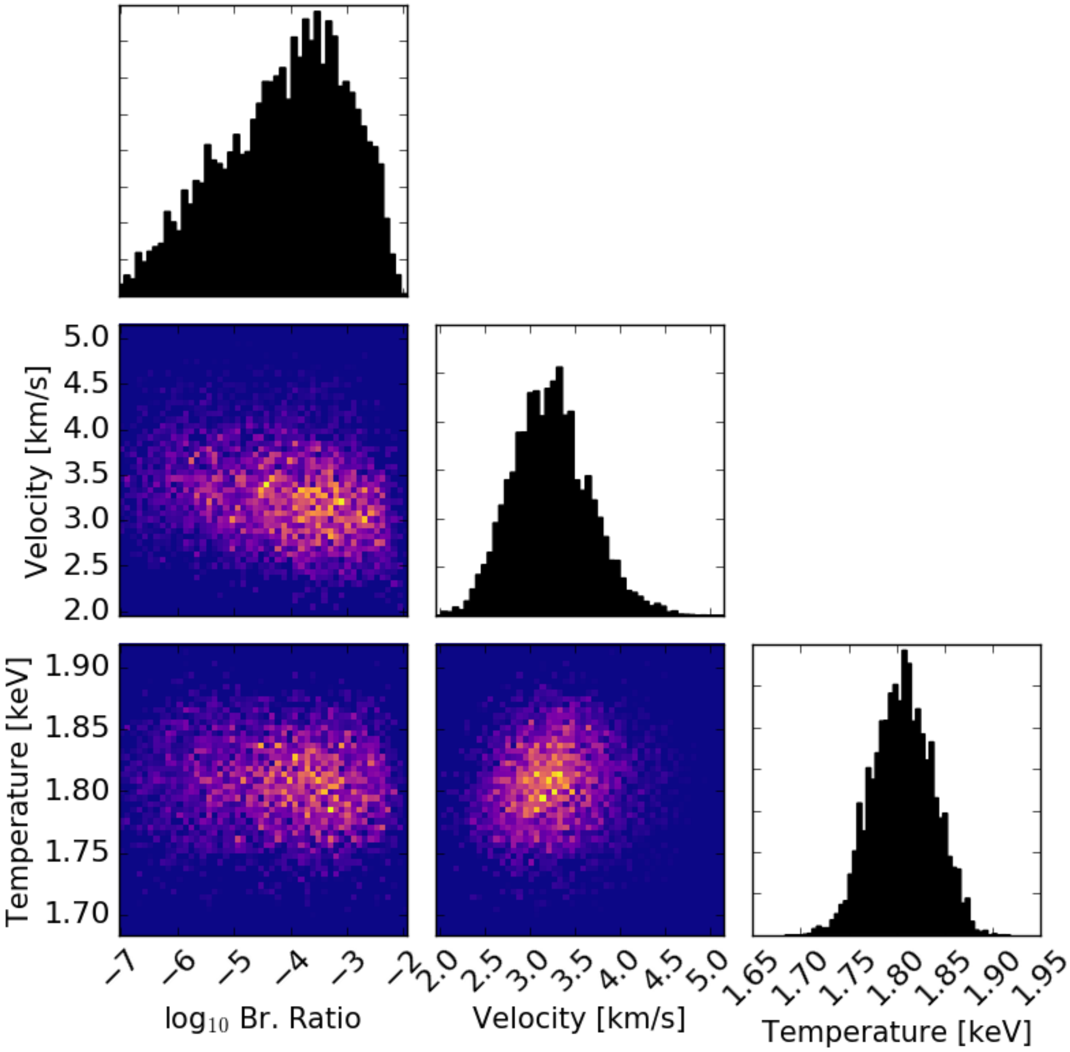

Figure 4-3: Corner plot showing correlation between the measurement of the brightness of an unresolved satellite line and its effect on other measurements. The plots on the diagonals are histograms showing the marginal distributions of the posterior inferred values of satellite to primary line brightness ratio, and the primary line velocity and temperature. The plots on the off-diagonals show the pairwise joint distributions.

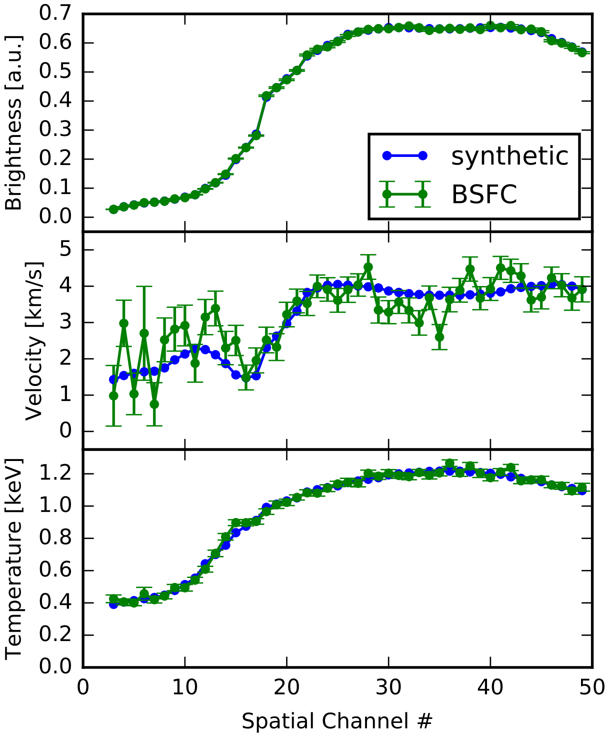

Figure 4-4: Comparison between true synthetic line-integrated measurements (blue) and measurements inferred from BSFC (green) for an L-mode plasma.

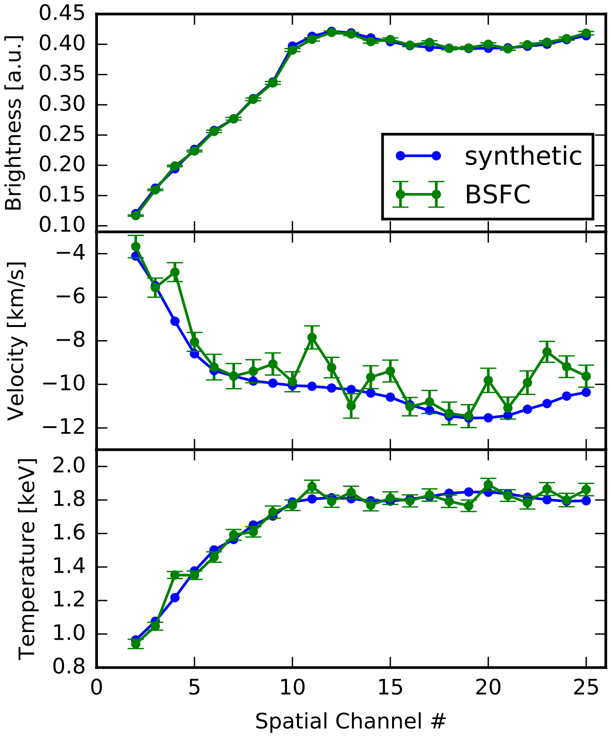

Figure 4-5: Comparison between true synthetic line-integrated measurements (blue) and measurements inferred from BSFC (green) for an I-mode plasma with hollow emissivity profile.

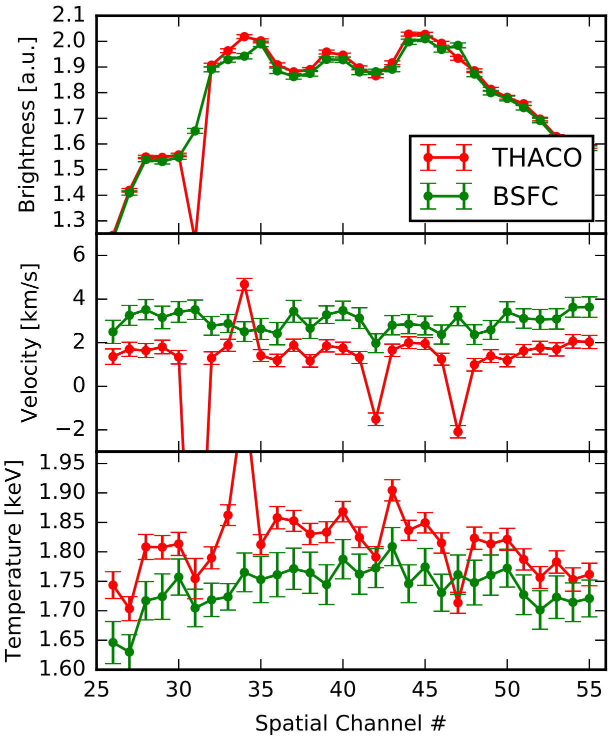

Figure 4-6: Comparison between line-integrated measurements inferred from BSFC (green) and from THACO (red) for an L-mode plasma zoomed in to a subset of spatial channels. Note that the BSFC inferences have fewer outliers, and are generally more consistent. The inferred error bars are also larger, more accurately capturing the true uncertainty in the inferences.

are directly addressed by BSFC. To illustrate the advantages of BSFC in these cases, we compare its results to those of THACO in two cases with overlapping lines: in the first case, one has a steady-state argon He-like w resonance line spectrum as seen in Figure 4-6; in the second, we have a rapidly-evolving calcium He-like w resonance line spectrum from a laser-blow-off impurity injection Figure 4-7.

In both cases, we see that traditional Gaussian line fitting methods can produce outliers. The BSFC method provides more consistent results, and the error bars also more realistically reflect the spread of data. Moreover, we note that BSFC finds a systematic shift of velocity and temperature measurements compared to the THACO inference. The former inference was validated against synthetic spectra with unresolved lines, and thus shown to be more accurate.

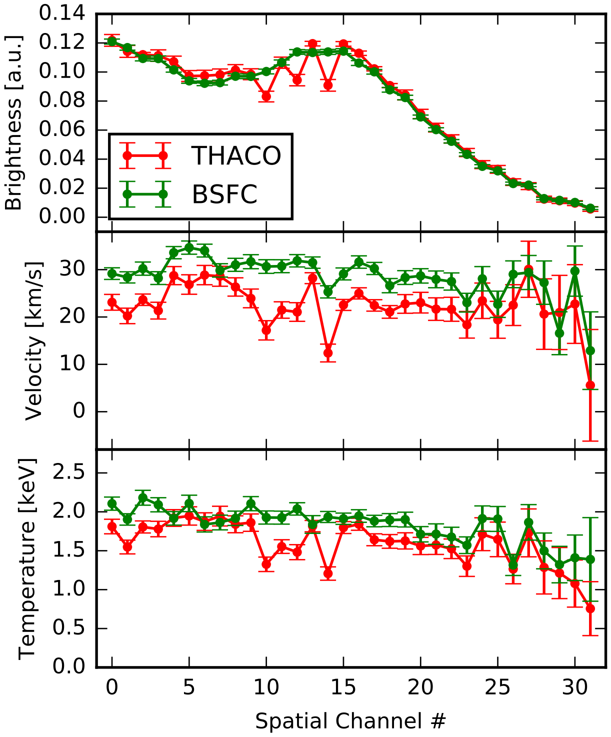

Figure 4-7: Comparison between line-integrated measurements inferred from BSFC (green) and from THACO (red) for an impurity injection in an I-mode plasma.

Chapter 5

Characterization of Turbulent Bifurcation via Hysteresis Experiments

In this chapter, a set of experiments is presented that uses hysteresis as a novel probe of the LOC/SOC transition and intrinsic rotation reversal [17]. Hysteresis in rotation of L-mode plasmas has been observed on several different tokamaks [9, 99]. The experiments presented here show that nearly exact matches of mean density and temperature profiles can lead to different rotation and turbulent states in the same discharge. The analysis builds on careful quantification of uncertainties using Gaussian Process Regression (GPR) described in Appendix B and on ion temperature and velocity measurements using the Bayesian Spectral Fitting Code (BSFC) described in Chapter 4. This shows that directly measured profile effects or other parametric dependencies of the turbulent response are not responsible for the transition itself, and instead must be the result of a nonlinear bifurcation in the turbulent state.

5.1 Experimental Setup

Two methods were used to realize the rotation reversal hysteresis: density control for Ohmic plasmas, and ion cyclotron resonance frequency (ICRF) heating power modulation for auxiliary heated plasmas. The discharges were upper single null, with $B_t = 5.4$T. The three experimental cases performed are shown in Table 5.1.

Table 5.1: Experimental cases performed

Case	I_p	Density Modulation	ICRF Modulation
I	0.8 MA	±10%	Off
II	1.1 MA	±10%	Off
III	0.8 MA	constant	0.2-1.2 MW

For all plasmas, line-average density control was achieved using edge fueling and a cryopump, along with the C-Mod two-color interferometer system for feedback control. For the Ohmic plasmas (Cases I and II), the density modulations were triangle waves with amplitude ±10% of a central value, and period much longer than the energy confinement time, $600\text{ms} \gg \tau_e \approx 25\text{ms}$. Note that the impurity confinement time is of similar magnitude [103], $\tau_I \sim \tau_e$. For the auxiliary heated plasma (Case III), the ICRF heating modulation was also a triangle wave with the same period from 0.2 to 1.2 MW, with the intention of controlling the collisionality through changes in the electron temperature. For comparison, the Ohmic power was estimated to be 0.95 MW for a plasma at the same current in case I. Rotation profiles during the reversal evolved on timescales $\approx 4\tau_e$, slower than the modulation period. There was no beam injection in these plasmas, so the only particle source is at the edge. Additionally, on some discharges a perturbed laser blow-off injection of CaF_2 impurity was performed to assess the robustness of the hysteresis to perturbation. Time traces from a representative Case I discharge are shown in Figure 5-1, where time points with matching line-integrated densities, but differing toroidal rotation, have been marked.

5.2 Comparison of Kinetic Profiles Across Reversal

The coexistence of multiple rotation states at a given density can be visualized by plotting the line-average density versus the line-average toroidal velocity of the discharge as a hysteresis curve, as is done in Figure 5-2. The plotted trajectories overlay closely,

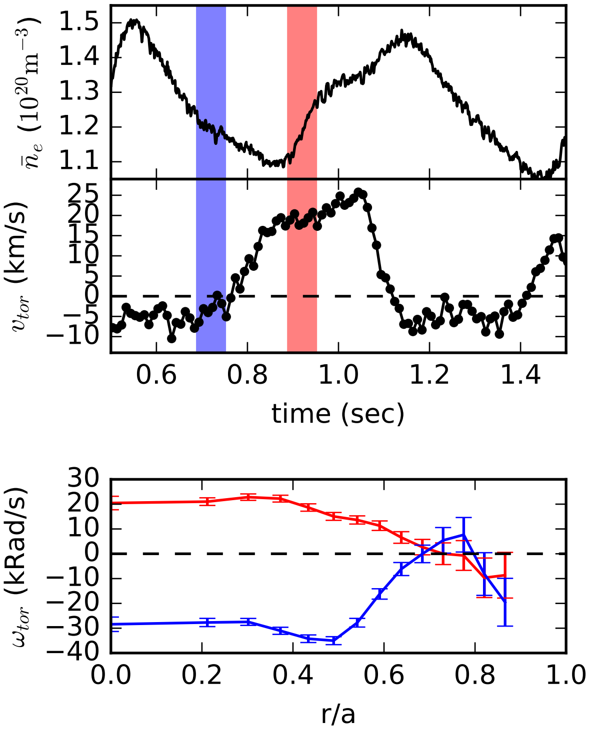

Figure 5-1: Time trace of a 1.1 MA Ohmic discharge from the hysteresis experiments (top) and representative toroidal rotation profiles from another discharge at the same current (bottom). The two times marked by the blue and red bars have nearly the same line-average density, electron and ion temperatures, but different core toroidal velocities. The rotation profiles are similar at the edge but diverge in the core. The region where the rotation diverges and the shear is non-zero will be referred to as the rotation reversal region.

showing the robustness of the hysteresis phenomenon to noise and perturbation from LBO. Since the edge rotation is similar for the two rotation states, the change in the core rotation profiles indicates a change in the turbulently generated residual stress in the core, implying that some aspect of the turbulence, yet to be determined, changes between the two states. This shows there exist two distinct states of turbulence, one exhibiting co-current rotation and the other counter-current rotation, which can stably exist in this range of plasma density. As the density is slowly changed, the co-current rotation states continuously evolve to lower-collisionality states, which corresponds to the 'LOC-like' branch, while the counter-current states continuously evolve to higher-collisionality states, which correspond to the 'SOC-like' branch. The rotation states between the two branches are transient, and do not correspond to steady states of the plasma. The transition densitites were found to match those from density ramp experiments, independent of ramp rate. Thus, it makes sense to associate plasmas which exhibit co-current rotation with 'LOC-like' turbulence, and plasmas which exhibit counter-current rotation with 'SOC-like' turbulence. In addition, a hysteresis cycle in core electron temperature versus core line-average toroidal velocity is also plotted for Case III, which demonstrates that the hysteresis in toroidal rotation persists for auxiliary heated L-mode plasmas, where the hysteresis is effected by ICRF heating modulation rather than by density modulation. While the general trend with the collisionality ν_* is consistent, the exact transition value is not the same between the ICRF heated case and the Ohmic cases.

Kinetic profiles matched across the reversal for all three cases are shown in Figure 5-3. Electron density was measured with the core and edge Thomson scattering system, while electron temperature was measured with both the Thomson scattering system and the GPC-ECE system. Due to a diagnostic issue, local profiles of ion temperature and rotation were unavailable for these shots, so line-integrated data inferred using Bayesian techniques [19] are shown instead. Additionally, local ion profiles from previously published discharges in *Rice et al.*[103], whose experimental parameters were replicated in this set of experiments, are shown when available. The fits displayed use data time-averaged over 60 ms, and utilize Gaussian Process

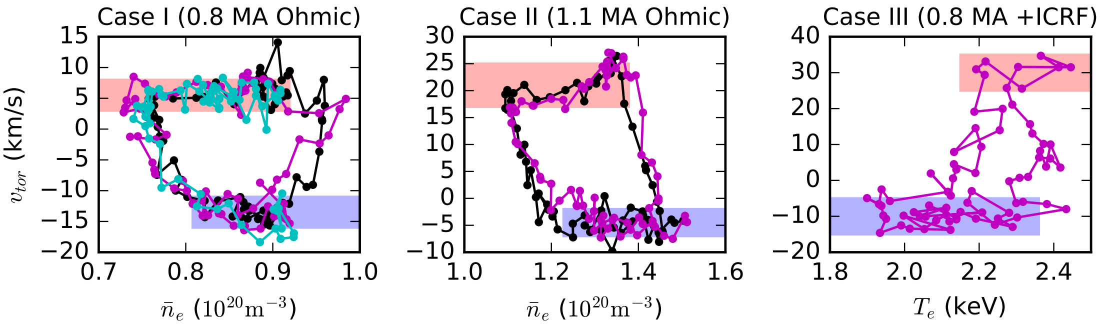

Figure 5-2: Trajectories of several discharges as hysteresis plots for the different experimental cases. The different colors in each plot correspond to different discharges. The discharges all demonstrate clearly separated rotation states at the same density for the ohmic cases, and core electron temperature for the ICRF heated case. These states have been highlighted in red and blue. Note that discharges in cyan and magenta were perturbed using laser blow-off injections. The discharge in the left frame plotted in cyan does not reach the required density to transition from the LOC-like branch to the SOC-like branch, so it does not complete a full hysteresis loop.

Regression to provide rigorous estimates of the error bars on the profiles and their gradients [21]. These error estimates take into account the statistical and systematic uncertainties of the data, given by error bars on individual measurements, as well as systematic uncertainties due to the unknown form of the fit, provided by a prior on the hyperparameters of the fit. The latter can have a large effect on the error bars, so their effect is properly taken into account by sampling the hyperparameter space using Markov Chain Monte Carlo. As in *Chilenski et al.*[21], a non-stationary squared exponential kernel with tanh length scale shape is used. Note the priors differ from those used for the previously reported profiles, as they were changed to better capture the flattening effect of sawteeth inside the sawtooth mixing radius. For all three cases, the profiles and gradients responsible for determining the linear stability characteristics of the drift-wave turbulence overlay each other very closely. This confirms previous analysis that drift-wave stability is not responsible for the reversal.

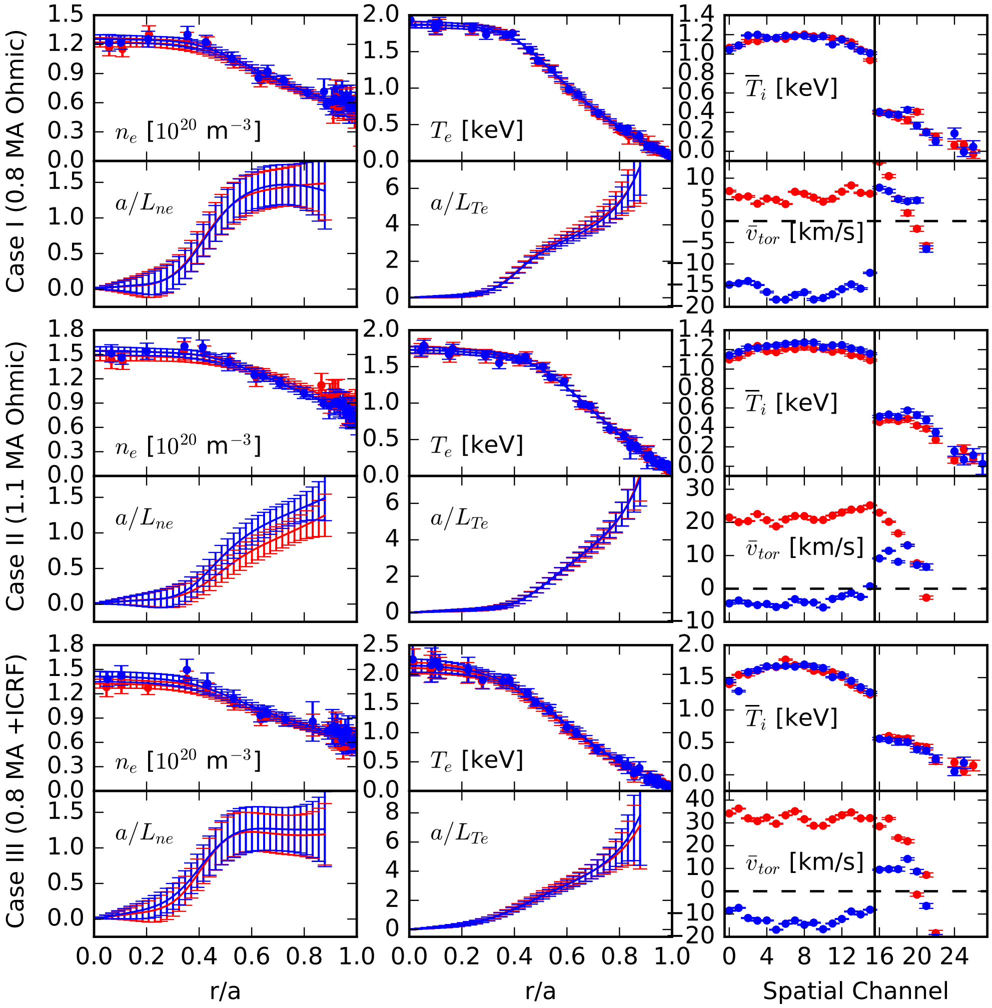

Figure 5-3: Profiles and gradients of electron density (left column), temperature (center column), and line-integrated ion temperature and rotation (right column), for the three experimental cases. The co-current rotation LOC-like profiles are shown in red, and the counter-current rotation SOC-like profiles are shown in blue. For the electron profiles, the raw data are shown by the scatter points, and the GPR fit is shown as a smooth profile. The timelices were chosen to show profiles which overlay each other well within experimental uncertainty. For the ion measurements, different spatial channels provide coverage of different radial locations in the plasma. There is a gap in spatial coverage of the plasma at channel 16, which is demarcated by a solid black line, which prevents the tomographic inversion of the ion profiles.

5.3 Fluctuation Measurements Across Reversal

Despite the nearly identical kinetic profiles, differences in fluctuations can be observed in all of the experimental cases. While a detailed picture of how changes in these measurements relate to the dynamics of the underlying turbulence is inaccessible without detailed synthetic diagnostic modeling, some broad interpretations are accessible. This section will discuss measurements from the phase contrast imaging, reflectometry, and correlation electron cyclotron emission diagnostics on Alcator C-Mod.

5.3.1 Phase Contrast Imaging (PCI) Measurements

Data are presented here from the Phase Contrast Imaging system on C-Mod, which is sensitive to line-integrated density fluctuations with wavevector component in the major radial direction of $k_R < 30\text{cm}^{-1}$, corresponding to $k_R\rho_s \lesssim 2.5$. In these cases, the PCI picks up high-frequency "wing" features in the LOC case, as has been previously reported[99, 102, 100, 98]. It has been shown that the presence of these wings does not correlate with a transition in dominant ion-scale linear instability from TEM to ITG [125]. These experiments go further and show that measured fluctuation spectra can change even with matched plasma density and temperature profiles, shown by the PCI spectra in Figure 5-4. One of the characteristic features observed about these PCI wings is an asymmetry in the $\pm k_R$ spectrum. The time evolution of a metric capturing this asymmetry is also plotted in Figure 5-4. It is interesting to observe that for the 1.1 MA Ohmic case, there is an asymmetry in the time evolution of fluctuations for the forward and reverse transitions. Going from LOC to SOC, when the shear layer forms, the fluctuations evolve on a timescale faster than the rotation reversal. Conversely going from SOC to LOC, when the shear layer collapses, the fluctuations evolve on a timescale similar to the rotation reversal.

Since PCI measurements are line-integrated, interpreting changes in PCI spectra can be challenging. The PCI sight lines are vertical, and intersect magnetic flux surfaces twice, once towards the top of the tokamak and once towards the bottom.

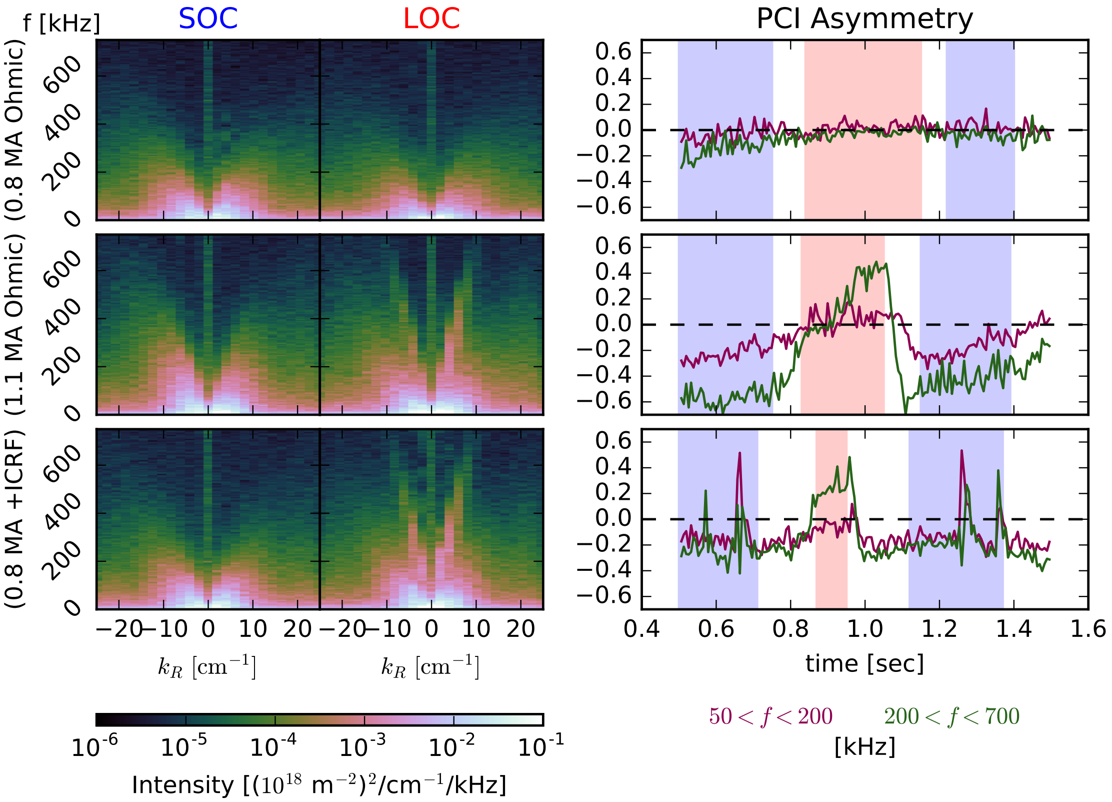

Figure 5-4: Spectrograms $S(k_R, f)$ of PCI fluctuations for the three experimental cases corresponding to the profiles in Figure 5-3 (left), and asymmetry $\frac{P_+ - P_-}{(P_+ + P_-)/2}$ for certain frequency bands plotted against time (right). While there is no discernible difference between the PCI spectra in the 0.8 MA Ohmic case, there are clear visible 'wing' features in the 200-700 kHz range for the other two cases. The evolution of these features in time is visualized by the asymmetry in the $\pm k_R$ parts of the spectrum at the given frequency bands. Times corresponding to steady co- or counter-current rotation are shaded in red and blue respectively.

The sign of the projection of k_θ on to k_R changes between these two intersections, so a $\pm k_R$ asymmetry is usually interpreted as an up-down fluctuation asymmetry. Note that k_R could be either larger or smaller than k_θ, depending on the angle of incidence to the flux surface and the radial wavevector k_r. Although it is difficult to precisely localize the radial location of the measured fluctuations, previous work suggests that the wing features are not an edge fluctuation[99]. Furthermore, it was shown via a PCI masking technique[95] that the features propagate in the ion diamagnetic direction in the laboratory frame. This is consistent with the expectation that in LOC, the Doppler shift dominates the plasma frame frequency of the drift-wave modes, and that the co-current rotation is in the ion diamagnetic direction in the low-field side where the drift-wave fluctuations originate. The roughly 700 kHz real frequency extent of the wings in the 1.1 MA Ohmic case corresponds to an angular frequency in the laboratory frame of $4.4c_s/a$ at $r/a = 0.6$. If this frequency were the result of a $E \times B$ Doppler shifted mode with zero real frequency in the plasma frame at $r/a = 0.6$, it would require the mode to have a toroidal mode number $n \approx 440$, although this estimate is crude due to uncertainty in the magnitude of the toroidal rotation and the radial location of the mode. Using $k_\theta \approx nq/r$, this would correspond to $k_\theta \rho_s \approx 3.7$. It would be difficult to observe ITG in the frequency range of the wings, which typically has $|\omega_r| \lesssim c_s/a$ and $k_y\rho_s \lesssim 1$. In contrast, TEMs with $k_\perp \rho_s \gtrsim 1$ and $|\omega_r| \gtrsim c_s/a$ may more plausibly be observed in the wing frequency range. Additionally, the weakly dispersive nature of the wings (i.e. fluctuations having nearly constant phase velocity) is consistent with intermediate scale $k_\theta \rho_s \approx$ 2-5 TEMs, as will be discussed in detail later. Note that the frequency response of the PCI detectors decays exponentially with frequency[39], so the attenuation of the wings at high frequency does not necessarily represent the attenuation of fluctuations in the plasma at that frequency.

One possibility for the lack of visible wings in the 0.8 MA Ohmic LOC case is the weaker Doppler shift (roughly 2-4 times smaller) in that case compared to either the 1.1 MA Ohmic case or 0.8 MA ICRF heated case, which may be insufficient to bring the wings above the strong fluctuations below 200 kHz. The wings not being discernible from the low frequency fluctuations, in combination with a possible difference in the ratio of edge to core fluctuation levels, may explain why the asymmetry is much weaker or does not appear in the 0.8 MA Ohmic case. Note that the gyro-Bohm normalized anomalous fluxes are larger in the 1.1 MA Ohmic case than they are in the 0.8 MA Ohmic case.

5.3.2 Reflectometry Measurements

The data presented here are from the 88.5 GHz channel of the Alcator C-Mod O-Mode baseband reflectometry system [112]. These measurements are sensitive to density fluctuations of $k_\perp$ up to 10 cm^{-1} [82], radially localized near the O-mode cutoff location on the outer midplane of the tokamak. This corresponds primarily to ion-scale fluctuations $k_\perp \rho_s \lesssim 0.8$, although the response of the signal over this wavenumber range is not flat, with significantly weaker sensitivity at large $k_\perp$. Both the in-phase and quadrature components of the reflectometry signal were used, providing both amplitude and phase information on the returned signal. Autopower spectra of the complex signal for reflectometry channels which were localized to the rotation reversal region are shown in Figure 5-5. In a 1D analysis the density fluctuation information is primarily carried by the phase shift of the returned signal. However, 2D effects such as scattering, diffraction, and overlap of sidebands with the returned wave complicate the analysis of the reflectometry signal.

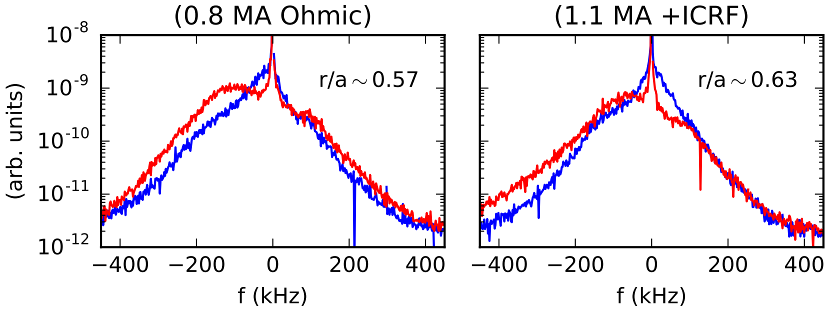

Figure 5-5: Reflectometry density fluctuation autopower spectra for Case I and III, corresponding to the profiles in Figure 5-3. Both in-phase and quadrature components of the signal were used. Spectra plotted in red correspond to LOC-like states, and ones in blue to SOC-like states. The spectra from co-current LOC-like states are broader than the ones from SOC-like rotation states.

The power in the signal is dominated by a low-frequency $|f| < 10$ kHz feature from electronics noise. Unfortunately it coincides with the peak of the spectrum in the SOC-like case, so it cannot be directly filtered out without removing a significant portion of the fluctuation power in the SOC-like case. The shift in the peak of the spectrum of about ~ 100 kHz would be consistent with the Doppler shift of $n \approx$ 10-20 modes, corresponding to $k_\perp \rho_s \approx$ 0.08-0.17. The width of the measured spectrum depends on a combination of the frequency spectrum of fluctuations in the plasma frame, the wavenumber-dependent sensitivity of the reflectometer diagnostic, and Doppler broadening $f_{tor} \Delta n$ over the range of active wavenumbers. Without further modeling it is difficult to provide additional quantitative interpretation of the data.

5.3.3 Correlation Electron Cyclotron Emission (CECE) Measurements

The data presented here are from the Correlation Electron Cyclotron Emission (CECE) diagnostic on Alcator C-Mod [116]. This system is sensitive to radially localized electron temperature fluctuations with $k_\theta \lesssim 10$ cm^{-1}, which within the rotation reversal region corresponds to $k_\theta \rho_s \lesssim 0.8$. The CECE measurements here result from the cross-correlation of two ECE signals which are separated in frequency space by an amount less than the ECE linewidth. In this case, the thermal noise is decorrelated between the two channels but the emission volume of the two signals will overlap in physical space. CECE fluctuation levels have been previously observed on Alcator C-Mod to decrease in SOC compared to LOC without a change in the dominant ion-scale linear instability from TEM to ITG [125, 115, 114]. However, these measurements were localized to outside the rotation reversal region. As part of the experiments in this thesis, measurements were attempted much further inside the plasma, $r/a \sim 0.65$ and 0.7, to try and characterize changes in fluctuations within the rotation reversal region. These data are shown in Figure 5-6.

Unfortunately, a combination of the weaker fluctuation levels further in the core of the plasma and a much shorter available window for averaging (60ms compared to

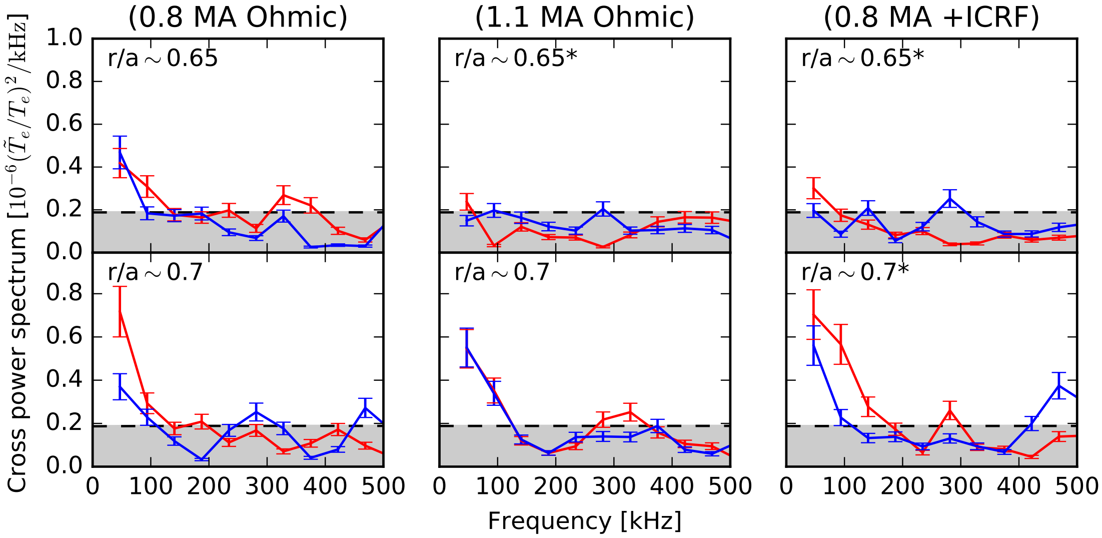

Figure 5-6: CECE cross-power spectra for the three experimental cases corresponding to the profiles in Figure 5-3. Red corresponds to LOC-like states, and blue to SOC-like states. Measurement locations within rotation reversal regions are marked with asterisks (*). The statistical noise level is shown in gray below the dashed line. Most of the measurements lie at or below the statistical noise level, so most turbulent fluctuations are not discernible from noise in these data.

500ms) led to most fluctuations being below the statistical noise level. The weaker $\tilde{T}_e/T_e$ fluctuations in the core are expected from the smaller gyro-Bohm normalized fluxes in the core (see Figure 6-4). While some of the spectra show stronger measured electron temperature fluctuations in LOC-like states outside the rotation reversal region, the error bars are too large to conclude that this is a robust result. Since the rotation does However, these measurements do provide the constraint that any changes in turbulence between the LOC-like and SOC-like states must be weak enough that they remain below the statistical noise limit within the rotation reversal region.

Chapter 6

Quasilinear Modeling and Subdominant Mode Collapse

In this chapter, linear and quasilinear gyrokinetic analysis is presented for experimental results from the previous Chapter. It will be shown that there is no change in dominant linear instability across the rotation reversal for the matched profiles. Furthermore, quasilinear analysis identifies a subdominant mode transition at intermediate $k_y \rho_s \gtrsim 1$ consistent with the transport inferred for the matched profiles.

For further analysis, the remainder of the chapter focuses on timeslices right before the LOC to SOC transition to try and characterize possible changes in turbulence as the transition occurs. Due to the lack of ion profile data from the presented experiments, linear and quasilinear gyrokinetic analysis was performed on density ramp shots from *Rice et al.*[103], corresponding to Case I and Case II.

6.1 Linear Gyrokinetic Stability

The gyrokinetic code CGYRO[16] was used in initial value mode, with gyrokinetic ions and electrons, and one gyrokinetic impurity species to match Z_{eff}. The Sugama model collision operator was used with experimentally calculated collision rates, experimental geometry used, and $\delta A_{\|}$ fluctuations were included. The calculated linear growth rates and real frequencies in the matched profile cases using profiles shown in

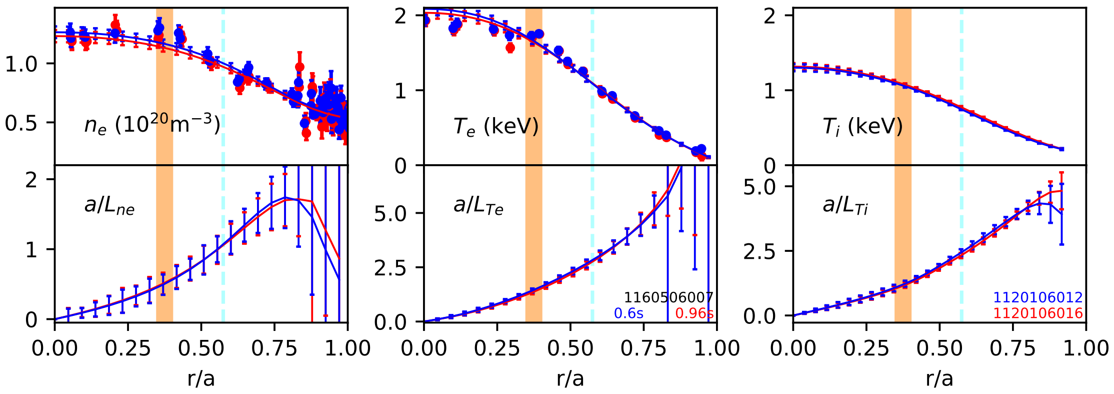

Figure 6-1: Profiles of electron density, electron temperature, and ion temperature and respective gradient scale lengths for the 0.8 MA case, for co-current LOC branch (red) and counter-current SOC branch (blue). The raw data are shown by the scatter points, and the fitted profiles with a smooth line. The orange shaded region is the approximate sawtooth inversion radius, and the dashed cyan line shows the location of the CGYRO simulations.

Figure 6-1, but differing rotation, are plotted in Figure 6-2

At nominal values of the gradients, the linear stability analysis does not show evidence of a transition from ion-direction to electron-direction dominance, either for the matched LOC/SOC profiles, or right before the transitions. This is consistent with linear stability analyses of Ohmic C-Mod, AUG, and DIII-D discharges, which have not shown a clear correlation between TEM↔ITG dominance transition and either the LOC/SOC transition or the rotation reversal [115, 114, 84, 77, 41, 50]. This radial location $r/a = 0.575$ remains ITG dominant when varying a single driving gradient within error bars, although variation outside of one standard deviation from the nominal value can lead to TEMs overtaking ITGs in growth rate, indicating that the plasma remains near a TEM↔ITG dominance transition.

This analysis is repeated for the density ramp shots from *Rice et al.*[103], corresponding to Case I and Case II, with results shown in Figure 6-3. The results of the analysis match that of the Case I result: near the transition, the dominant ion-scale instability is ITG. An interesting observation is that near the transition, the scales $k_y \rho_s$ where TEMs are dominantly unstable separate from the scales where ITGs are dominantly unstable, leaving a region near $k_y \rho_s \approx 1$ of modes which are strongly sub-

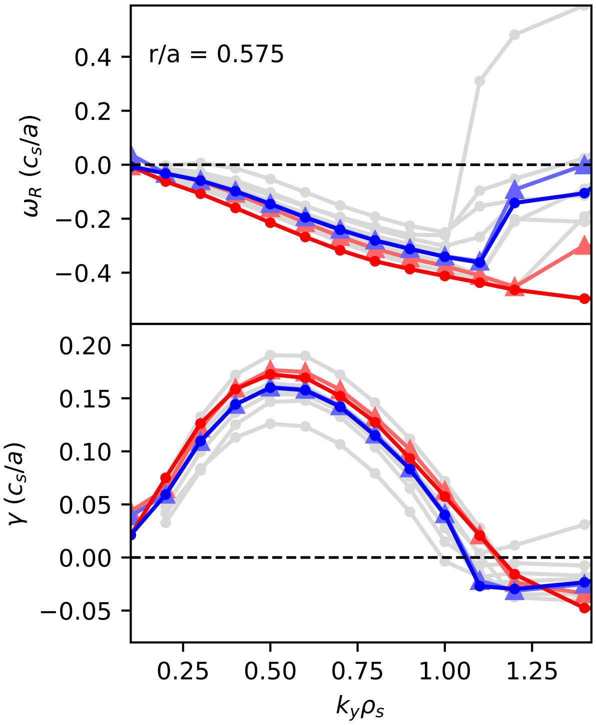

Figure 6-2: Real frequency (top) and growth rate (bottom) of most unstable mode at different $k_y\rho_s$. Several cases are plotted; the dark blue and dark red correspond to the matched profile conditions for counter-current and co-current cases, respectively. The light blue and light red, with triangle markers, correspond to conditions right before transition. Note the curves overlay each other very closely. The gray corresponds to variation of the driving gradients within error bars from the counter-current matched case.

dominant to the dominant ion-scale instability in linear growth rate. Additionally, a plot of the largest ion-scale growth rate is plotted against the $E \times B$ shearing rate calculated from force balance for co- and counter-current rotation profiles in Figure 6-3.

6.2 Reduced Quasilinear Model

To better understand the impact of the modes on transport and diagnose the turbulent state of the plasma, we adopt a quasilinear transport approximation (QLTA). In QLTA, the turbulent fluxes (e.g. the electron heat flux Q_e) are expressed as the sum of a quasilinear mode weight (for electron heat flux, this will be denoted $W_{Qe,k}$) times an averaged mode intensity (also called spectral weight, in this case $\left\langle \bar{\phi}_k^2 \right\rangle$) for each linear eigenmode indexed by wavenumber k. For example, writing this explicitly for the electron heat flux:

$$Q_e = \sum_k W_{Qe,k} \left\langle \bar{\phi}_k^2 \right\rangle \tag{6.1}$$

Adopting this model allows the separation of the linear physics of the plasma, encoded into the quasilinear weights, here assumed to be determined entirely by the structure of the linear eigenmodes, from the nonlinear physics of the plasma, encoded into the mode intensities determined by the nonlinear turbulence saturation mechanisms active in the plasma. While the validity of this approximation has not been rigorously established, in practice mQLTA has been surprisingly successful. Quasilinear weights have been found to match weights calculated from fully nonlinear simulation[120]. Density-temperature fluctuation cross-phases, which are related to the quasilinear weights, have been observed to match experimental measurements[126, 43]. This model also underlies modern quasilinear transport codes such as TGLF[111] and QualiKiz[10], which have shown success in replicating heat and particle transport in LOC/SOC transition scans.

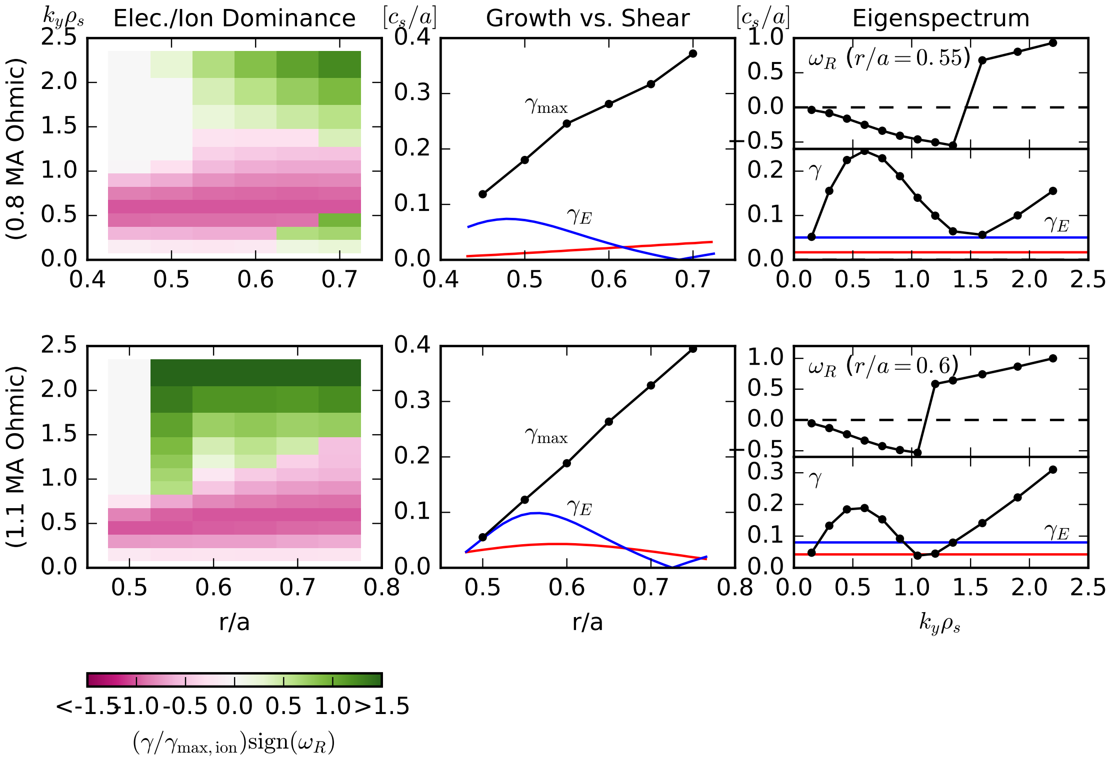

Figure 6-3: Plot of dominant linear instability as a function of $k_y\rho_s$ and r/a (left), the maximum ion scale linear growth rate against $E \times B$ shear (center), and the real frequency and growth rate plotted for a single radial location in the reversal region, with $E \times B$ shear plotted for comparison (right). Case I (top row) and Case II (bottom row) were analyzed. Negative frequency corresponds to ion-direction turbulence. For the dominant linear instability, the growth rates are normalized to the maximum ion scale linear growth rate, and show that ion-direction turbulence remains dominant over the entire plasma radius shortly before the rotation reversal. Next a plot of the maximum ion scale growth rate against the $E \times B$ shearing rate calculated from force balance is shown, where red and blue correspond to LOC and SOC respectively. Note the shearing rate reaches a significant fraction of the maximum ion scale growth rate. Finally, the linear spectrum for a single radius is shown.

6.2.1 Derivation of Reduced Model

Here, instead of being used in a predictive manner, mQLTA is used in a diagnostic manner. Using power balance, experimentally-derived turbulent fluxes can be utilized to provide a constraint on the possible mode intensities. Three fluxes are used: the electron and ion heat fluxes, and the electron particle flux. This analysis uses the power balance code TRANSP[11] and subtracts out the neoclassical component of the fluxes calculated from the code NEO[4]. The resulting anomalous fluxes are plotted in Figure 6-4. If the spectrum is discretized into N modes, then equation (6.1) and the corresponding equations for the other fluxes can be viewed as a $3 \times N$ matrix equation, as in equation (6.2):

$$\begin{bmatrix} Q_i \\ Q_e \\ \Gamma_e \end{bmatrix} = \begin{bmatrix} W_{Qi,k_1} & W_{Qi,k_2} & \cdots \\ W_{Qe,k_1} & W_{Qe,k_2} & \cdots \\ W_{\Gamma e,k_1} & W_{\Gamma e,k_2} & \cdots \end{bmatrix} \begin{bmatrix} \left\langle \bar{\phi}_{k_1}^2 \right\rangle \\ \left\langle \bar{\phi}_{k_2}^2 \right\rangle \\ \vdots \end{bmatrix} \approx \begin{bmatrix} W_{Qi,I} & W_{Qi,II} & \cdots \\ W_{Qe,I} & W_{Qe,II} & \cdots \\ W_{\Gamma e,I} & W_{\Gamma e,II} & \cdots \end{bmatrix} \begin{bmatrix} \left\langle \bar{\phi}_{I}^2 \right\rangle \Delta k_I \\ \left\langle \bar{\phi}_{II}^2 \right\rangle \Delta k_{II} \\ \vdots \end{bmatrix} \tag{6.2}$$

In the full system, N will be very large or infinite, so a naive application of the flux constraint leaves the mode intensities highly underdetermined. However, for the purpose of broadly determining trends in transport of the plasma, we do not need the detailed shape of the mode spectrum. For example, at electron scales corresponding to $k_y \rho_e \lesssim 1$, electron temperature gradient (ETG) modes will exhaust primarily electron heat flux without exhausting ion heat or particle flux, since ions will behave nearly adiabatically at that scale. Thus the net effect of ETGs on the turbulent fluxes can be well-approximated using only one degree of freedom, instead of using one degree of freedom per mode. This motivates the construction of a reduced transport model where similar modes are lumped together into 'families'. To calculate the total turbulent fluxes, the sum over modes is replaced with a sum over families, using quasilinear weights and spectral weights averaged over the modes in the family.

Additionally, here an explicit spectral width Δk has been included, which captures the number of modes in the original sum that the family replaces. This is represented in matrix form as in the second line of equation (6.2), where the families are enumerated by Roman numerals I, II, III, ... Note that the product $\left\langle \bar{\phi}_I^2 \right\rangle \Delta k_I$ represents a family-integrated spectral weight, while $\left\langle \bar{\phi}_I^2 \right\rangle$ alone is the family-averaged spectral weight.

6.2.2 Identification of Mode Families

Several radial locations were chosen for analysis, starting with the location of maximum $\omega'_{tor}(r)$, and proceeding radially outward until the points were outside the rotation reversal region. Quasilinear weights calculated from CGYRO are shown in Figure 6-4, for Case I and Case II. Despite being at different currents, the quasilinear weights look very similar between the two cases, with key features that are present in all analyzed locations:

- At ion scales $k_y \rho_s \lesssim 1$, the modes primarily exhaust ion heat flux, although there is a significant electron heat flux component as well. These modes are also thought to be responsible for most of the momentum transport in the plasma, as momentum will primarily be carried by ions. The electron particle transport starts outward at low k, but becomes increasingly inward directed as higher k are approached. For locations within the rotation reversal region, this inward trend is strong enough to reverse the direction of the particle flux. This ITG particle flux trend can be understood through a kinetic picture[1]. Collisions and diffusion cause outward particle fluxes, as is the case at low k. Ion finite larmor radius effects push the phase velocity of higher k modes closer to zero, causing the modes to be resonant with lower energy particles. Since temperature gradients produce an energy dependence in the radial gradient of the background Maxwellian distribution function which is of opposite sign to that produced by a density gradient at low energies, modes which are resonant with lower energy particles produce a stronger inward thermally-driven particle flux.

- At intermediate scales $k_y\rho_s \sim 1$, both ITG and a combined TEM/ETG branch are present. Occasionally ubiquitous modes[26] (modes with real frequency ≈ 0) can be observed in linear simulations at this scale. ITG and ubiquitous modes present at this scale tend to have strongly inward particle flux. TEMs which are active at this scale also have inward particle fluxes.

- At electron scales $k_y\rho_s \gg 1$, only a combined TEM/ETG branch is present. These modes are characterized by nearly adiabatic ions due to ion gyroaveraging over the small scales, and hence have weak ion heat and momentum flux, as well as weak particle flux due to the ambipolar nature of transport in axisymmetric systems[92].

Proceeding with the identification of families using the quasilinear weights, here we classify modes into dominant or subdominant families by the following criterion: At the location of maximum $\omega'_{tor}(r)$, calculate the ratio $\alpha \equiv \gamma_E/\gamma_{max}$. γ_{max} is the maximum ion scale linear growth rate, and $\gamma_E = \frac{r}{q}\frac{\partial\omega_0}{\partial r}$ is the shearing rate from ω_0, the $E\times B$ rotation rate calculated using force balance. Using the shearing rates right after the rotation reversal results in α of about 0.4 for the 0.8 MA Ohmic Case I, and about 0.7 for the 1.1 MA Ohmic case II. Then, across the entire profile, the subdominant modes are defined as modes with $\gamma_k < \alpha\gamma_{max}$, where γ_k is the maximum growth rate at each k_y. At the location of maximum shear, the subdominant modes correspond to modes which a naive application of the 'Waltz rule'[121] would suggest are quenched by the mean $E\times B$ shear in SOC, although the derived constraints are independent of whether or not the modes are actually quenched by the flow shear. Each contiguous component of subdominant modes on each branch of dispersion is grouped into a single family, allowing the identification of six families, shown in Table 6.1, with their main properties summarized. The naming scheme is somewhat arbitrary, as for example there is no discrete delineation between TEM and ETG. Additionally, note that this classification based on the linear growth rate is not the only possible way to group the modes into families, and consideration of other mechanisms including nonlinear mode coupling may suggest different classifications.

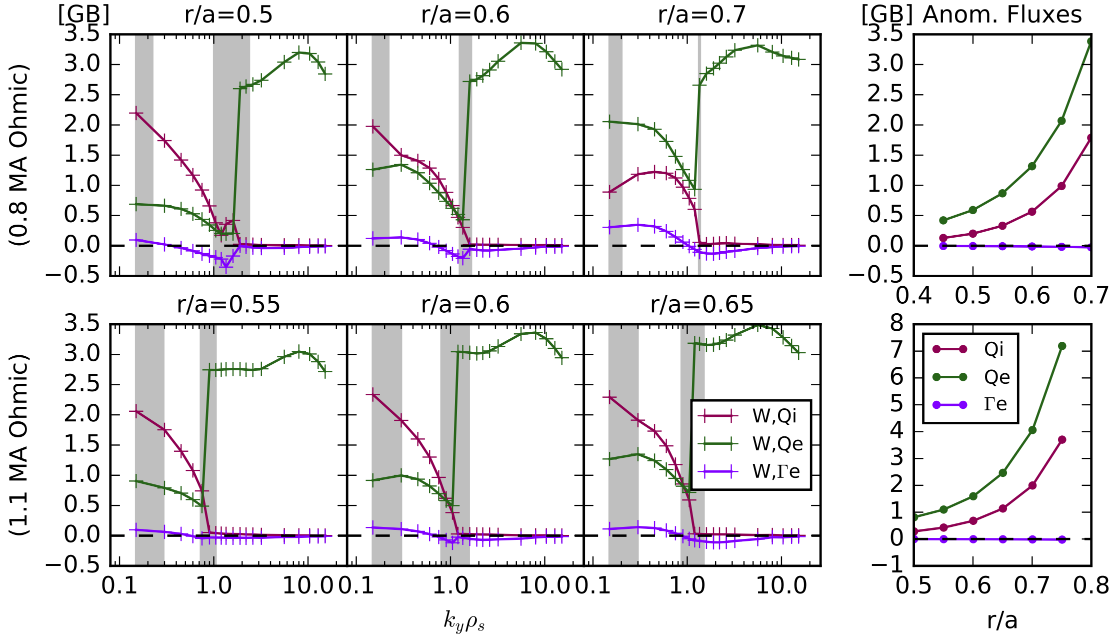

Figure 6-4: (Left) The quasilinear weights are shown for the most unstable drift wave modes at different radial locations, shortly before the rotation reversal, for the two Ohmic cases. (Right) The anomalous fluxes inferred for this timeslice are shown, plotted as a function of radius. The quasilinear weights and anomalous fluxes are both in gyro-Bohm units. The plot of anomalous fluxes shows how the particle flux is nearly zero, when compared to the ion and electron heat fluxes in gyro-Bohm units. For the quasilinear weights, the regions marked in gray are the 'subdominant' regions, where $\gamma_k < 0.4\gamma_{max}$ for Case I and $\gamma_k < 0.7\gamma_{max}$ for Case II. These gray regions define the subdominant mode families used in the quasilinear analysis.

Table 6.1: List of families used in the quasilinear analysis

Family	Description
ITGa	Low-k subdominant ITG. Always has outward particle flux
ITGb	Mid-k ITG. Has nearly balanced particle flux inside the rotation reversal region
ITGc	High-k subdominant ITG. Strong inward particle flux inside the rotation reversal region
TEMa	$k_y\rho_s \sim 1$ subdominant ∇T_e driven TEM. Always has inward particle flux. Ubiquitous modes are sometimes observed at this scale.
TEMb	$k_y r_b \lesssim 1$ ∇T_e driven TEM, where r_b is the typical banana orbit width. Also always exhibits inward particle flux, although is particularly strong outside the rotation reversal region. Some metrics of subdominance, such as comparing $\gamma/k_\perp^2$, find all TEMs to be subdominant and so do not have a TEMb family.
ETG	$k_y r_b \gtrsim 1$ ETG, exhausts primarily electron heat flux.

6.3 Subdominant Mode Collapse

With these families identified, the additional constraint that mode intensities must be non-negative distinguishes two qualitatively different solutions consistent with the transport constraints imposed by equation (6.2), based on whether or not the subdominant modes are active. Since neutral penetration from the edge is low and there is no beam fueling on Alcator C-Mod, the particle flux in the core is nearly zero. Since neutral penetration from the edge is low and there is no beam fueling on Alcator C-Mod, the particle flux in the core is nearly zero. The neoclassical particle pinch is not large enough to balance a significant turbulent particle diffusivity, so the active turbulent modes must provide the particle pinch necessary to have a balanced particle flux. One way to achieve this balance in the rotation reversal region is to only have the dominant ITG and TEM/ETG active, with the subdominant modes inactive. The particle flux constraint is satisfied primarily within the modes of ITGb, possibly with a small additional contribution from TEMb. This is possible because the particle flux weight of these modes averages to nearly zero for weights in the rotation reversal region. This leads to a narrower k spectrum of ion-scale turbulence, with electron direction turbulence quenched at ion-scales, corresponding to a “SOC-like” regime. Note that at large enough r/a, an increasingly large outward particle flux is driven by ITG due to increasing collisionality, so it is not possible for the particle balance constraint to be satisfied within ITGb alone. This necessitates significant activity from TEMa/b at these radii. Another possibility is to have both dominant and subdominant modes active. For this other solution, the subdominant ITGa is active, so either or both of ITGc and TEMa/b must have significant activity in order to balance the net particle flux. This leads to a broader k spectrum, with possibly intermixed ion- and electron-direction turbulence at ion-scales, corresponding to a “LOC-like” regime.

Since the “SOC-like” and “LOC-like” regimes continuously connect to the higher collisionality counter-current rotation and lower collisionality co-current rotation branches of the turbulent bifurcation, respectively, it is inferred that the rotation physics of

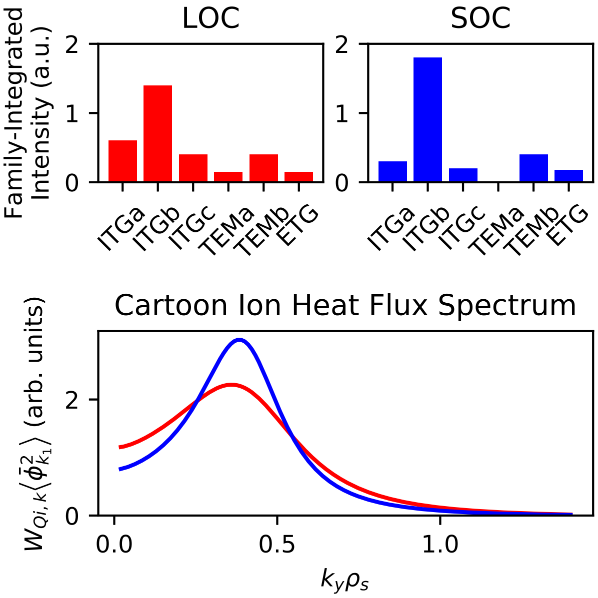

Figure 6-5: A qualitative illustration of the proposed LOC/SOC transition in the rotation reversal region. (Top) Example of six mode family-integrated intensities which would be consistent with the inferred transport via equation (6.2). Note the exact ratios between families are underconstrained, so these are only illustrative solutions. In SOC the subdominant families ITGa/c and TEMa are quenched in a way which respects particle flux constraint. (Bottom) An example ion heat flux spectrum which is consistent with the above mode families. Note the SOC spectrum in blue is narrower than the LOC spectrum in red.

ITG dominant or TEM dominant (but possibly ITG active) turbulence continues to be relevant closer to the transition in their respective regimes. The changes suggested by this model are illustrated schematically in Figure 6-5, and their consequences summarized in Table 6.2. One key implication is that despite heat transport being the principal externally driven means of turbulent free energy release in the plasma, modes which are subdominant in heat transport can play a role in determining the behavior of transport in other channels, such as particle or momentum transport.

Table 6.2: Summary of the consequences of the two possible turbulent states predicted by mQLTA.

Turbulent State	**LOC**	**SOC**
Active Mode Families	Broad ITG Ion- and Electron-Scale TEM ETG	Narrow ITG Electron-Scale TEM ETG
Particle Flux Balance	ITG balances TEM	Balance within ITG
Ion Heat Transport	TEM giving way to ITG	Primarily ITG
Electron Heat Transport	Ion and Electron Scale	Primarily Electron Scale
Torque Balance	TEM and ITG	ITG dominates

Chapter 7

Physical Mechanisms of the Transition

In order to fulfill the stated goal of understanding the feedback mechanisms leading to the LOC/SOC transition, we would like to know what constraints hysteresis places on the possible physical mechanisms underlying the observed dynamics. In the typical view of plasma turbulence, fluctuations grow due to down-gradient fluxes in the plasma, which release thermodynamic free energy. In a quasilinear picture, the energy of these fluctuations is located mostly in linear eigenmodes of the system, and the total transport is determined when the energy transfered from the active modes to dissipation by nonlinear interactions balances the pumping of the modes by the linear growth rate for the relaxed mean profile, leading to a saturated state of turbulence. This model was implicit in the earlier sections, particularly in the discussions of Sec. 2.4.2. These assumed that a decrease in the linear growth rate of the turbulence would lead to a decrease in the saturation level of the turbulence, and hence a reduction in transport. However, upon looking at this viewpoint critically, it leaves open the possibility that changing saturation mechanisms, rather than changing linear drives, could cause the transition. This section will describe some possibilities for changes in saturation which could underlie the turbulent transition.

While this work does not suggest a mechanism leading to the observed bistability of the turbulent state, it does identify constraints on the possibilities. The experimentally observed matched density and temperature profiles, both in mean value and gradients, show that the bistability cannot be explained by changes in the linear instability drive terms alone. Although not systematically ruled out, the robustness of the hysteresis to perturbation from LBO injection also suggests that the crossing of an undetected linear stability boundary is not responsible for the transition. This is due to the large effect of LBO on the linear stability of the plasma[105, 106]. Additionally, while profile shear has been identified as being important to intrinsic rotation[14, 57], these experiments suggest that changing profile shear is not responsible for the transition itself. However, the experiments do not rule out profile shear being responsible for setting the final steady-state shape of the rotation profile.

7.1 Possibilities Within Mean Field Theory

Local mean-field mechanisms for bistability are not entirely ruled out by the profiles, as change of the mean rotation profile could feedback on the plasma turbulence. The $E \times B$ flow shear is not large enough to entirely quench the ion-scale turbulence, but the shearing rate is a significant fraction of the maximum linear growth rate at ion-scales, as shown in Figure 6-3. Thus the flow shear could play a role in the saturation of subdominant modes, creating a situation resembling a ‘population collapse’ posited by predator-prey models of turbulence at the L-H transition, see e.g. *Diamond et al.*[29]. Here, only a portion of the ion scale spectrum collapses at the transition due to the formation of a shear layer, instead of its entirety. Experimentally this could be manifested in several ways: for example as a change in fluctuation intensity spectra, fluctuation correlation lengths, or fluctuation cross-phases, all of which could possibly be measured on present-day devices. However, nonlinear mode interactions are important in determining the response of modes to the $E \times B$ flow shear [6, 53, 121]. Thus it is premature to conclude that changing flow shear is the primary driver of changing turbulence on the basis of the comparison of the linear growth rate of subdominant modes to the shear rate.

7.2 Possibilities For Meso- or Micro-Scale Changes

Looking beyond mean field dependencies, other mechanisms for bistability could involve a change in meso- or micro-scale structure leading to a change in the mode-mode or mode-zonal flow nonlinear energy transfer. At a basic level, ITGs are predominantly observed to saturate by coupling to zonal flows, while TEM saturation is found to be insensitive to the presence of zonal flows in some parameter regimes[79, 86, 80, 40]. $T_e/T_i \approx$ 1.2-1.4 and $\eta_e \approx$ 2-3 in the rotation reversal region for the presented experiments, which may be a regime of weak zonal flow damping of TEMs. Simulations have suggested the importance of turbulent particle transport or zonal density in the saturation of TEMs[86, 80], although it is unclear why zonal flows become an ineffective saturation mechanism, and what relevance if any this plays in the LOC/SOC transition. The rest of this section will discuss other possibilities for changes in meso- or micro-scale structures relevant to the LOC/SOC transition, although the suggestions are not mutually exclusive, and do not comprise an exhaustive list.

One such change is suggested by Figure 7-1, where the perpendicular group velocity in the flux surface $v_{gr} = \frac{\partial \omega(k_y)}{\partial k_y}$ is compared to the phase velocity in the same direction $v_{ph} = \frac{\omega(k_y)}{k_y}$. Visually, $v_{ph} \approx v_{gr}$ for an intermediate scale $k_y \rho_s$ from 2-5, implying waves in that range are weakly dispersive. The existence of this range can be understood from the fact that the ratio of the thermal banana orbit width to the ion sound gyroradius $\Delta r_b/\rho_s \approx 0.062$ is small, so there exists a range of scales where $k_y \rho_s$ is large enough that ions are largely adiabatic while $k_y \Delta r_b$ is small enough that finite banana orbit width effects have yet to become important. Thus, TEMs at ion-scales are not expected to have this weak dispersion. Since the wave group velocity matches the phase velocity over a wide range in k, wave packets would travel with resonant particle trajectories in the absence of nonlinear scattering. As has been pointed out in the past[128, 73], since trapped electron bounce centers precess toroidally and do not decorrelate from the wave due to parallel streaming, they can remain at a fixed phase with the wave. This is contrasted with electrons and ions in passing orbits,

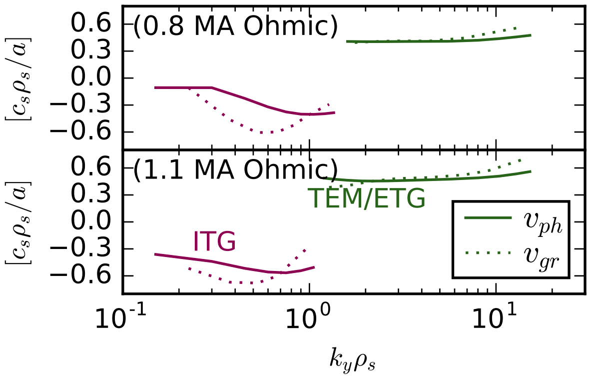

Figure 7-1: A plot of wave phase velocity v_{ph} (solid lines) and group velocity v_{gr} (dashed lines), for Case I (top) and II (bottom) both at $r/a = 0.6$. The ITG branch (magenta) and TEM/ETG branch (green) are shown in different colors. Note that v_{gr} follows v_{ph} more closely for the TEM/ETG branch than it does for the ITG branch. The text discusses this more quantitatively.

which rapidly decorrelate with the wave phase due to parallel streaming. This long field-particle interaction time could lead to a large deflection of the trapped electron bounce center from its unperturbed trajectory. Such large deflections would lead to the breakdown of quasilinear theory, which is based on 'small' kicks due to the response of particles to the perturbing fields.

This breakdown is signaled quantitatively by the Kubo number $\mathcal{K} \equiv \tau_{ac}/\tau_S$ crossing unity. Here τ_{ac} is the autocorrelation time of the fields (in this case, electrostatic potential) as seen by resonant particles on unperturbed trajectories, and τ_S is the 'bounce' time of the resonant particle in the field pattern, after which the usage of unperturbed trajectories for resonant particles will fail. See Appendix A for a more quantitative discussion of how this condition arises. Some prototypical examples of τ_S are in Current Driven Ion Acoustic (CDIA) turbulence where $\tau_S^{-1} = k\sqrt{q\tilde{\phi}/m_i}$ is the bounce time of a particle in an electrostatic well of amplitude $\tilde{\phi}$ formed by the ion acoustic wave, or in fluid $E \times B$ turbulence where $\tau_S = \tilde{V}_E/\lambda_c$ is the eddy circulation time with λ_c as the characteristic eddy length[108]. Here, the symbol τ_S is used to prevent confusion with the bounce time of particles in banana orbits τ_b in the magnetic well, and emphasizes that this is an effect due to the long interaction time between particles and an eikonal phase S of the wave.

With this physical picture in mind, the proximity of v_{gr} to v_{ph} can now be estimated. Note that these are order of magnitude estimates, as the experiments do not tightly constrain many of the relevant values, and are presented here to inform future work rather than to claim any particular conclusion. For ITG, there are contributions from both parallel streaming and perpendicular particle drift motion relative to the group velocity, which we can estimate a typical time as $\tau_{ac,\|} \approx qR/v_{ti} \approx 5.4a/c_s$ and $\tau_{ac,\perp} \approx |(v_{ph} - v_{gr})\Delta k_y|^{-1} \approx 5a/c_s$, where $\Delta k_y \rho_s \approx 1$ for ITG and the phase and group velocity of the most unstable mode were taken. Thus $\tau_{ac} = (\tau_{ac,\|}^{-1} + \tau_{ac,\perp}^{-1})^{-1} \approx 2.6a/c_s$ For the ITGb family, by using the values from Figure 6-4 in equation (6.2), the experimental heat flux requires a saturation amplitude of $\left\langle \left| \frac{e\tilde{\phi}}{T_e} \right|^2 \right\rangle \frac{a^2}{\rho_s^2} \approx 1$ in the rotation reversal region. Using $T_e \approx 1.2T_i$ and considering a peak $k_y \rho_s \approx 0.5$, this amplitude corresponds to a typical RMS velocity of $\tilde{V}_E \approx 0.4 c_s \rho_s / a$. Then for radial eddies of size 2-10 ρ_s, the ITG Kubo number will be $\mathcal{K} \approx$0.5-0.1, which marginally satisfies the requirements for quasilinear theory to hold.

In contrast to this situation, for TEMs in the absence of collisions, the decorrelation will be due to the relative difference of the bounce center toroidal precession and the group velocity, and can be estimated as $\tau_{ac} \approx |(v_{ph} - v_{gr})\Delta k_y|^{-1} \approx 25a/c_s$ where the spectral width $\Delta k_y \rho_s$ is taken to be 4, which is the spectral range over which the phase velocity closely follows the group velocity. For the TEMb family, a mixing length estimate constrained by the experimental fluxes suggests a saturation amplitude of $\left\langle \left| \frac{e\tilde{\phi}}{T_e} \right|^2 \right\rangle \frac{a^2}{\rho_s^2} \approx 0.1$ in the rotation reversal region, so $\mathcal{K} \gtrsim 1$. Thus the TEMb family, when it is active, requires additional decorrelation mechanisms to satisfy a necessary condition for weak turbulence in LOC. Note here the effect of mean flow shear, zonal flow shear, and other forms of radial shear on the Kubo number have not been taken into consideration. These could contribute to an enhanced decorrelation rate through the mechanism of shear-enhanced dispersion [6, 53, 23].

As the transition is approached, the TEM amplitude decreases, lengthening τ_S. Concurrently the collisionality increases, causing trapped electrons to be scattered into passing orbits, rapidly shortening τ_{ac}. Finally, the magnitude of the mean flow shear also increases significantly in the rotation reversal region. These effects suggest that $\mathcal{K}$ decreases as the LOC/SOC transition is approached, suggesting the possibility of a transition from strong TEM turbulence to weak TEM turbulence may be involved with the transition. This transition could involve trapped electron coherent phase space structures in LOC, which disappear in SOC due to the stronger decorrelation mechanisms. These structures may take the form of coherent radial streamers, which have been observed in simulations of strong collisionless TEM turbulence[128]. However, note that $\mathcal{K} < 1$ is a necessary but not sufficient condition for weak turbulence to hold, and other timescales such as the Dupree trapping time[36] need to be considered in order to determine if this strong to weak transition would actually occur.

An interesting meso-scale transition which could be involved in LOC/SOC is the formation of staircases. Staircases are self-sharpening zonal $E \times B$ flow patterns, named after their planetary analogue[33]. The possibility of staircases being involved in LOC/SOC was raised by observations in *Hornung et al.*[58], where quasi-regularly spaced local reductions in the radial turbulence coherence length were observed in SOC but not in LOC. Staircases could form from inhomogeneous mixing exhibiting bistability in the flux-gradient relationship. Staircase steps can merge to form larger shear layers[3]. The suggestion here would be that the fate of staircases would differ between LOC and SOC, possibly due to the stronger presence of TEM in the former. In LOC, staircases would either not form, or not merge into large-scale shear layers, while in SOC, staircases would form and merge into the observed shear layer. One mechanism which could lead to this situation is suggested by the strong to weak turbulence transition mentioned earlier. In LOC, coherent trapped electron phase space structures could form. These would act similarly to coherent vortices in atmospheric flows, which are known to punch through planetary staircases when the vortex strength is large enough compared to the staircase potential vorticity step [35].

Chapter 8

Summary, Discussion, and Future Work

In summary, this thesis presents hysteresis experiments which provide a novel probe of the LOC/SOC transition and rotation reversal. The two transitions are shown to be linked to a single bifurcation of the turbulent state, showing that LOC and SOC correspond to different states of turbulence, with elements of this bifurcation persisting in auxiliary heated plasmas. Plasmas with density and temperature profiles indistinguishable within error bars are shown to manifest different rotation states, placing tight constraints on possible mechanisms for the rotation reversal. The hysteresis is observed to be robust to perturbative cold pulse injection, showing conclusively that a change in dominant ion-scale instability from electron-directed to ion-directed alone cannot be responsible for the LOC/SOC transition. Despite having nearly identical drive terms, differences in measured turbulent fluctuations are observed in some circumstances across the transition. Similar phenomena are observed in auxiliary heated L-modes, suggesting the relevance of the bifurcation to more general transport trends in L-mode. A reduced quasilinear transport model used experimentally-inferred turbulent fluxes to provide constraints on the possible modes active in the turbulence. This analysis identified a change in the mix of mode saturation levels as a candidate explanation for the rotation reversal, implicating a subdominant mode population collapse as the physical mechanism underlying the observed bifurcation in turbulent fluctuations and momentum transport. This associates the LOC/SOC transition with the collapse of a subdominant intermediate-scale TEM population, rather than with a change in dominant linear instability from TEM to ITG. The relevance of physics beyond the quasilinear approximation was also explored, noting the possibility of a change from strong to weak TEM turbulence suggested by changes to the Kubo number across the transition.

The hysteresis experiments presented here provide a stepping stone for future inquiry that could lead to a full dynamical explanation of the LOC/SOC transition and rotation reversal. Many open questions remain, since the validity of the quasilinear approximations is called into question in this work, and the mechanism underlying bistability has yet to be identified. Additionally, the link between how changes in turbulence lead to the observed changes in residual stress is still missing. The analysis hints at the nonlinear physics needed to construct reduced dynamical models to describe the LOC/SOC transition, such as predator-prey models of the sort used to describe the L-H transition. The experiments also suggest the possibility of numerical hysteresis experiments in global nonlinear simulations, which could probe the residual stress physics independent of the linear drives. The analysis also provides possible observable consequences of the bifurcation which could be seen on present-day devices, providing interesting future experimental avenues of investigation as well.

8.1 Impacts on Reactor Design

While this work concludes that a nonlinear bifurcation underlies the LOC/SOC transition, we have yet to address the impact on reactor design. While the bulk of the thesis was about characterizing this bifurcation from an experimental and physical point of view, this section will now discuss its impact in the larger context of fusion energy. In particular, the work showed that the nonlinear bifurcation persists in auxiliary heated L-modes, raising the question of how or if the LOC/SOC scaling manifests in high-performance plasmas. This section will discuss questions raised by the conclusions of this thesis: is the transition relevant to reactor regimes? What does the transition say about confinement scalings outside of Ohmic scalings? And what role does rotation play in confinement?

8.1.1 Is the Transition Reactor-Relevant?

This work established that the same nonlinear bifurcation present in Ohmic plasmas also separates turbulent states in auxiliary heated L-modes. Note that transitions similar to the LOC/SOC transition in energy confinement time have also been observed in density ramps of plasmas heated with electron auxiliary heating [119, 88], so this is perhaps not necessarily that surprising. However, it does further reinforce the importance of understanding whether or not this confinement transition will occur for reactor-relevant plasmas.

While most reactors are designed around H-mode plasmas, there has been a recent resurgence of interest L-mode reactor concepts through the observed performance of negative triangularity L-mode plasmas [85, 70]. Such L-mode plasmas would have the benefit of being naturally ELM-free, less sensitive to radiative fraction at the edge, and would not have a minimum power threshold for access to high-performance regimes. It has been proposed that on TCV and DIII-D, the observed improvement in confinement was due to the stabilization of TEMs by negative triangularity, even for plasmas where $T_e \sim T_i$. However, results on TCV also showed this confinement improvement disappearing at high collisionality [15]. Given that the LOC/SOC transition is thought to be due to increasing collisionality at higher densities, and that this work shows this bifurcation persists in auxiliary heated L-mode plasmas, this work suggests that a similar transport bifurcation may exist in high performance negative triangularity regimes for high enough collisionalities. Thus, a firmer understanding of the collisionality dependence of the LOC/SOC transition may inform extrapolation of negative triangularity plasma performance to higher collisionality plasmas. While this work has not provided new quantitative estimates of the scaling, it does rule out scalings based on the growth rate of the linear instabilities alone.

The scaling of the LOC/SOC transition density with other plasma parameters is still not well understood. Two explanations that have been proposed are that the transition occurs at a critical collisionality ν_* [103], or when electrons and ions become sufficiently collisionally coupled (depending on both T_e/T_i and ν_{ei}) [41]. While this work has not provided new quantitative estimates of the scaling, it does imply that arguments based on the linear growth rates or collisional couplings alone cannot explain the LOC/SOC transition. In Ohmic plasmas, since most of the plasma parameters of interest are correlated (such as density and temperature at fixed current, or current and temperature at fixed density), it is difficult to probe the dependency of the transition on the relevant plasma parameters individually. Additional experiments on intrinsic rotation reversals in the presence of auxiliary heating may help break these correlations and improve understanding of when the transition occurs.

One final note is that so far, nothing in the arguments presented in the thesis so far suggest that the transition is limited to L-modes. It may be interesting to explore if a subdominant mode collapse of TEMs could occur in the core of H-or I-mode plasmas as well, and see if the consequences on transport are similar to the consequences on L-mode transport.

8.1.2 What Does the Transition Say About Confinement Scaling?

The biggest takeaway from this work is that the LOC and SOC branches of confinement scaling are not continuously connected when taking paths via density control or auxiliary heating for the parameter regimes tested here. An interesting question is whether or not the LOC and SOC branches then represent completely completely different states of plasma which cannot be connected by any path, or if these states could be connected through different parameter regimes. What this means is, for example, water with pressure and temperature below the critical point experiences a first-order phase transition between the liquid and gas phases. However, it is possible to continuously transform from a liquid to a gas without a phase transition by passing through a supercritical fluid state above the critical temperature or pressure. Such a transformation is possible because the liquid and gas states have the same symmetry properties [47]. Such a continuous transformation is not possible for the solid-liquid or solid-gas transition, which will always involve a phase transition due to the change in the symmetry properties of the phase. By determining the ‘phase diagram’ of confinement transitions, it would be possible to more productively sort discharges into different underlying turbulent states, with more accurate scaling laws being developed for the different classes of discharges. This is already done by the separation of discharges into L- and H-mode states, and could be extended further to ‘LOC-like’ and ‘SOC-like’ states.

This work also brings up questions about whether or not the plasma can be tailored to remain in the LOC branch or SOC branch. In the past, improved Ohmic confinement (IOC) scalings were observed as an (approximate) extension of the LOC scaling into much higher-collisionality plasmas, which would normally be SOC, via controlling edge conditions or via pellet injection. It was hypothesized that this improved confinement involved the stabilization of ITG modes by the increased density gradient, although it is unclear if the peaking of the density profile is the root cause of the improved confinement, or if it is a corollary of another transport change [119]. The observed turbulence bifurcation suggests a new interpretation of the difference between SOC and IOC through the dynamics of the subdominant modes. In IOC when the ITG stabilized, the formerly subdominant TEMs become dominantly responsible for transport. Noting that the net particle transport of the TEMs predicted by the quasilinear model is inward, this suggests the TEMs alone support a steeper density gradient than the mixed ITG/TEM state. This steeper density gradient would not get realized in SOC because of the presence of the ITGs, and by the quenching of subdominant TEMs at the transition.

Since auxiliary heated plasmas tend to be at lower collisionality than Ohmic plasmas, one might ask if it is possible to extend the SOC scaling into LOC collisionality regimes. An interesting experiment may be to identify there is hysteresis in the response of the energy confinement to scans of neutral beam injection (NBI) from co- to counter-current injection. For example, experiments on ASDEX found counter-current injection of NBI heating into L-mode discharges lead to improved confinement, while co-current injection of the same amount of NBI did not [46]. These experiments could probe the impact of the mean flow shear on the subdominant modes, and suggest new ways to tailor the performance of reactor plasmas that would only require injection of momentum to the rotation reversal region, not all the way into the plasma core.

8.1.3 What About Rotation?

This work suggests that one possibility for the LOC/SOC transition is from the self-consistent feedback of the toroidal rotation generated via turbulent residual stress on the saturated turbulent state. While the role of the residual stress and toroidal rotation shear is well known in the pedestal of H- and I-mode plasmas, as well as in internal transport barrier (ITB) plasmas, this conclusion would suggest the importance of self-consistent rotation modeling to predict transport for ‘plain’ turbulent plasmas without ITBs. This is outside of the range of current quasilinear codes, and suggests the need for additional work to be directed in the characterization of rotation in global gyrokinetic simulations for the construction of improved reduced models.

8.2 Avenues for Future Exploration

This section will discuss signatures of the proposed transition that could possibly be observed in experiment or in simulation, as well as theoretical approaches to gaining more insight into the dynamics of the transition. Since the physical mechanism underlying the transition hasn’t been determined, it is difficult to say with certainty what the signatures of the transition would be. For example, while the use of the word ‘collapse’ might suggest that looking for a significant drop in the power spectrum of electrostatic fluctuations at intermediate-k would be a sign of this transition, there are other ways that transport from this wavenumber range could be quenched. For example, the cross-phases could be randomized without a loss in amplitude of electrostatic fluctuations, which would lead to a quenching of transport but no observed change in the power spectrum. This would only be detectable by looking at fluctuation cross-phases.

8.2.1 Possibly Observable Experimental Signatures

This section will discuss what different experimental signatures, accessible through current or near-future diagnostics, would imply about the physical mechanisms of the LOC/SOC transition. A note of caution is that characterizing the relationship between fluctuations measured by turbulence diagnostics, and that of the actual turbulent state is non-trivial. However, performing hysteresis experiments on other tokamaks equipped with more extensive diagnostic systems could differentiate between the different physical mechanisms underlying the transition proposed in this thesis. As a reminder, the changes in turbulence identified by the quasilinear modeling are summarized in Table 6.2.

Turbulence Amplitude Diagnostics

The most direct interpretation of the subdominant mode collapse is that fluctuations at intermediate-k scales collapse in amplitude in the SOC branch. Some diagnostics, such as Doppler backscattering (DBS) systems, are able to directly measure fluctuations localized both in real space and in wavenumber space. For example, experiments on DIII-D observed a collapse in $k_\theta \rho_s \approx 1.5$-$2.0$ density fluctuations in radial locations corresponding to the rotation reversal region for SOC plasmas compared to LOC plasmas [50]. However, since these measurements were at higher density, it is not necessarily clear if these reduced fluctuations were due to a change in linear stability, as opposed to a change in the nonlinear saturation mechanisms. It may be interesting to repeat similar measurements for hysteresis experiments.

Non-Doppler reflectometry systems, which provide spatial localization but not wavelength localization, may also be another option for providing insight into changes in the turbulent state. While such reflectometry data was collected for the hysteresis experiments in this thesis, additional modeling with synthetic diagnostics would be required to disentangle the impact of changes in turbulence in the plasma frame versus changes in measured spectra from a change in Doppler shift. Significant work has been done to characterize such reflectometry spectra in LOC/SOC transition experiments on JET and Tore Supra. A quasi-coherent feature present in LOC but not in SOC was identified as a quasi-coherent TEM fluctuation from nonlinear simulation [24]. Futhermore, it was identified that TEM linear instability was not sufficient to create the QC-TEMs; some unidentified nonlinear effects were necessary to reproduce the observed quasi-coherent feature as well. WEST or KSTAR might be good testbeds for new measurements. The question here would be, do QC-TEMs disappear on the SOC branch and reappear on the LOC branch of hysteresis experiments? This may provide insight into the nature of the nonlinear processes responsible for creating the QC-TEMs.

Correlation Electron Cyclotron Emission (CECE) diagnostics are also capable of providing turbulence amplitude measurements which are localized in space but not in wavelength. Due to weak signal-to-noise ratio, the CECE measurements collected from the experiments in this thesis did not provide strong quantitative insight into changes in turbulence amplitude between the LOC-like and SOC-like turbulence states within the rotation reversal region. Previous measurements on Alcator C-Mod outside of the rotation reversal region do robustly observe a drop in electron temperature fluctuations going from LOC to SOC without a change in dominant ion-scale instability [125, 115, 114]. This is broadly consistent with the picture of a quench of subdominant ion-scale TEMs as LOC transitions to SOC. However, this interpretation comes with several caveats. The first is that the subdominant mode collapse proposed in this thesis only describes changes within the rotation reversal region. In the absence of turbulence spreading or other non-local effects a subdominant mode collapse in one region of the plasma would not necessarily manifest a change in turbulence in other regions of the plasma. The second is that ITG can also drive significant electron temperature fluctuations via the trapped electron response, which will change as a function of collisionality. Thus, changes in electron temperature fluctuations are not necessarily purely indicative of changes in TEM amplitude, and could also reflect changes in the collisionality profile rather than the turbulence bifurcation identified in this work. Experimental validation of the proposed subdominant mode collapse would thus require synthetic diagnostic development in combination with new CECE measurements in rotation reversal hysteresis experiments which are radially localized to the rotation reversal region. The CECE system on AUG may be capable of such measurements. Such experiments would not necessarily need to continuously ramp the density up and down in order to complete a full hysteresis loop, thus leaving much larger windows for averaging of the turbulent fluctuations.

Finally, line-integrated fluctuation measurements such as PCI may provide insight when other diagnostics are not available. However, detailed interpretation these measurements requires significant investment into synthetic diagnostics, and may leave the radial localization difficult.

Turbulence Correlation and Cross-Phase Diagnostics

As discussed in the physical mechanisms section, another way a subdominant mode collapse may manifest is as a dephasing of fluctuations at intermediate-k scales. In this case, the amplitude of fluctuations in this wavelength range could still be significant, but since the transport cross-phases have been randomized, this range of wavelengths would not be responsible for any turbulent transport. One way of observing this in experiments is through cross-phase measurements, such as done in AUG through CECE systems which share optics with a reflectometry system. This mechanism of subdominant mode collapse could be visible as a change in the measured density-temperature cross-phases without a corresponding change in the total amplitude of fluctuations. Another possibility is to look at fluctuation radial coherence lengths - a shortening of the radial coherence length would increase the decorrelation rate of particles with the wave as particles are transported radially, and hence would also correspond to a change in the quasilinear weight. If the coherence length changed without a change in turbulent amplitude, this would also be indicative of a subdominant mode collapse via change in the quasilinear weights.

8.2.2 Dynamics Visible in Simulation

In addition to experimental work, nonlinear simulation can also play a role in elucidating the physical mechanisms underlying the LOC/SOC transition. A major challenge in studying simulation comes from experimental uncertainty. Small changes in the profile gradients or other simulation inputs within error bars can have a significant effect on the simulated heat fluxes and other features of the turbulent state. Additionally, it is difficult to determine if the simulations include all physics relevant to the transition - for example, since the dynamics of the TEM/ETG branch is implicated in the transition, one would expect that a large enough portion of the TEM/ETG spectrum needs to be simulated in order to properly capture the possibility of energy cascading from the intermediate scales to the electron scales. Such simulations would need to be multiscale, and hence extremely computationally expensive. The impact of intermediate scales on global organization of turbulence through staircases and avalanching is also unclear.

With these caveats in mind, it is still possible to investigate individual parts of the proposed bifurcation via targeted nonlinear simulations. Possible numerical diagnostics of use in local gyrokinetic simulations would be frequency or k power spectra of the electrostatic potential fluctuations - similar to the experimental measurements, these could reveal a collapse of fluctuation amplitudes at the subdominant scales. Cross-phases and quasilinear weights are also more accessible in simulation, and could reveal quenching of transport via departure of the cross-phases from quasilinear predictions. Heat and particle flux spectra could also provide important clues as to which scales are active in transport. Bicoherence [64] and other third-order statistics could also provide insight into nonlinear energy transfer present in the system.

If the $E \times B$ shear were responsible for suppressing subdominant intermediate-scale modes, this hypothesis could be explored by running nonlinear local gyrokinetic simulations of plasmas near the transition with the same density and temperature profiles, but differing rotation shear corresponding to LOC (weaker shear) and SOC (stronger shear). It may be important to extend the simulation up to scales $k_y \Delta r_b \sim 1$, or equivalently $k_y\rho_s \approx 16$ since as discussed in the physical mechanisms section, the intermediate scale TEM branch with $\rho_s^{-1} \lesssim k_y \lesssim \Delta r_b$ is weakly dispersive and could possibly lead to strong nonlinear coupling of drift waves in this regime, leading to significant transfer of energy from scales where $\gamma_k > \gamma_E$ to the subdominant intermediate scales.

Running similar numerical experiments in global gyrokinetic codes could also provide insight into the symmetry breaking mechanisms responsible for the generation of the rotation in the first place. One could envision running "numerical hysteresis experiments", where a simulation is run for profiles near the transition in one rotation state until the saturation of turbulence is reached, then switch the rotation to the other state, then see how the saturated state of turbulence responds. Note that simulations in [50] observed the residual stress profile to be closely correlated with the structure of the $E \times B$ zonal flow shearing profile, with the rotation reversal corresponding to the formation of a large-scale dipolar structure in the zonal flow shearing rate. These numerical hysteresis experiments could provide insight into how robust this structure is at different plasma parameters, and also provide information on the dynamics of the structure formation, such as if it forms as the result of the merger of staircase steps.

8.2.3 Theoretical Approaches

The analogy between the L-H transition and the intrinsic rotation reversal suggests that the LOC/SOC transition may be amenable to predator-prey modeling. This modeling may be useful for identifying which physical mechanisms are necessary to capture the qualitative features of the transition. Such modeling could also identify possible scalings for the LOC/SOC transition density. However, predator-prey models of turbulence typically only have one population of drift waves, as including additional populations requires a description of how these drift wave populations interact. Using nonlinear simulation to inform how the drift waves interact, possibly through proper orthogonal decomposition (POD) techniques to identify the the relevant modes in gyrokinetic simulations [54], could help determine the importance of interactions between the different populations of drift waves. Dupree renormalization [36] or more formal direct interaction approximation (DIA) techniques [74] could also provide insight on how modes interact and on the possibility of a strong-weak TEM transition, although these methods would be significantly more difficult to handle analytically.

Appendix A

Aspects of Quasilinear Theory

This appendix briefly covers aspects of quasilinear theory relevant for the thesis. In particular, a motivation for studying the Kubo number is given. For detailed derivations and discussions on this topic, see [108, 74, 31].

A.1 Physical Content of Quasilinear Theory

Consider abstractly the following set of equations which describes a closed nonlinear advection equation by an incompressible flow:

$$\frac{\partial}{\partial t} f + \mathbf{u} \cdot \frac{\partial}{\partial \mathbf{z}} f = 0 \tag{A.1}$$

$$\mathbf{u} = \mathcal{U}[f] \tag{A.2}$$

$$\frac{\partial}{\partial \mathbf{z}} \cdot \mathbf{u} = 0 \tag{A.3}$$

Here $\mathbf{z}$ is some real space or phase space coordinate, $f = f(\mathbf{z}, t)$ is an arbitrary scalar function, $\mathbf{u} = \mathbf{u}(\mathbf{z}, t)$ is the flow velocity, and $\mathcal{U}$ is a (possibly nonlinear) functional which determines the flow pattern $\mathbf{u}(\mathbf{z}, t)$ in terms of the scalar function $f(\mathbf{z}, t)$. The incompressibility condition (A.3) is redundant for properly defined $\mathcal{U}$, but it is included for emphasis. This setup encompasses two important cases of the Vlasov-Poisson equations and the Charney-Hasegawa-Mima (CHM) equation, shown in Table A.1.

Abstract symbol	Vlasov-Poisson equations	CHM equation
f	Particle distribution function f	Potential vorticity q
$\mathbf{z}$	Phase space coordinates $(\mathbf{x}, \mathbf{v})$	Real space coordinates (x,y)
$\mathbf{u}$	Phase space velocity $(\mathbf{v}, q\mathbf{E}/m)$	$E \times B$ velocity $\mathbf{u}_E$

Table A.1: List of correspondences between the symbols in the abstract equations (A.1-A.3) and two important systems of study.

Take equation (A.1) and split it into a Reynolds averaged and fluctuating part, i.e. $f = \langle f \rangle + \tilde{f}$, which results in

$$\frac{\partial}{\partial t} \langle f \rangle + \langle \mathbf{u} \rangle \cdot \frac{\partial}{\partial \mathbf{z}} \langle f \rangle = -\left\langle \tilde{\mathbf{u}} \cdot \frac{\partial}{\partial \mathbf{z}} \tilde{f} \right\rangle \tag{A.4}$$

$$\frac{\partial}{\partial t} \tilde{f} + \langle \mathbf{u} \rangle \cdot \frac{\partial}{\partial \mathbf{z}} \tilde{f} + \tilde{\mathbf{u}} \cdot \frac{\partial}{\partial \mathbf{z}} \langle f \rangle = \left[\tilde{\mathbf{u}} \cdot \frac{\partial}{\partial \mathbf{z}} \tilde{f} - \left\langle \tilde{\mathbf{u}} \cdot \frac{\partial}{\partial \mathbf{z}} \tilde{f} \right\rangle \right] \tag{A.5}$$

Formally, these equations are exact. Equation (A.4) determines the evolution of the mean state, which depends on the fluctuations, interpreted as eddies, through the right-hand side of the equation. Since $\mathbf{u}$ is incompressible, we can write the right-hand side as the divergence of a turbulent flux,

$$-\left\langle \tilde{\mathbf{u}} \cdot \frac{\partial}{\partial \mathbf{z}} \tilde{f} \right\rangle = -\frac{\partial}{\partial \mathbf{z}} \cdot \left\langle \tilde{\mathbf{u}} \tilde{f} \right\rangle = -\frac{\partial}{\partial \mathbf{z}} \cdot \mathbf{F} \tag{A.6}$$

In order to calculate the turbulent flux, equation (A.5) is used to determine the evolution of the eddies. The term on the right-hand side of that equation relates to nonlinear eddy-eddy interaction. In the quasilinear approximation, we drop these nonlinear terms, resulting in the following linear equation:

$$\left[\frac{\partial}{\partial t} + \langle \mathbf{u} \rangle \cdot \frac{\partial}{\partial \mathbf{z}} \right] \tilde{f} = -\tilde{\mathbf{u}} \cdot \frac{\partial}{\partial \mathbf{z}} \langle f \rangle \tag{A.7}$$

The operator on the left-hand side of (A.7) can be formally inverted by solving for the Green's function G

$$\left[\frac{\partial}{\partial t} + \langle \mathbf{u} \rangle \cdot \frac{\partial}{\partial \mathbf{z}} \right] G(\mathbf{z}, t; \mathbf{z}', t') = \delta(\mathbf{z} - \mathbf{z}') \delta(t - t') \tag{A.8}$$

This PDE can be solved for via the method of characteristics,

$$G(\mathbf{z},t;\mathbf{z}',t') = \delta(\bar{\mathbf{z}}_c(t';\mathbf{z},t) - \mathbf{z}')H(t-t') \tag{A.9}$$

where $H(t-t')$ is the unit step function, and $\bar{\mathbf{z}}_c(t';\mathbf{z},t)$ is the time-reversed path of a particle following a mean flow characteristic which ends up at position $\mathbf{z}$ at time t, e.g. the solution to the ODE

$$\frac{\mathrm{d}}{\mathrm{d}s}\bar{\mathbf{z}}_c(t-s;\mathbf{z},t) = -\left\langle u(\bar{\mathbf{z}}_c(t-s;\mathbf{z},t),t-s)\right\rangle \tag{A.10}$$

$$\bar{\mathbf{z}}_c(t;\mathbf{z},t) = \mathbf{z} \tag{A.11}$$

Now, we can invert equation (A.7)

$$\tilde{f}(\mathbf{z},t) = -\int \mathrm{d}\mathbf{z}'\,\mathrm{d}t'\,G(\mathbf{z},t;\mathbf{z}',t')\tilde{\mathbf{u}}(\mathbf{z}',t')\cdot\frac{\partial}{\partial\mathbf{z}'}\left\langle f\right\rangle(\mathbf{z}',t') \tag{A.12}$$

which allows for the calculation of the turbulent flux seen in equation (A.6) as

$$F_j = \left\langle \tilde{u}_i(\mathbf{z},t)\tilde{f}(\mathbf{z},t)\right\rangle = -\sum_j\int \mathrm{d}\mathbf{z}'\,\mathrm{d}t'\,G(\mathbf{z},t;\mathbf{z}',t')\left\langle\tilde{u}_i(\mathbf{z},t)\tilde{u}_j(\mathbf{z}',t')\right\rangle\frac{\partial}{\partial z_j'}\left\langle f\right\rangle(\mathbf{z}',t') \tag{A.13}$$

where the subscript index refers to the component of a vector in some fixed basis. Assuming a scale separation between the time and spatial scales of $\left\langle f\right\rangle(\mathbf{z},t)$ compared to the fluctuating fields, which depend on $\mathbf{z}-\mathbf{z}'$ and $t-t'$, equation (A.13) can be written in a form reminiscent of a Fick's law:

$$\mathbf{F}(\mathbf{z},t) = -\mathbf{D}(\mathbf{z},t)\frac{\partial}{\partial\mathbf{z}}\left\langle f\right\rangle(\mathbf{z},t) \tag{A.14}$$

$$D_{ij}(\mathbf{z},t) = \int_0^\infty \mathrm{d}s\,\left\langle\tilde{u}_i(\mathbf{z},t)\tilde{u}_j(\bar{\mathbf{z}}_c(t-s;\mathbf{z},t),t-s)\right\rangle \tag{A.15}$$

where the integration over $\mathrm{d}\mathbf{z}'$ was performed using the Green's function (A.9).

Equation (A.15) represents one of the principal physical underpinnings of quasilinear theory. Particles (or equivalently, fluid parcels) are assumed to diffuse based on the statistics of $\tilde{\mathbf{u}}$, *as sampled along particle trajectories which are traveling only* *with the mean velocity* $\langle \mathbf{u} \rangle$. If the typical root mean square velocity is $\tilde{U}$ and the typical autocorrelation time of the field as seen along the mean trajectory is τ_{ac}, we see that $D \propto \tilde{U}^2 \tau_{ac}$. This corresponds to the physical picture of particles undergoing independent kicks $\tilde{U}/\tau_{ac}$ spaced τ_{ac} apart, then using to the central limit theorem to conclude that this results in a diffusive process.

The final approximation to employ is to use the linearized version of equation (A.2) (although it is not an approximation if $\mathcal{U}$ is linear) to determine the relationship between $\tilde{f}$ and $\tilde{\mathbf{u}}$ via

$$\tilde{\mathbf{u}} = \frac{\delta \mathcal{U}}{\delta f}[\tilde{f}] \tag{A.16}$$

which when combined with equation (A.7) and applying Fourier transforms for spatially homogeneous mean states $\langle f \rangle$ and $\langle \mathbf{u} \rangle$ typically results in a dispersion relation $\epsilon(\omega, \mathbf{k}) = 0$. This states that fluctuations at each $\mathbf{k}$ are primarily coherent fluctuations, $\tilde{f}_{\mathbf{k}} = \delta f^c_{\mathbf{k}}$, which satisfy the dispersion relation. For most plasma and fluid systems where quasilinear theory may conceivably apply, these coherent fluctuations take the form of waves, possibly with non-zero growth or damping rates. Thus, quasilinear theory can be thought of as fluctuations consisting of traveling wavepackets supported by the mean state of the medium, which feeds back on the medium via equation (A.13), plus resonant particle fluctuations.

One thing to note is that due to the wave nature of the fluctuations, the fluctuations will have well-defined propagating wave phase fronts. If the mean particle trajectories are not synchronized with these phase fronts, then the integral in equation (A.15) will average over the phase of the wave, leading to zero diffusion. This is the real-space version of the resonance condition requirement for irreversible transport. This leads to a natural linkage in Hamiltonian systems between the appearance of irreversibility in quasilinear theory and the onset of chaos due to resonance overlap. This leads to the Chirikov island overlap criterion [31] as a necessary condition for quasilinear theory to be valid, i.e. for chaotic flow to cover large regions of phase space which supports particle orbit stochasticity.

A.2 Breakdown of Quasilinear Theory via Particle Trapping

This diffusive picture can be contrasted with the situation without approximation. Consider the statistics of a particle or fluid element flowing in the full velocity field $\mathbf{u}$,

$$\frac{\mathrm{d}}{\mathrm{d}t}\mathbf{z}_p(t) = \mathbf{u}(\mathbf{z}_p(t), t) \tag{A.17}$$

$$\frac{\mathrm{d}}{\mathrm{d}t}\left\langle \mathbf{z}_p(t)\mathbf{z}_p(t)\right\rangle = 2\int_0^\infty \mathrm{d}s \left\langle \mathbf{u}(\mathbf{z}_p(t), t)\mathbf{u}(\mathbf{z}_p(t-s), t-s)\right\rangle \tag{A.18}$$

While equation (A.18) is superficially reminiscent to diffusion suggested by equation (A.15), notice that the integrand depends on the entire history of the *full* particle path $\mathbf{z}_p(t)$, not just the characteristics along the mean flow. The kicks the particle experiences at time t are not independent of the kicks experienced at earlier times, and hence the central limit theorem cannot be applied without additional assumptions.

One way to quantify the departure of the true particle trajectories from the quasilinear estimate is via the Kubo number, $\mathcal{K} \equiv \tau_{ac}/\tau_S$. Here τ_{ac} is given a precise definition as the decay time of the integrand $\langle \tilde{u}_i(\mathbf{z}, t)\tilde{u}_j(\bar{\mathbf{z}}_c(t-s; \mathbf{z}, t), t-s)\rangle$, and τ_S is the 'bounce' time of a resonant particle in the field pattern. This was originally studied in the context of random modulations of an oscillator frequency [75], and connects to the study of turbulence as a prototypical example of the impact of multiplicative noise on the linear response function [74]. The symbol τ_S is used to instead of the usual τ_b to prevent confusion with the banana orbit bounce time, and emphasizes the connection to the eikonal phase S of the waves.

One prototypical example of τ_S comes from Current Driven Ion Acoustic (CDIA) turbulence. Consider a particle in 1-D in the frame moving with the phase velocity of an electrostatic wave. The Hamiltonian for this situation is given by

$$H = \frac{p^2}{2m} - q\phi\cos(kx) \tag{A.19}$$

which is the same form as the Hamiltonian for a pendulum. Taking the harmonic oscillator approximation for the particle motion, the time evolution of a particle starting with $p(0) = 0$, $x(0) = x_0$ (representing an initially resonant particle) is

$$p(t) = mx_0/\tau_s \sin(t/\tau_S) \tag{A.20}$$

where $\tau_S^{-1} = k\sqrt{q\phi/m}$. If $\mathcal{K} \ll 1$, then the particle only has a chance to travel for a time $t \lesssim \tau_{ac} \ll \tau_S$ before it sees a new wave phase. Then, taking $x_0 \sim k^{-1}$ equation (A.20) can be approximated using $\sin\theta \approx \theta$ as

$$p(t) - p(0) \approx mx_0/\tau_s^2 t \sim qk\phi\tau_{ac} \tag{A.21}$$

so we see that the particle experiences a kick of $\Delta p = q\tilde{E}\tau_{ac}$. This matches the diffusive scaling estimate given earlier. However, in the opposite limit, if $\mathcal{K} \gg 1$, then the linearized trajectory of the particle cannot be used. The kick does not scale with τ_{ac}. Thus $\mathcal{K} \ll 1$ is a necessary condition for quasilinear diffusion estimates to hold.

Appendix B

Gaussian Process Regression

This appendix will discuss what in more detail the assumptions and inputs needed for Gaussian Process Regression (GPR), and explain more precisely what “rigorous quantification of uncertainty” means in the context of profile fitting for transport modeling and falsifiability. Advantages of GPR over spline fitting methods are also discussed.

B.1 Explanation of Gaussian Process Regression

Gaussian Process Regression (GPR), originally known as kriging [83], as used in this thesis is a method for inferring mean profiles of density, temperature, and rotation (as differentiable functions of some flux surface label) from the discrete and noisy measurements provided by experimental diagnostics. These profiles are then used as inputs to the transport models used in this thesis. As the class of differentiable functions over an interval has an infinite number of degrees of freedom, the mean profiles are underdetermined for any finite number of measurements. Thus, some choice has to be made on how to determine which mean profiles represent the data ‘better’ than other ones. Since measurements are necessarily noisy, this suggests a probabilistic approach will need to be taken.

This section will introduce time-independent one-dimensional GPR, which is used for inferring time-averaged kinetic profiles. GPR presumes that the experimental measurements, denoted here as the set of measurements $\{y_i\}$ at locations $\{x_i\}$, can be modeled as samples drawn from a Gaussian process plus Gaussian measurement noise. A Gaussian process is a special case of a stochastic process, which can be thought of as a function mapping each point in space to a random variable. For Gaussian processes, the joint probability distribution of any finite collection of those random variables will be a multivariate Gaussian distribution. Gaussian processes can be thought of as infinite-dimensional generalizations of multivariate Gaussian distributions. Just like how an n-dimensional multivariate Gaussian distribution is completely specified by an n-dimensional mean vector $\boldsymbol{\mu}$ and $n \times n$ symmetric covariance matrix $\boldsymbol{\Sigma}$, a Gaussian process is completely specified by a mean function $m(x)$ and symmetric covariance kernel $k(x, x') = k(x', x)$.

The problem of evaluating mean profiles and their uncertainties given the experimental measurements can now be restated in probabilistic terms as evaluating the functions $\bar{y}_*(x_*) = \mathbb{E}[y_*|\{y_i\}]$ and $\Sigma(x_*, x'_*) = \mathrm{Cov}[y_*, y'_*|\{y_i\}]$ respectively. Here y_* is the value of the Gaussian process without measurement noise measured at location x_*. We follow Chilenski [21] and set $m(x) = 0$. Then, if we specify the covariance kernel $k(x, x')$ and the measurement noise covariance matrix Σ_{ij}, these can be calculated as

$$\bar{y}_*(x_*) = \mathbf{K}(x_*, \mathbf{x}) \left[\mathbf{K}(\mathbf{x}, \mathbf{x}) + \boldsymbol{\Sigma}_n\right]^{-1} \mathbf{y} \tag{B.1}$$

$$\Sigma(x_*, x'_*) = k(x_*, x'_*) - \mathbf{K}(x_*, \mathbf{x}) \left[\mathbf{K}(\mathbf{x}, \mathbf{x}) + \boldsymbol{\Sigma}_n\right]^{-1} \mathbf{K}(\mathbf{x}, x'_*) \tag{B.2}$$

The symbols in these equations are defined in Table B.1.

Symbol	Definition
$\mathbf{y}$	n-component column vector of experimental measurements y_i
$\boldsymbol{\Sigma}_n$	$n \times n$ noise covariance matrix with components Σ_{ij}
$\mathbf{K}(\mathbf{x}, \mathbf{x})$	$n \times n$ matrix with components $k(x_i, x_j)$
$\mathbf{K}(x_*, \mathbf{x})$	function mapping x_* to the n-component row vector $k(x_*, x_i)$
$\mathbf{K}(\mathbf{x}, x'_*)$	function mapping x'_* to the n-component column vector $k(x_i, x'_*)$

Table B.1: Definition of symbols in (B.1) and (B.2), for n experimental measurements. This entirely specifies the inputs required to calculate mean profiles and their uncertainties given the experimental data.

These closed-form analytic expressions for both the mean profiles and their uncertainties represent a significant gain over nonlinear spline fitting routines in terms of uncertainty quantification. While uncertainty in nonlinear fit routines must typically be numerically approximated using sampling routines, here the uncertainty (and moreover the entire covariance kernel) is immediately accessible given the covariance kernel and measurement noise covariance matrix. Additionally, the mean gradients and their uncertainties are also immediately accessible by taking the derivatives of equations (B.1) and (B.2). This comes from the fact that the derivative is a linear operator, and transforms the Gaussian process in analogy to how a linear transformation $\mathbf{B}$ of a multivariate Gaussian transforms the mean $\boldsymbol{\mu} \mapsto \mathbf{B}\boldsymbol{\mu}$ and covariance $\boldsymbol{\Sigma} \mapsto \mathbf{B}\boldsymbol{\Sigma}\mathbf{B}^T$. Note this implies that the smoothness (used here in the technical sense of the number of continuous derivatives) of the fit profile depends on the smoothness of the covariance kernel $k(x, x')$.

B.2 Choice and Physical Interpretation of Covariance Kernel

At this point, we find that in order to complete the inference of the mean profiles and their uncertainties, we need some method to specify the covariance kernel $k(x, x')$ and the measurement noise covariance Σ_{ij}. While the latter can be determined through modeling of the diagnostic, the former cannot be determined without some *a priori* information about what the shape of the fit profiles should look like.

Progress can be made by considering the definition of 'mean' when discussing mean profiles. Typically in transport models, this mean refers to a Reynolds averaging operation, which as discussed in the introduction can be implemented using many different types of averages including spatial, temporal, and ensemble averages. In practice, because of systematic uncertainties differing between measurement channels and limited spatial resolution, some amount of spatial averaging is required in order to infer the shape of the mean profiles between the measurements. One method for achieving this spatial average is via convolution with a Gaussian filter of a given length scale ℓ.

This averaging operation can be connected to Gaussian processes in the following way: suppose $w(x)$ is a white noise field, i.e. a Gaussian process with zero mean and delta-correlated covariance kernel $\mathrm{Cov}[w(x), w(x')] = 2W\delta(|x-x'|/\ell_0)$. Consider convolution of $w(x)$ with a Gaussian smoothing filter

$$g(x) = \frac{1}{\sqrt{2\pi}\ell}\exp\left(-\frac{x^2}{2\ell^2}\right) \tag{B.3}$$

Note the Gaussian form of the smoothing filter is not related to the Gaussian nature of the process. Other smoothing filters such as a double-sided exponential $g(x) = \frac{1}{2\ell}\exp\left(-\frac{|x|}{\ell}\right)$ could have been used, although the Gaussian filter is convenient because it has continuous derivatives of all orders[1]. Since convolution is a linear operation, this results in a new Gaussian process $b(x) = g(x) \star w(x)$ which also has mean zero (since $g(x) \star 0 = 0$), and covariance

$$\mathrm{Cov}[b(x+s), b(x)] = g(s) \star (2W\delta(s/\ell_0)) \star g(-s) = \frac{W}{\sqrt{\pi}}\frac{\ell_0}{\ell}\exp\left(-\frac{s^2}{4\ell^2}\right) \tag{B.4}$$

Thus, we see that a Gaussian process with zero mean and squared exponential covariance kernel (referring to the $\exp(-s^2)$) can be seen as a white noise field smoothed by a Gaussian filter. This now provides a precise physical interpretation of GPR, as equations (B.1) and (B.2) provide a rigorous answer to the question "if I were to randomly sample white noise fields then smooth them with a Gaussian filter, if I sample from those smoothed fields by the probability that they are consistent with the experimental measurements, then what is the mean and covariance of these subsampled fields?"

In principle all smooth functions are sampled over as the covariance kernel is positive-definite, in analogy to how the probability density function of a multivariate Gaussian is non-zero everywhere for a positive-definite covariance matrix. Thus, the choice of covariance kernel does not constrain the functional form of the mean profile

---

[1] Note that diffusion tends to improve the regularity of functions

in GPR. This is in contrast to spline fits, which constrain the functional form of the fit by the spline basis functions. Additionally, the quantitative impacts of the fitting parameters in GPR are more transparent than the impacts of knots and regularization terms used in spline fitting. The scale length of the covariance kernel ℓ implies that the typical sample profile primarily has features up to length scale ℓ, while profiles with significant features finer than the length scale ℓ are less likely to be sampled over.

In this thesis, a slightly more complicated covariance kernel was used, namely a squared exponential kernel with spatially varying tanh covariance length scale function. See equations (B.73) and (B.78) in [22]. However, instead of separating the plasma into an ‘edge’ and ‘core’ region, which was appropriate for fits of profiles with transport barriers at the edge, in this thesis the plasma was instead separated into ‘inside sawtooth mixing radius’ and ’outside sawtooth mixing radius’ regions. This was found to be more appropriate for Ohmic L-mode plasmas, where the sawteeth strongly flattened the temperature, density, and velocity profiles within the sawtooth mixing radius.

Additionally, while the discussion in this appendix focused on the case of GPR with a specified covariance kernel, in this thesis the scale lengths and other parameters determining the covariance kernel were not determined ahead of time. Instead, the prior distribution covering a possible range for these parameters was specified, and a Bayesian method described in [21] was used to infer the parameters from the data. Markov Chain Monte Carlo (MCMC) sampling was then used to quantify the additional uncertainty in the fit profiles due to the uncertainty in the parameters describing the covariance kernel. While usage of this MCMC step was not found to affect the uncertainty in the mean profiles much, it was found to have a significant effect on the uncertainty of the mean gradients.

Appendix C

Data and Figure Sources

Most of the figures and analysis in this thesis was performed in Python 2.7. GitHub repositories are available for BSFC `https://github.com/Maplenormandy/bsfc` and other codes `https://github.com/Maplenormandy/psfc-misc`, and are accessible from `/home/normandy/git` on the PSFC workstations. Specific codes and data sources used to generate figures are as follows:

Chapter 4

- Figure 4-1: C-Mod shot #1101014019, $t = 1.25$s.
  `python /home/normandy/git/bsfc/bsfc/bsfc_run_ns.py 1101014019`
- Figure 4-2: C-Mod shot #1160506007, $t = 0.96$s.
  `/home/normandy/git/bsfc/bsfc/bsfc_read_nhermite_scan.py`
- Figures 4-3, 4-4: C-Mod shot #1160506007, $t = 0.96$s
  `/home/normandy/git/bsfc/analysis/bsfc_synthetic_profile_plot.py`
- Figure 4-5: C-Mod shot #1101014019, $t = 1.25$s
  `/home/normandy/git/bsfc/analysis/bsfc_synthetic_profile_plot.py`
- Figure 4-6: C-Mod shot #1160506007, $t = 0.96$s
  `/home/normandy/git/bsfc/analysis/bsfc_profile_plot.py`

- Figure 4-7: C-Mod shot #1101014019, $t = 1.25$s
  `/home/normandy/git/bsfc/analysis/bsfc_profile_plot.py`

Chapters 5, 6, 7

All plots generated by `/home/normandy/git/psfc-misc/PresentationScripts/hysteresis_pop/hysteresis_pop_draft.py`, unless otherwise specified.

- Case I refers to C-Mod shots #1160506007, 008, and 024, or #1120216030 $t = 0.95$s when using the 'matched' case. #1160506007 $t = 0.6$s is SOC and 0.96s is LOC.

- Case II refers to C-Mod shots #110607009, 010, or #1120216017 $t = 1.25$s when using the 'matched' case. #1160506009 $t = 0.72$s is SOC and 0.92s is LOC.

- Case III refers to C-Mod shot #1160506015. $t = 0.68$s is SOC, and 0.9s is LOC.

- Figure 5-1: Rotation profiles from C-Mod shot #1120216017 $t = 1.21$s and 1.43s.

- Figures 5-5, 5-6: Generated with `/home/normandy/git/psfc-misc/PresentationScripts/thesis/thesis_fluctuations.py`

- All configurations for CGYRO can be on the engaging cluster in `/home/normandy/hys2/` or `/home/normandy/1120216/`.

- Figures 6-1, 6-2: Generated with `/home/normandy/git/psfc-misc/PresentationScripts/hysteresis_prl/hysteresis_prl_draft.py`

- Figure 6-5: Generated with `/home/normandy/git/psfc-misc/PresentationScripts/hysteresis_pop/hysteresis_pop_cartoon_draft.py`

Bibliography

[1] C. Angioni, Y. Camenen, F.J. Casson, E. Fable, R.M. McDermott, A.G. Peeters, and J.E. Rice. Off-diagonal particle and toroidal momentum transport: a survey of experimental, theoretical and modelling aspects. *Nuclear Fusion*, 52(11):114003, nov 2012.

[2] H. Arnichand, R. Sabot, S. Hacquin, A. Krämer-Flecken, X. Garbet, J. Citrin, C. Bourdelle, G. Hornung, J. Bernardo, C. Bottereau, F. Clairet, G. Falchetto, and J.C. Giacalone. Quasi-coherent modes and electron-driven turbulence. *Nuclear Fusion*, 54(12):123017, dec 2014.

[3] Arash Ashourvan and P H Diamond. How mesoscopic staircases condense to macroscopic barriers in confined plasma turbulence. *Physical Review E*, 94(5):051202, nov 2016.

[4] E A Belli and J Candy. Kinetic calculation of neoclassical transport including self-consistent electron and impurity dynamics. *Plasma Physics and Controlled Fusion*, 50(9):095010, sep 2008.

[5] Carl M. Bender. Making sense of non-Hermitian Hamiltonians. *Reports on Progress in Physics*, 70(6):947–1018, jun 2007.

[6] H. Biglari, P. H. Diamond, and P. W. Terry. Influence of sheared poloidal rotation on edge turbulence. *Physics of Fluids B: Plasma Physics*, 2(1):1–4, jan 1990.

[7] Christopher M Bishop. *Pattern recognition and machine learning.* springer, 2006.

[8] S Blinnikov and R Moessner. Expansions for nearly Gaussian distributions. *Astronomy and Astrophysics Supplement Series*, 130(1):193–205, may 1998.

[9] A. Bortolon, B. P. Duval, A. Pochelon, and A. Scarabosio. Observation of Spontaneous Toroidal Rotation Inversion in Ohmically Heated Tokamak Plasmas. *Physical Review Letters*, 97(23):235003, dec 2006.

[10] C. Bourdelle, X. Garbet, F. Imbeaux, A. Casati, N. Dubuit, R. Guirlet, and T. Parisot. A new gyrokinetic quasilinear transport model applied to particle transport in tokamak plasmas. *Physics of Plasmas*, 14(11):112501, nov 2007.

[11] Joshua Breslau, Marina Gorelenkova, Francesca Poli, Jai Sachdev, and Xingqiu Yuan. TRANSP. [Computer Software] `https://doi.org/10.11578/dc.20180627.4`, jun 2018.

[12] A. J. Brizard and T. S. Hahm. Foundations of nonlinear gyrokinetic theory. *Reviews of Modern Physics*, 79(2):421–468, 2007.

[13] Y. Camenen, C. Angioni, A. Bortolon, B. P. Duval, E. Fable, W. A. Hornsby, R. M. McDermott, D H Na, Y-S Na, A. G. Peeters, and J. E. Rice. Experimental observations and modelling of intrinsic rotation reversals in tokamaks. *Plasma Physics and Controlled Fusion*, 59(3):034001, mar 2017.

[14] Y. Camenen, Y. Idomura, S. Jolliet, and A.G. Peeters. Consequences of profile shearing on toroidal momentum transport. *Nuclear Fusion*, 51(7):073039, jul 2011.

[15] Y Camenen, A Pochelon, R Behn, A Bottino, A Bortolon, S Coda, A Karpushov, O Sauter, G Zhuang, and the TCV Team. Impact of plasma triangularity and collisionality on electron heat transport in TCV L-mode plasmas. *Nuclear Fusion*, 47(7):510–516, jul 2007.

[16] J. Candy, E.A. Belli, and R.V. Bravenec. A high-accuracy Eulerian gyrokinetic solver for collisional plasmas. *Journal of Computational Physics*, 324:73–93, nov 2016.

[17] N.M. Cao, J.E. Rice, P.H. Diamond, A.E. White, S.G. Baek, M.A. Chilenski, J.W. Hughes, J. Irby, M.L. Reinke, and P. Rodriguez-Fernandez. Hysteresis as a probe of turbulent bifurcation in intrinsic rotation reversals on Alcator C-Mod. *Nuclear Fusion*, 59(10):104001, oct 2019.

[18] N.M. Cao, J.E. Rice, P.H. Diamond, A.E. White, M.A. Chilenski, P.C. Ennever, J.W. Hughes, J. Irby, M.L. Reinke, and P. Rodriguez-Fernandez. Evidence and Modeling of Turbulence Bifurcation in L-mode Confinement Transitions on Alcator C-Mod. *Physics of Plasmas*, page (Accepted), 2020.

[19] Norman M. Cao and Francesco Sciortino. Bayesian Spectral Moment Estimation and Uncertainty Quantification. *IEEE Transactions on Plasma Science*, 48(1):22–30, jan 2020.

[20] J. G. Charney and P. G. Drazin. Propagation of planetary-scale disturbances from the lower into the upper atmosphere. *Journal of Geophysical Research*, 66(1):83–109, jan 1961.

[21] M.A. Chilenski, M. Greenwald, Y. Marzouk, N.T. Howard, A.E. White, J.E. Rice, and J.R. Walk. Improved profile fitting and quantification of uncertainty in experimental measurements of impurity transport coefficients using Gaussian process regression. *Nuclear Fusion*, 55(2):023012, feb 2015.

[22] Mark Alan Chilenski. *Experimental data analysis techniques for validation of Tokamak impurity transport simulations*. PhD thesis, Massachusetts Institute of Technology, 2017.

[23] G J Choi and T S Hahm. ExB shear and precession shear induced turbulence suppression and its influence on electron thermal internal transport barrier formation. *Physics of Plasmas*, 23(7):072301, jul 2016.

[24] J Citrin, H Arnichand, J Bernardo, C Bourdelle, X Garbet, F Jenko, S Hacquin, M J Pueschel, and R Sabot. Comparison between measured and predicted turbulence frequency spectra in ITG and TEM regimes. *Plasma Physics and Controlled Fusion*, 59(6):064010, jun 2017.

[25] Colm Connaughton, Sergey Nazarenko, and Brenda Quinn. Rossby and drift wave turbulence and zonal flows: The Charney–Hasegawa–Mima model and its extensions. *Physics Reports*, 604:1–71, dec 2015.

[26] B. Coppi and F. Pegoraro. Theory of the ubiquitous mode. *Nuclear Fusion*, 17(5):969–993, oct 1977.

[27] Luc Devroye. *Non-Uniform Random Variate Generation*. Springer-Verlag, New York, 1986.

[28] P. H. Diamond, S. I. Itoh, K. Itoh, and T. S. Hahm. Zonal flows in plasma - A review. *Plasma Physics and Controlled Fusion*, 47(5):R35–R161, 2005.

[29] P. H. Diamond, Y.-M. Liang, B. A. Carreras, and P. W. Terry. Self-Regulating Shear Flow Turbulence: A Paradigm for the L to H Transition. *Physical Review Letters*, 72(16):2565–2568, apr 1994.

[30] P. H. Diamond, C. J. McDevitt, Ö D. Gürcan, T. S. Hahm, and V. Naulin. Transport of parallel momentum by collisionless drift wave turbulence. *Physics of Plasmas*, 15(1):012303, jan 2008.

[31] Patrick H. Diamond, Sanae-I. Itoh, and Kimitaka Itoh. *Modern Plasma Physics*. Cambridge University Press, Cambridge, 2010.

[32] P.H. Diamond, Y. Kosuga, Ö.D. Gürcan, C.J. McDevitt, T.S. Hahm, N. Fedorczak, J.E. Rice, W.X. Wang, S. Ku, J.M. Kwon, G. Dif-Pradalier, J. Abiteboul, L. Wang, W.H. Ko, Y.J. Shi, K. Ida, W. Solomon, H. Jhang, S.S. Kim, S. Yi, S.H. Ko, Y. Sarazin, R. Singh, and C.S. Chang. An overview of intrinsic torque and momentum transport bifurcations in toroidal plasmas. *Nuclear Fusion*, 53(10):104019, oct 2013.

[33] G Dif-Pradalier, P H Diamond, V Grandgirard, Y Sarazin, J Abiteboul, X Garbet, Ph Ghendrih, A Strugarek, S Ku, and C S Chang. On the validity of the local diffusive paradigm in turbulent plasma transport. *Physical Review E*, 82(2):025401, aug 2010.

[34] E.J. Doyle (Chair Transport Physics), W.A. Houlberg (Chair Confinement Database and Modelling), Y. Kamada (Chair Pedestal and Edge), V. Mukhovatov (co-Chair Transport Physics), , T.H. Osborne (co-Chair Pedestal Edge), A. Polevoi (co-Chair Confinement Da Modelling), G Bateman, J.W Connor, J.G. Cordey (retired), T Fujita, X Garbet, T.S Hahm, L.D Horton, A.E Hubbard, F Imbeaux, F Jenko, J.E Kinsey, Y Kishimoto, J Li, T.C Luce, Y Martin, M Ossipenko, V Parail, A Peeters, T.L Rhodes, J.E Rice, C.M Roach, V Rozhansky, F Ryter, G Saibene, R Sartori, A.C.C Sips, J.A Snipes, M Sugihara, E.J Synakowski, H Takenaga, T Takizuka, K Thomsen, M.R Wade, H.R Wilson, ITPA Transport Physics Topical Group, ITPA Confinement Database Group, Model, ITPA Pedestal Group, and Edge Topical. Chapter 2: Plasma confinement and transport. *Nuclear Fusion*, 47(6):S18–S127, jun 2007.

[35] D G Dritschel and M. E. McIntyre. Multiple Jets as PV Staircases: The Phillips Effect and the Resilience of Eddy-Transport Barriers. *Journal of the Atmospheric Sciences*, 65(3):855–874, mar 2008.

[36] T H Dupree. A Perturbation Theory for Strong Plasma Turbulence. *Physics of Fluids*, 9(9):1773, 1966.

[37] E.F Eikenberry, Ch Brönnimann, G Hülsen, H Toyokawa, R Horisberger, B Schmitt, C Schulze-Briese, and T Tomizaki. PILATUS: a two-dimensional X-ray detector for macromolecular crystallography. *Nuclear Instruments and Methods in Physics Research Section A: Accelerators, Spectrometers, Detectors and Associated Equipment*, 501(1):260–266, mar 2003.

[38] Michael Eldred and John Burkardt. Comparison of Non-Intrusive Polynomial Chaos and Stochastic Collocation Methods for Uncertainty Quantification. In *47th AIAA Aerospace Sciences Meeting including The New Horizons Forum and Aerospace Exposition*, Reston, Virigina, jan 2009. American Institute of Aeronautics and Astronautics.

[39] P.C. Ennever. *Turbulence and Transport Measurements in Alcator C-Mod and Comparisons with Gyrokinetic Simulations.* PhD thesis, Massachusetts Institute of Technology, 2016.

[40] D R Ernst, J Lang, W M Nevins, M Hoffman, Y Chen, W Dorland, and S Parker. Role of zonal flows in trapped electron mode turbulence through nonlinear gyrokinetic particle and continuum simulation. *Physics of Plasmas*, 16(5):055906, may 2009.

[41] I Erofeev, E Fable, C Angioni, and R.M. McDermott. Theory-based modeling of LOC–SOC transitions in ASDEX Upgrade. *Nuclear Fusion*, 57(12):126067, dec 2017.

[42] Gregory L Eyink. Dissipative anomalies in singular Euler flows. *Physica D: Nonlinear Phenomena*, 237(14-17):1956–1968, aug 2008.

[43] S. J. Freethy, T. Görler, A. J. Creely, G. D. Conway, S. S. Denk, T. Happel, C. Koenen, P. Hennequin, and A. E. White. Validation of gyrokinetic simulations with measurements of electron temperature fluctuations and density-temperature phase angles on ASDEX Upgrade. *Physics of Plasmas*, 25(5):055903, may 2018.

[44] Uriel Frisch. *Turbulence.* Cambridge University Press, nov 1995.

[45] X Garbet. Turbulence in fusion plasmas: key issues and impact on transport modelling. *Plasma Physics and Controlled Fusion*, 43(12A):A251–A266, dec 2001.

[46] O Gehre, O Gruber, H D Murmann, D E Roberts, F Wagner, B Bomba, A Eberhagen, H U Fahrbach, G Fussmann, J Gernhardt, K. Hübner, G Janeschitz, K Lackner, E. R. Müller, H Niedermeyer, H. Röhr, G Staudenmaier, K H Steuer, and O Vollmer. Improved confinement with counter neutral injection into ASDEX. *Physical Review Letters*, 60(15):1502–1505, apr 1988.

[47] Nigel Goldenfeld. *Lectures on phase transitions and the renormalization group.* CRC Press, 2018.

[48] M. Greenwald, A. Bader, S. Baek, M. Bakhtiari, H. Barnard, W. Beck, W. Bergerson, I. Bespamyatnov, P. Bonoli, D. Brower, D. Brunner, W. Burke, J. Candy, M. Churchill, I. Cziegler, A. Diallo, A. Dominguez, B. Duval, E. Edlund, P. Ennever, D. Ernst, I. Faust, C. Fiore, T. Fredian, O. Garcia, C. Gao, J. Goetz, T. Golfinopoulos, R. Granetz, O. Grulke, Z. Hartwig, S. Horne, N. Howard, A. Hubbard, J. Hughes, I. Hutchinson, J. Irby, V. Izzo, C. Kessel, B. LaBombard, C. Lau, C. Li, Y. Lin, B. Lipschultz, A. Loarte, E. Marmar, A. Mazurenko, G. McCracken, R. McDermott, O. Meneghini, D. Mikkelsen, D. Mossessian, R. Mumgaard, J. Myra, E. Nelson-Melby, R. Ochoukov, G. Olynyk, R. Parker, S. Pitcher, Y. Podpaly, M. Porkolab, M. Reinke, J. Rice, W. Rowan, A. Schmidt, S. Scott, S. Shiraiwa, J. Sierchio, N. Smick, J. A. Snipes, P. Snyder, B. Sorbom, J. Stillerman, C. Sung, Y. Takase, V. Tang, J. Terry, D. Terry, C. Theiler, A. Tronchin-James, N. Tsujii, R. Vieira, J. Walk, G. Wallace, A. White, D. Whyte, J. Wilson, S. Wolfe, G. Wright, J. Wright, S. Wukitch, and S. Zweben. 20 years of research on the Alcator C-Mod tokamak. *Physics of Plasmas*, 21(11):110501, nov 2014.

[49] Martin Greenwald. Verification and validation for magnetic fusion. *Physics of Plasmas*, 17(5):058101, may 2010.

[50] B A Grierson, C Chrystal, S R Haskey, W X Wang, T L Rhodes, G. R. McKee, K Barada, X Yuan, M F F Nave, A Ashourvan, and C Holland. Main-ion intrinsic toroidal rotation across the ITG/TEM boundary in DIII-D discharges during ohmic and electron cyclotron heating. *Physics of Plasmas*, 26(4):042304, apr 2019.

[51] B. A. Grierson, W. X. Wang, S. Ethier, G. M. Staebler, D. J. Battaglia, J. A. Boedo, J. S. DeGrassie, and W. M. Solomon. Main-Ion Intrinsic Toroidal Rotation Profile Driven by Residual Stress Torque from Ion Temperature Gradient Turbulence in the DIII-D Tokamak. *Physical Review Letters*, 118(1):015002, jan 2017.

[52] Ö D Gürcan and P H Diamond. Zonal flows and pattern formation. *Journal of Physics A: Mathematical and Theoretical*, 48(29):293001, jul 2015.

[53] T S Hahm and K H Burrell. Flow shear induced fluctuation suppression in finite aspect ratio shaped tokamak plasma. *Physics of Plasmas*, 2(5):1648–1651, may 1995.

[54] D R Hatch, P W Terry, F Jenko, F Merz, M J Pueschel, W M Nevins, and E Wang. Role of subdominant stable modes in plasma microturbulence. *Physics of Plasmas*, 18(5):055706, may 2011.

[55] Per Helander and Dieter J. Sigmar. *Collisional Transport in Magnetized Plasmas.* Cambridge University Press, 2002.

[56] A. Hirose. Electron temperature gradient modes in tokamaks. *Physics of Fluids B: Plasma Physics*, 2(4):850–853, apr 1990.

[57] W. A. Hornsby, C. Angioni, Z. X. Lu, E. Fable, I. Erofeev, R. McDermott, A. Medvedeva, A. Lebschy, and A. G. Peeters. Global gyrokinetic simulations of intrinsic rotation in ASDEX Upgrade Ohmic L-mode plasmas. *Nuclear Fusion*, 58(5), 2018.

[58] G. Hornung, G. Dif-Pradalier, F. Clairet, Y. Sarazin, R. Sabot, P. Hennequin, and G. Verdoolaege. $\mathbf{E} \times \mathbf{B}$ staircases and barrier permeability in magnetised plasmas. *Nuclear Fusion*, 57(1):014006, jan 2017.

[59] I. H. Hutchinson. *Principles of Plasma Diagnostics.* Cambridge University Press, Cambridge, 2002.

[60] A Ince-Cushman. *Rotation studies in fusion plasmas via imaging X-ray crystal spectroscopy.* PhD thesis, Massachusetts Institute of Technology, 2008.

[61] A Ince-Cushman, J E Rice, M Bitter, M L Reinke, K W Hill, M F Gu, E Eikenberry, Ch Broennimann, S Scott, Y Podpaly, S G Lee, and E S Marmar. Spatially resolved high resolution x-ray spectroscopy for magnetically confined fusion plasmas (invited). *Review of Scientific Instruments*, 79(10):10E302, oct 2008.

[62] Philip Isett. A proof of Onsager's conjecture. *Annals of Mathematics*, 188(3):871, 2018.

[63] ITER Physics Basis Editors ITER Physics Expert Group on Confin and Transport, ITER Physics Expert Group on Confin and Database. Chapter 2: Plasma confinement and transport. *Nuclear Fusion*, 39(12):2175–2249, dec 1999.

[64] K. Itoh, Y Nagashima, S.-I Itoh, P H Diamond, A Fujisawa, M Yagi, and A Fukuyama. On the bicoherence analysis of plasma turbulence. *Physics of Plasmas*, 12(10):102301, oct 2005.

[65] Edwin Jaynes. Prior Probabilities. *IEEE Transactions on Systems Science and Cybernetics*, 4(3):227–241, 1968.

[66] H H Johann. Die Erzeugung lichtstarker Röntgenspektren mit Hilfe von Konkavkristallen. *Zeitschrift für Physik*, 69(3-4):185–206, may 1931.

[67] B.B. Kadomtsev and O.P. Pogutse. Trapped particles in toroidal magnetic systems. *Nuclear Fusion*, 11(1):67–92, jan 1971.

[68] N G Van Kampen. On the theory of stationary waves in plasmas. *Physica*, 21(6-10):949–963, 1955.

[69] M F Kasim, T P Galligan, J Topp-Mugglestone, G Gregori, and S M Vinko. Inverse Problem Instabilities in Large-Scale Plasma Modelling. may 2018.

[70] M. Kikuchi, T. Takizuka, S. Medvedev, T. Ando, D. Chen, J.X. Li, M. Austin, O. Sauter, L. Villard, A. Merle, M. Fontana, Y. Kishimoto, and K. Imadera. L-mode-edge negative triangularity tokamak reactor. *Nuclear Fusion*, 59(5):056017, may 2019.

[71] A. N. Kolmogorov. The local structure of turbulence in incompressible viscous fluid for very large Reynolds numbers. *Proceedings of the Royal Society of London. Series A: Mathematical and Physical Sciences*, 434(1890):9–13, jul 1991.

[72] Y. Kosuga, P. H. Diamond, and Ö D. Gürcan. On the efficiency of intrinsic rotation generation in tokamaks. *Physics of Plasmas*, 17(10):102313, oct 2010.

[73] Y Kosuga, S.-I. Itoh, P H Diamond, K Itoh, and M Lesur. Ion temperature gradient driven turbulence with strong trapped ion resonance. *Physics of Plasmas*, 21(10):102303, oct 2014.

[74] John A Krommes. Fundamental statistical descriptions of plasma turbulence in magnetic fields. *Physics Reports*, 360(1-4):1–352, apr 2002.

[75] Ryogo Kubo. Stochastic Liouville Equations. *Journal of Mathematical Physics*, 4(2):174–183, feb 1963.

[76] Hsiao-lan Kuo. DYNAMIC INSTABILITY OF TWO-DIMENSIONAL NONDIVERGENT FLOW IN A BAROTROPIC ATMOSPHERE. *Journal of Meteorology*, 6(2):105–122, apr 1949.

[77] Daniel (Daniel Joowon) Kwak. Investigation of intrinsic rotation dependencies in Alcator C-Mod using a new data analysis workflow. Master's thesis, Massachusetts Institute of Technology, 2015.

[78] J.M. Kwon, S. Yi, T. Rhee, P.H. Diamond, K. Miki, T.S. Hahm, J.Y. Kim, Ö.D. Gürcan, and C. McDevitt. Analysis of symmetry breaking mechanisms and the role of turbulence self-regulation in intrinsic rotation. *Nuclear Fusion*, 52(1):013004, jan 2012.

[79] Jianying Lang, Yang Chen, and Scott E Parker. Gyrokinetic δf particle simulation of trapped electron mode driven turbulence. *Physics of Plasmas*, 14(8):082315, aug 2007.

[80] Jianying Lang, Scott E Parker, and Yang Chen. Nonlinear saturation of collisionless trapped electron mode turbulence: Zonal flows and zonal density. *Physics of Plasmas*, 15(5):055907, may 2008.

[81] A Langenberg, J Svensson, H Thomsen, O Marchuk, N A Pablant, R Burhenn, and R C Wolf. Forward Modeling of X-Ray Imaging Crystal Spectrometers Within the Minerva Bayesian Analysis Framework. *Fusion Science and Technology*, 69(2):560–567, apr 2016.

[82] Y Lin, R Nazikian, J H Irby, and E S Marmar. Plasma curvature effects on microwave reflectometry fluctuation measurements. *Plasma Physics and Controlled Fusion*, 43(1):L1–L8, jan 2001.

[83] G. Matheron. The intrinsic random functions and their applications. *Advances in Applied Probability*, 5(3):439–468, dec 1973.

[84] R.M. McDermott, C. Angioni, G.D. Conway, R. Dux, E. Fable, R. Fischer, T. Pütterich, F. Ryter, and E. Viezzer. Core intrinsic rotation behaviour in ASDEX Upgrade ohmic L-mode plasmas. *Nuclear Fusion*, 54(4):043009, apr 2014.

[85] S.Yu. Medvedev, M Kikuchi, L Villard, T Takizuka, P Diamond, H Zushi, K Nagasaki, X Duan, Y Wu, A.A. Ivanov, A.A. Martynov, Yu.Yu. Poshekhonov, A Fasoli, and O Sauter. The negative triangularity tokamak: stability limits and prospects as a fusion energy system. *Nuclear Fusion*, 55(6):063013, jun 2015.

[86] F Merz and F Jenko. Nonlinear Saturation of Trapped Electron Modes via Perpendicular Particle Diffusion. *Physical Review Letters*, 100(3):035005, jan 2008.

[87] Clément Mouhot and Cédric Villani. On Landau damping. *Acta Mathematica*, 207(1):29–201, 2011.

[88] D. H. Na, Yong Su Na, S. G. Lee, C. Angioni, S. M. Yang, H. S. Kim, T. S. Hahm, W. H. Ko, H. Jhang, and W. J. Lee. Observation of the intrinsic rotation in KSTAR Ohmic L-mode plasmas. *Nuclear Fusion*, 56(3), 2016.

[89] Sergey Nazarenko. *Wave Turbulence*, volume 825 of *Lecture Notes in Physics*. Springer Berlin Heidelberg, Berlin, Heidelberg, 2011.

[90] H. Nordman and J. Weiland. Transport due to toroidal η i mode turbulence in tokamaks. *Nuclear Fusion*, 29(2):251–263, feb 1989.

[91] N. A. Pablant, R. E. Bell, M. Bitter, L. Delgado-Aparicio, K. W. Hill, S. Lazerson, and S. Morita. Tomographic inversion techniques incorporating physical constraints for line integrated spectroscopy in stellarators and tokamaks. *Review of Scientific Instruments*, 85(11):11E424, nov 2014.

[92] Felix I Parra and Peter J Catto. Vorticity and intrinsic ambipolarity in turbulent tokamaks. *Plasma Physics and Controlled Fusion*, 51(9):095008, sep 2009.

[93] A. G. Peeters and C. Angioni. Linear gyrokinetic calculations of toroidal momentum transport in a tokamak due to the ion temperature gradient mode. *Physics of Plasmas*, 12(7):072515, jul 2005.

[94] A.G. Peeters, C. Angioni, A. Bortolon, Y. Camenen, F.J. Casson, B. Duval, L. Fiederspiel, W.A. Hornsby, Y. Idomura, T. Hein, N. Kluy, P. Mantica, F.I. Parra, A.P. Snodin, G. Szepesi, D. Strintzi, T. Tala, G. Tardini, P. de Vries, and J. Weiland. Overview of toroidal momentum transport. *Nuclear Fusion*, 51(9):094027, sep 2011.

[95] Miklos Porkolab, J.C. Rost, Nils Basse, James Dorris, Eric Edlund, Liang Lin, Yijun Lin, and Steve Wukitch. Phase contrast imaging of waves and instabilities in high temperature magnetized fusion plasmas. *IEEE Transactions on Plasma Science*, 34(2):229–234, apr 2006.

[96] Hong Qin, Ruili Zhang, Alexander S Glasser, and Jianyuan Xiao. Kelvin-Helmholtz instability is the result of parity-time symmetry breaking. *Physics of Plasmas*, 26(3):032102, mar 2019.

[97] M L Reinke, Y A Podpaly, M Bitter, I H Hutchinson, J E Rice, L Delgado-Aparicio, C Gao, M Greenwald, K Hill, N T Howard, A Hubbard, J W Hughes, N Pablant, A E White, and S M Wolfe. X-ray imaging crystal spectroscopy for use in plasma transport research. *The Review of scientific instruments*, 83(11):113504, nov 2012.

[98] M. L. Reinke, J. E. Rice, A. E. White, M. Greenwald, N. T. Howard, P. Ennever, C. Gao, A. E. Hubbard, and J. W. Hughes. Density sensitivity of intrinsic rotation profiles in ion cyclotron range of frequency-heated L-mode plasmas. *Plasma Physics and Controlled Fusion*, 55(1):012001, jan 2013.

[99] J E Rice, I Cziegler, P H Diamond, B P Duval, Y A Podpaly, M L Reinke, P C Ennever, M J Greenwald, J W Hughes, Y Ma, E S Marmar, M Porkolab, N Tsujii, and S M Wolfe. Rotation Reversal Bifurcation and Energy Confinement Saturation in Tokamak Ohmic L-Mode Plasmas. *Physical Review Letters*, 107(26):265001, dec 2011.

[100] J E Rice, M J Greenwald, Y A Podpaly, M L Reinke, P H Diamond, J W Hughes, N T Howard, Y Ma, I Cziegler, B P Duval, P C Ennever, D Ernst, C L Fiore, C Gao, J H Irby, E S Marmar, M Porkolab, N Tsujii, and S M Wolfe. Ohmic energy confinement saturation and core toroidal rotation reversal in Alcator C-Mod plasmas. *Physics of Plasmas*, 19(5):056106, may 2012.

[101] J E Rice, M L Reinke, J M A Ashbourn, C Gao, M Bitter, L Delgado-Aparicio, K Hill, N T Howard, J W Hughes, and U I Safronova. X-ray observations of medium Z H- and He-like ions with satellites from C-Mod tokamak plasmas. *Journal of Physics B: Atomic, Molecular and Optical Physics*, 48(14):144013, jul 2015.

[102] J.E. Rice, B.P. Duval, M.L. Reinke, Y.A. Podpaly, A. Bortolon, R.M. Churchill, I. Cziegler, P.H. Diamond, A. Dominguez, P.C. Ennever, C.L. Fiore, R.S. Granetz, M.J. Greenwald, A.E. Hubbard, J.W. Hughes, J.H. Irby, Y. Ma, E.S. Marmar, R.M. McDermott, M. Porkolab, N. Tsujii, and S.M. Wolfe. Observations of core toroidal rotation reversals in Alcator C-Mod ohmic L-mode plasmas. *Nuclear Fusion*, 51(8):083005, aug 2011.

[103] J.E. Rice, C. Gao, M.L. Reinke, P.H. Diamond, N.T. Howard, H.J. Sun, I. Cziegler, A.E. Hubbard, Y.A. Podpaly, W.L. Rowan, J.L. Terry, M.A. Chilenski, L. Delgado-Aparicio, P.C. Ennever, D. Ernst, M.J. Greenwald, J.W. Hughes, Y. Ma, E.S. Marmar, M. Porkolab, A.E. White, and S.M. Wolfe. Non-local heat transport, rotation reversals and up/down impurity density asymmetries in Alcator C-Mod ohmic L-mode plasmas. *Nuclear Fusion*, 53(3):033004, mar 2013.

[104] J.E. Rice, M.L. Reinke, N. Cao, J.W. Hughes, J.M.A. Ashbourn, D.R. Ernst, A.E. Hubbard, and J.H. Irby. Up/down impurity density asymmetries in C-Mod plasmas. *Nuclear Fusion*, 58(12):126008, dec 2018.

[105] P. Rodriguez-Fernandez, A. E. White, N. T. Howard, B. A. Grierson, G. M. Staebler, J. E. Rice, X. Yuan, N. M. Cao, A. J. Creely, M. J. Greenwald, A. E. Hubbard, J. W. Hughes, J. H. Irby, and F. Sciortino. Explaining Cold-Pulse Dynamics in Tokamak Plasmas Using Local Turbulent Transport Models. *Physical Review Letters*, 120(7):075001, feb 2018.

[106] P. Rodriguez-Fernandez, A.E. White, N.T. Howard, B.A. Grierson, X. Yuan, G.M. Staebler, J.E. Rice, C. Angioni, N.M. Cao, A.J. Creely, E. Fable, M.J. Greenwald, A.E. Hubbard, J.W. Hughes, J.H. Irby, and F. Sciortino. Perturbative transport modeling of cold-pulse dynamics in Alcator C-Mod Ohmic plasmas. *Nuclear Fusion*, 59(6):066017, jun 2019.

[107] F. Romanelli, W.M. Tang, and R.B. White. Anomalous thermal confinement in ohmically heated tokamaks. *Nuclear Fusion*, 26(11):1515–1528, nov 1986.

[108] Roal'd Zinnurovič Sagdeev and Albert A Galeev. Nonlinear plasma theory. *Nonlinear Plasma Theory, New York: Benjamin, 1969*, 1969.

[109] A A Schekochihin, J T Parker, E G Highcock, P J Dellar, W Dorland, and G W Hammett. Phase mixing versus nonlinear advection in drift-kinetic plasma turbulence. *Journal of Plasma Physics*, 82(2):905820212, apr 2016.

[110] A I Smolyakov, P H Diamond, and V I Shevchenko. Zonal flow generation by parametric instability in magnetized plasmas and geostrophic fluids. *Physics of Plasmas*, 7(5):1349–1351, may 2000.

[111] G. M. Staebler, J. E. Kinsey, and R. E. Waltz. A theory-based transport model with comprehensive physics. *Physics of Plasmas*, 14(5):055909, may 2007.

[112] Paul Cornelis Stek. *Reflectometry Measurements on Alcator C-Mod.* PhD thesis, Massachusetts Institute of Technology, 1997.

[113] K Stewartson. The evolution of the critical layer of a Rossby wave. *Geophysical & Astrophysical Fluid Dynamics*, 9(1):185–200, jan 1977.

[114] C. Sung, A. E. White, D. R. Mikkelsen, M. Greenwald, C. Holland, N. T. Howard, R. Churchill, and C. Theiler. Quantitative comparison of electron temperature fluctuations to nonlinear gyrokinetic simulations in C-Mod Ohmic L-mode discharges. *Physics of Plasmas*, 23(4):042303, apr 2016.

[115] C. Sung, A.E. White, N.T. Howard, C.Y. Oi, J.E. Rice, C. Gao, P. Ennever, M. Porkolab, F. Parra, D. Mikkelsen, D. Ernst, J. Walk, J.W. Hughes, J. Irby, C. Kasten, A.E. Hubbard, and M.J. Greenwald. Changes in core electron temperature fluctuations across the ohmic energy confinement transition in Alcator C-Mod plasmas. *Nuclear Fusion*, 53(8):083010, aug 2013.

[116] Choongki Sung. *Experimental study of turbulent heat transport in Alcator C-Mod.* PhD thesis, Massachusetts Institute of Technology, 2015.

[117] T Tatsuno, W Dorland, A A Schekochihin, G G Plunk, M Barnes, S C Cowley, and G G Howes. Nonlinear Phase Mixing and Phase-Space Cascade of Entropy in Gyrokinetic Plasma Turbulence. *Physical Review Letters*, 103(1):015003, jun 2009.

[118] Cédric Villani. Particle systems and nonlinear Landau damping. *Physics of Plasmas*, 21(3):030901, mar 2014.

[119] F. Wagner and U. Stroth. Transport in toroidal devices-the experimentalist's view. *Plasma Physics and Controlled Fusion*, 35(10):1321–1371, oct 1993.

[120] R. E. Waltz, A. Casati, and G. M. Staebler. Gyrokinetic simulation tests of quasilinear and tracer transport. *Physics of Plasmas*, 16(7):072303, jul 2009.

[121] R. E. Waltz, R. L. Dewar, and X. Garbet. Theory and simulation of rotational shear stabilization of turbulence. *Physics of Plasmas*, 5(5):1784–1792, may 1998.

[122] Lu Wang and P. H. Diamond. Gyrokinetic Theory of Turbulent Acceleration of Parallel Rotation in Tokamak Plasmas. *Physical Review Letters*, 110(26):265006, jun 2013.

[123] Lu Wang, Shuitao Peng, and P H Diamond. Intrinsic rotation drive by collisionless trapped electron mode turbulence. *Physics of Plasmas*, 23(4):042309, apr 2016.

[124] W. X. Wang, P. H. Diamond, T. S. Hahm, S. Ethier, G. Rewoldt, and W. M. Tang. Nonlinear flow generation by electrostatic turbulence in tokamaks. *Physics of Plasmas*, 17(7):072511, jul 2010.

[125] A. E. White, N. T. Howard, M. Greenwald, M. L. Reinke, C. Sung, S. Baek, M. Barnes, J. Candy, A. Dominguez, D. Ernst, C. Gao, A. E. Hubbard, J. W. Hughes, Y. Lin, D. Mikkelsen, F. Parra, M. Porkolab, J. E. Rice, J. Walk, S. J. Wukitch, and Alcator C.Mod Team. Multi-channel transport experiments at Alcator C-Mod and comparison with gyrokinetic simulations. *Physics of Plasmas*, 20(5):0–11, 2013.

[126] A. E. White, W. A. Peebles, T. L. Rhodes, C. H. Holland, G. Wang, L. Schmitz, T. A. Carter, J. C. Hillesheim, E. J. Doyle, L. Zeng, G. R. McKee, G. M. Staebler, R. E. Waltz, J. C. DeBoo, C. C. Petty, and K. H. Burrell. Measurements of the cross-phase angle between density and electron temperature fluctuations and comparison with gyrokinetic simulations. *Physics of Plasmas*, 17(5):056103, may 2010.

[127] DAVID WILCOX. A half century historical review of the k-omega model. In *29th Aerospace Sciences Meeting*, Reston, Virigina, jan 1991. American Institute of Aeronautics and Astronautics.

[128] Yong Xiao and Zhihong Lin. Turbulent Transport of Trapped-Electron Modes in Collisionless Plasmas. *Physical Review Letters*, 103(8):085004, aug 2009.

[129] A. Yoshizawa, S.I. Itoh, and K. Itoh. *Plasma and Fluid Turbulence.* CRC Press, nov 2002.